JOURNAL OF APPLIED PHYSICS

JOURNAL OF APPLIED PHYSICS

Vol. 23, No. 3 MARCH, 1952

In This Issue

	Page
Phenomena Associated with the Flight of Ultra-Speed Pellets. Part III. General Features of Luminosity — John S. Rinehart, William A. Allen, and W. C. White	297
Mechanisms of Positive and Negative Corona in Hydrogen and Argon between Coaxial Cylindrical Electrodes over an Extended Pressure Range — Eugene J. Lauer	300
Statistical Theory of Rubber-Like Elasticity. V. The Stress Birefringence — Akira Isihara, Natsuki Hashitsume, and Masao Tatibana	308
Measurement of the DC Resistance of Selenium and Copper Oxide Rectifiers below Room Temperature — D. M. Grimes and Sam Legvold	312
Domain Structure of Perminvar Having a Rectangular Hysteresis Loop — H. J. Williams and Matilda Goertz	316
Study of Imperfections of Crystal Structure in Polycrystalline Materials: Low Carbon Alloy and Silicon Ferrite — J. J. Slade, Jr., and Sigmund Weissmann	323
Lattice Parameters, Coefficients of Thermal Expansion, and Atomic Weights of Purest Silicon and Germanium — M. E. Straumanis and E. Z. Aka	330
Approximate Elastic Spectrum of β-Brass from X-Ray Scattering — H. Cole and B. E. Warren	335
Analysis of Certain Errors in the X-Ray Reflection Method for the Quantitative Determination of Preferred Orientations — Warren P. Chernock and Paul A. Beck	341
Correlation of DC and Microsecond Pulsed Emission from Oxide Coated Cathodes — Frank A. Horak	346
Allotropic Transformation of Hafnium and a Tentative Equilibrium Diagram of the System Zirconium-Hafnium — J. D. Fast	350
Physical Structure and Magnetic Anisotropy of Alnico 5. Part I — R. D. Heidenreich and E. A. Nesbitt	352
Physical Structure and Magnetic Anisotropy of Alnico 5. Part II — E. A. Nesbitt and R. D. Heidenreich	366
Letters to the Editor:	
Reduction of Three-Dimensional Electromagnetic Problems — John W. Miles	372
Heat Conduction Along an Exponential Bar — John W. Miles	372
Physical Entropy and Information — D. A. Bell	372
Radiofrequency Field Quenching of Ultraviolet Excited Phosphors — T. Miller and K. N. Fromm	373
Diffusion in Grain Boundaries — M. H. Dawson	373
Diffusion in Grain Boundaries — M. R. Achter and R. Smoluchowski	373
Shock Wave Formation in a Shock Tube — George A. Lundquist	374
New Superlattice in Co-Pt Alloys — A. H. Geisler and D. L. Martin	375
Announcements:	
Conferences	375
Recent Appointments	375
Index to Advertisers	xxiv

BOARD OF EDITORS

Elmer Hutchisson, *Editor*

Earle C. Gregg, *Assistant Editor*

Associate Editors

Howard H. Aiken
Ray E. Bolz
Lyle D. Borst
Robert D. Heidenreich
James Hillier
Leonard B. Loeb
W. James Lyons
Eric Reissner
Roman Smoluchowski

Publication of the American Institute of Physics

OFFICERS

George R. Harrison, *Chairman*
George B. Pegram, *Treasurer*

GOVERNING BOARD

Karl K. Darrow
G. J. Dienes
S. A. Goudsmit
G. P. Harnwell
George R. Harrison
F. V. Hunt
Rudolph Kingslake
Hugh S. Knowles
C. C. Lauritsen
F. W. Loomis
William F. Meggers
George B. Pegram
I. I. Rabi
Duane Roller
Frederick Seitz
Francis G. Slack
John C. Steinberg
Richard M. Sutton
Mark W. Zemansky

Consultant on Printing

Melvin Loos

ADMINISTRATIVE STAFF

Henry A. Barton, *Director*
Wallace Waterfall, *Executive Secretary*
Theodore Vorburger, *Advertising Manager*
Ruth F. Bryans, *Publication Manager*
Betty H. Goodfriend, *Assistant Secretary*
Eileen B. Neuberger, *Circulation Manager*
Kathryn Setze *Assistant Treasurer*

The Journal of Applied Physics, published monthly at Prince and Lemon Sts., Lancaster, Pa., is devoted to physics in its role as the science basic to other natural sciences and to the arts and industries. Previous to 1937 this publication was known as Physics. The Journal of Applied Physics publishes editorials and reviews, as well as technical papers of applied physics. Articles appearing in it are indexed regularly, according to their field, by Physics Abstracts, Chemical Abstracts, Engineering Index, Inc., Industrial Arts Index, etc.

Manuscripts should be submitted to Elmer Hutchisson, Editor, Case Institute of Technology, Cleveland 6, Ohio. Unless otherwise stated, submission of a manuscript is a representation that it has been neither copyrighted, published, nor submitted for publication elsewhere. The authors' institutions are requested to pay a **publication charge** of $8 per page which, if honored, entitles them to 100 reprints without further charge. Instructions will be sent with galley proofs.

Subscriptions, renewals, and orders for back numbers should be addressed to the American Institute of Physics, 57 East 55 Street, New York 22, New York.

Subscription Price	U.S. and Canada	Elsewhere
To members of the American Institute of Physics and Affiliated Societies	$10.00	$11.00
To all others	12.00	13.00

Back Number Prices

Yearly back number rate when complete year is available: $10.00. Single copies: $1.00 each.

Changes of address should be sent to the American Institute of Physics; **corrected proofs** should be sent to the Publication Manager, American Institute of Physics. **Advertising rates** supplied on request. Orders, advertising copy, and cuts should be sent to the American Institute of Physics.

Entered as second class matter January 22, 1937, at the Post Office at Lancaster, Pennsylvania, under the Act of March 3, 1879. Accepted for mailing at the special rate of postage provided for in paragraph (d-2), section 34.40, P. L. & R. of 1948, authorized May 2, 1932.

Copyright 1952, by the American Institute of Physics.

Journal
of
Applied Physics

Volume 23, Number 3 March, 1952

Phenomena Associated with the Flight of Ultra-Speed Pellets.* Part III. General Features of Luminosity

JOHN S. RINEHART, WILLIAM A. ALLEN, AND W. C. WHITE
Michelson Laboratory, United States Naval Ordnance Test Station, Inyokern, China Lake, California
(Received July 16, 1951)

Ultra-speed pellets of the lighter metals such as aluminum and magnesium generate intensely luminous trails when fired through air. A pronounced characteristic of the luminous trails is the *intermittent* manner in which the light is emitted. This effect has also been observed in meteors and in studies of conventional shaped charges. Photographs indicate that flashing is caused by yawing of the pellet.

The brilliant flashes of light are associated with the ablation and subsequent burning of material f om the pellet. There is evidence that the material is removed from the pellet in the form of small droplets.

The brightness, luminous output, and temperature of the trail generated by an aluminum pellet have been measured. The brightness is approximately 25,000 lamberts, the luminous output is 30,000 lumen-seconds, and the color temperature is 2900°K.

INTRODUCTION

THE ballistics of ultra-speed pellets have been discussed in Part I of this report, and the spectral characteristics of the luminous trails associated with such pellets have been treated in Part II. The present part, Part III, deals with the general features of luminosity. Flashing, brightness, temperature, and dependence of luminosity on such factors as material and velocity are discussed.

FLASHING

The most striking feature of the light associated with the flight of an ultra-speed pellet is its intermittent character. This intermittency in luminosity we refer to as *flashing*. A similar effect is observed in meteors where the flashes are usually called bursts.[1,2] The very fast fragments projected by shaped charges also flash.[3]

The characteristic features of flashing are well illustrated in Fig. 1 which is a reproduction of a still photograph of a 5 m/msec aluminum pellet in flight and in Fig. 2 which is a reproduction of a streak photograph of the same pellet. The total length of the luminous trail is approximately 20 ft. Four flashes are visible. The time between flashes is about 0.4 millisecond. The trails of many such pellets have been photographed and each shows a somewhat similar periodicity in flashing although no two pellets behave exactly the same. In some cases a double periodicity is present; for example, there will be a long burst, a short burst, a long burst, and then a short burst. The period also seems to depend upon the size of the pellet. If the original pellet breaks up into several pieces, as it occasionally does, the period of the flashing of the small fragments is usually much less than that of a large pellet.

The mechanisms or mechanism responsible for the flashing of ultra-speed pellets and meteors has been the subject of much informal discussion and speculation among meteoriticists and ballisticians. A number of instantaneous discrete photographs of the pellet in flight have been taken in an effort to establish the mechanics of flashing. The following photographic scheme was used. A narrow slit is placed near and set at a right angle to the trajectory of the pellet. A General Radio High-Speed Camera is used to photograph the object as it passes the slit. The camera is oriented so that the film moves parallel to the trajectory of the pellet. The result is that the pellet as it passes the slit places on the film an image which is a nearly true photograph of the pellet, provided the speed of the image and that of the film are the same. In our case the film speed

* Work supported by Armament Branch, ONR.
[1] W. W. Zimmerman and C. R. Hammond, Contr. Soc. Research Meteorites **2**, 2, 73 (1939).
[2] Luigi G. Jacchia, Harvard Coll. Obs. and Center of Analysis of M.I.T., Tech. Report **3**, 22 (1949).
[3] J. S. Rinehart, Rev. Sci. Instr. **21**, 939 (1950).

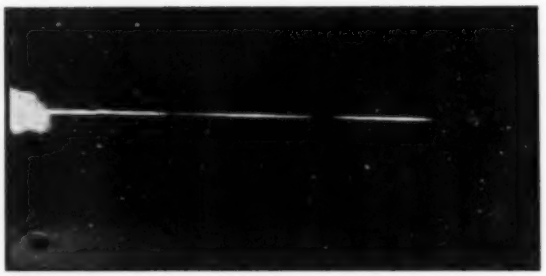

FIG. 1. Still photograph of a 5 m/msec aluminum pellet in flight. Length of luminous trail about 20 ft.

used was approximately one-tenth that of the image so that our photographs are foreshortened by a factor of ten. A typical photograph obtained in this way is reproduced as Fig. 3.

It has been determined from photographs of the type reproduced that the width of the trail ranges from about 1 in. to 3 in. and that its length ranges from 1½ ft to 2½ ft. The width and length of the trail will, of course, fluctuate as the pellet moves through the air.

Examinations of a number of such photographs have shown unambiguously that flashing is associated with yawing of the pellet. Still stereoscopic photographs indicate that, in addition to yawing, the pellet may follow a more or less sinusoidal path or spiral through the air and that the maximum light is given off at the maximum amplitude of the lateral motion. Our data, however, are still too incomplete to describe the detailed motion of the pellet or to establish the aerodynamic conditions under which maximum and minimum ablation will occur.

DEPENDENCY OF MATERIAL AND VELOCITY

The photograph of the smoke trail in Part I and the characteristics of the spectra described in Part II have established that the luminosity can be definitely associated with the burning of eroded material. The contribution to the luminosity made by the shock wave is negligible as has been pointed out in Parts I and II. The material leaves the pellet because energy is supplied to it. The quantity of material must depend upon the energy imparted to the pellet and upon such physical properties of the pellet material as the specific heat, heat of fusion, and heat of vaporization. The amount of dissociation and ionization that occurs within the shock front must also be considered. The exact nature of the way in which these physical properties and processes come into play have not yet been systematically investigated. Unfortunately, our experimental methods do not permit us to vary at will the shape, initial velocity, and mass of the pellet, nor have we developed precise techniques for determining mass loss and changes in shape during flight.

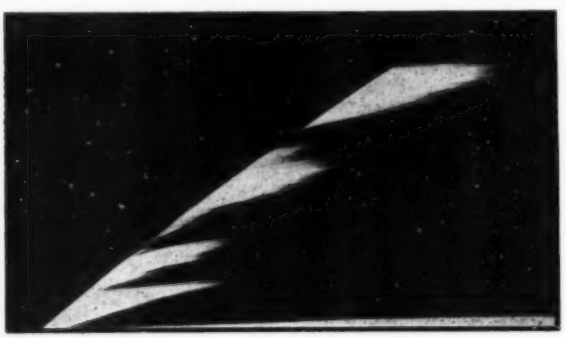

FIG. 2. Streak photograph of pellet shown in Fig. 1.

The form in which the material leaves the pellet has been reasonably well established. The major portion of the material seems to be swept off the surface of the pellet as liquid which rapidly forms into small droplets. One portion of the photograph reproduced in Fig. 2 has been much enlarged in order to show more detail and is reproduced in Fig. 4. Many individual streaks are evident in this enlargement. We have tentatively associated each of these streaks with a small droplet. The droplets are separated in the photograph by virtue of their relative decelerations.

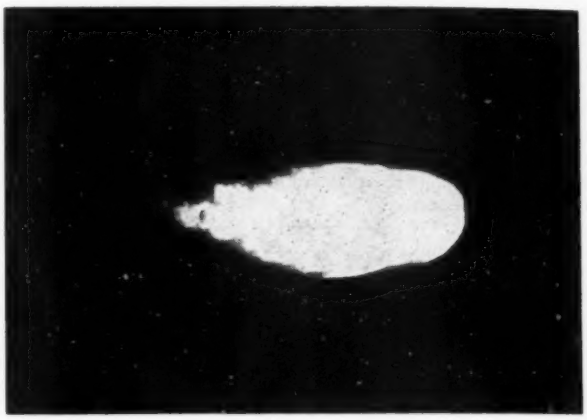

FIG. 3. Photograph of pellet in flight showing luminous trail. Pellet moving from left to right.

We have an opportunity to make limited observations on the effect of velocity on ablation since the pellet is decelerated rapidly in flight. Our conclusions are (a) that at a velocity of 5 m/msec an aluminum pellet loses mass rapidly and the ablated material burns vigorously so as to produce an intensely luminous trail, (b) that at 3 m/msec ablation of aluminum ceases, (c) that at 2.5 m/msec a steel pellet is not brilliantly luminous although faint tracks have been photographed on Shellburst and Super XX film with F/1.5 lens, and (d) magnesium pellets continued to erode material and to burn down to a velocity of 1.5 m/msec.

BRIGHTNESS AND TEMPERATURE

The brightness, luminous output, and temperature of the trail generated by an aluminum pellet have been measured. The sun and a commercial photoflash bulb

were used as brightness standards. A null method of photographic photometry was used to determine brightness. Several successively less intense images of a single bright object of known brightness are impressed on a single photographic plate. At the same time, similar images of the object of unknown brightness are impressed on the same film. Respective images of corresponding brightness are then compared. If the reduction in intensity of successive images and the brightness of the standard object are known, the brightness of the unknown object can be easily determined. A typical photograph obtained for the purpose of comparing the brightness of a pellet with that of the sun is reproduced in Fig. 5. This photograph was taken with the General Radio High-Speed Camera. Thus, the sun appears as a series of streaks extending along the film. The pellet was fired athwart the film. Comparable exposures were insured by setting the camera at such a distance from the trajectory of the pellet that the angular width of the pellet train was equal to the angular width of the sun. Five images of the sun and three images of the pellet are visible. In terms of photographic density, the brightest image of the pellet corresponds in brightness

FIG. 4. A portion of photograph reproduced in Fig. 2, much enlarged to show discrete character of eroded material.

to the third image of the sun. We find, from our calibration, that the image of the pellet is 0.06 times as bright as the sun. The picture was taken at high noon in a cloudless sky. If we assume the brightness of the sun as 500,000 lamberts, the brightness of the image of the pellet is 30,000 lamberts. Similar photographs of a commercial No. 50 flash bulb and an aluminum pellet indicate that the pellet has a brightness of 20,000 lamberts or is about 33 percent as bright as the peak brightness of the flash bulb. The two measurements of brightness are in reasonably close agreement.

A good estimate can be made of the total luminous output of the pellet's trail from a knowledge of the brightness, diameter, and persistance of the trail. If,

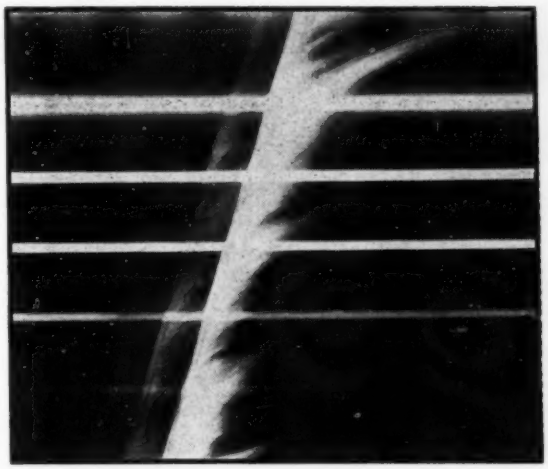

FIG. 5. Streak photograph used to compare brightness of pellet with brightness of sun.

for purposes of estimation, we think of the pellet as an extended light source approximately 2 in. in diameter and 2 ft long that is moving with a velocity of about 4 m/msec and remains luminous for a distance of 20 ft, then the total light emitted is found to be 20,000 lumen-seconds.

A crude independent measure has been made of the luminous output. A photocell integrating light meter was placed so that it was illuminated by a part of the trail. The reading obtained was then reduced to brightness and gave a value of 15,000 lamberts.

The luminosity of the pellet arises primarily from the burning of eroded aluminum. One would expect that the brightness of the trail would be more or less independent of velocity. The photograph in Fig. 5 indicates that this is very nearly the case. The luminous output will not necessarily be the same at all points along the path of the pellet since this quantity will depend upon the amount of material that burns. If the total luminous output is compared with the rated luminous output of the No. 50 flash bulb, all of the light that is emitted by the pellet can be accounted for by the burning of about 15 milligrams of aluminum.

The color temperature of the trail can be obtained from the aforementioned brightness determinations. The color temperature obtained from comparison with the sun is 2970°K and from comparison with the flash bulb, 2890°K. In this connection it should be realized that the effective vibrational temperature derived from spectral data in Part II was found to be 4000°K.

Mechanisms of Positive and Negative Corona in Hydrogen and Argon between Coaxial Cylindrical Electrodes over an Extended Pressure Range

EUGENE J. LAUER*
Department of Physics, University of California, Berkeley, California
(Received August 6, 1951)

Mechanisms in the corona discharge from a fine platinum wire at a positive potential along the axis of a hollow nickel cylinder have been investigated by using the oscilloscope to analyze the pulses caused by α-particles passed through the low field region parallel to the wire. γ_p, the secondary coefficient for the photoelectric effect at the cathode in hydrogen, had values from 70×10^{-5} at 100 mm to 5×10^{-5} at 650 mm pressure. γ_i for the hydrogen ions at the cathode was less than 10^{-4}. The mobility of the positive ions (presumably H_3^+) was 13.4 ($\pm$0.4) cm²/volt×sec at 760 mm and 20°C. Adding 0.1 to 1.0 percent of oxygen to hydrogen resulted in the formation of O_3^- ions. γ_i for the argon positive ions was about 9×10^{-4} extrapolated to zero pressure and decreased with increasing pressure and γ_p was less than $\frac{1}{10}\gamma_i$. Most of the ions were A_2^+ with a mobility of 1.94 ($\pm$0.08) cm²/volt×sec. Positive wire dc current voltage data were taken in hydrogen and argon at several pressures. Sparks occurred with the positive wire in argon at relatively lower gap voltages than in hydrogen. Current-voltage data were taken with the wire negative. In hydrogen the discharge started as a small (10^{-11} amp) self-supporting current (probably uniformly distributed along the wire) which changed with increasing gap voltage to a larger (microampere) discharge localized in luminous spots on the wire in analogy to Miller's observations in nitrogen. No small self-supporting currents were observed in argon. The discharge started as a spark above 200 mm and as a glow that spread uniformly over the wire below 100 mm pressure.

INTRODUCTION

THE study of positive and negative point-to-plane and coaxial wire to cylinder corona discharges in various gases and over broad pressure ranges has shown itself to be an invaluable source of information concerning the various factors leading to the electrical breakdown of gases. The considerable series of studies carried on in the Department of Physics at Berkeley under Professor L. B. Loeb during the last 15 years have contributed a great deal to the knowledge of the breakdown processes. Earlier investigations were carried out by G. W. Trichel,[1] A. F. Kip,[2] G. G. Hudson,[3] and G. L. Weissler[4] on point-to-plane corona. The basic processes having been clearly delineated by these studies, it became of interest to carry the work over to coronas in coaxial geometry, the reasons being first, that such a geometry permits calculations of fields, thresholds, etc., and second, that this is the geometry often used in Geiger counters and proportional counters. The fundamental processes of these counters have been in continuous controversy virtually since the first Geiger-Müller counter was developed in 1928. Studies of the coronas with coaxial geometry in pure nitrogen, pure oxygen, air, and other mixtures of nitrogen and oxygen over extended pressure ranges have recently been carried out experimentally by C. G. Miller and interpreted by Professor Loeb.[5]

The present work was undertaken to extend the investigations of this geometry to pure hydrogen and the inert gases.

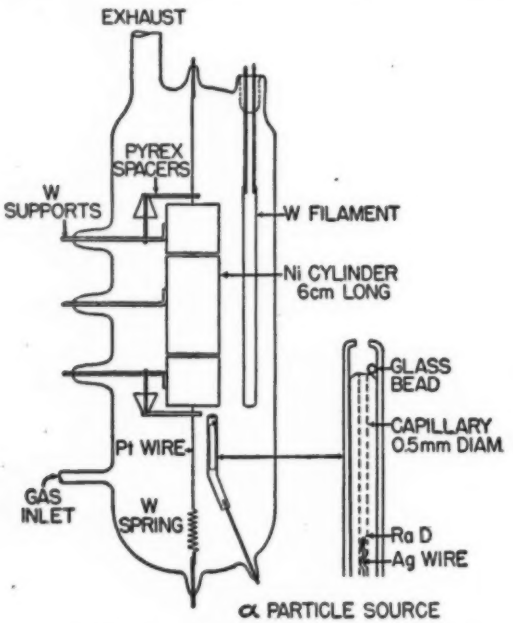

FIG. 1. Discharge tube and α-particle source.

EXPERIMENTAL TECHNIQUES

The most direct information about the mechanisms occurring in the discharge was obtained by using the oscilloscope to observe pulses resulting from α-particle ionization. The wire was at a positive potential and an α-particle from a collimated source passed through the low field region parallel to the axis of symmetry of the electrodes (see Fig. 1). (The α-particle passes in about 10^{-8} second and with good collimation can give a sharply defined region of initial ionization.) The initial electrons produced along the path of the α-particle moved into the wire and multiplied by collision in the high field region. The resulting pulse was amplified and fed to the synchroscope and recorded photographically. The primary burst of ionization near the wire triggered the synchroscope sweep, and the subsequent

* This work was supported by ONR funds.
[1] G. W. Trichel, Phys. Rev. 55, 382 (1939).
[2] A. F. Kip, Phys. Rev. 55, 549 (1939).
[3] Loeb, Kip, and Hudson, Phys. Rev. 60, 714 (1941).
[4] G. L. Weissler, Phys. Rev. 63, 96 (1943).
[5] C. G. Miller and L. B. Loeb, J. Appl. Phys. 22, 494 (1951); 22, 614 (1951); 22, 740 (1951).

signal was used to analyze the mechanisms which take place. Positive and negative wire current-voltage curves were also taken.

Figure 1 shows the discharge tube and α-particle source. Except for the α-particle source, the discharge tube was closely similar to that used by C. G. Miller. The platinum wire was 0.00635 ($\pm$0.0003) cm in radius and the nickel cylinders were of 1.45 ($\pm$0.005) cm inside radius. The glass bead could be bounced off or onto the capillary hole of the collimator by tapping the discharge tube. This was convenient for turning the α-particle beam on and off to aid in identifying the pulses.

The discharge tube was baked out and the electrodes were outgassed at a red heat. The nickel cylinders were heated by electron bombardment from the tungsten filament and the platinum wire was heated by passing a current through it.

The hydrogen was electrolytically prepared steel tank gas passed over hot copper and through a liquid nitrogen trap. The argon was Air Reduction Company gas stored in glass flasks.

"B" batteries were used for the potential source.

A Tektronix Type 511A synchroscope and Type 121 preamplifier together with a variable RC (RC=0.03 to 3 μsec with $R=10^3$ to 10^5 ohms) across the output of the discharge tube constituted the oscilloscope circuit.

MOBILITY OF THE IONS IN THE POSITIVE WIRE HYDROGEN CORONA

The mobility of the ions in the positive wire hydrogen corona was determined by measuring the time for the ions to go from the wire to the cylinder. The synchroscope sweep was triggered by the large pulse caused by the formation of the ion sheath. The amplitude in the tail of the pulses (Fig. 2) is proportional to the current resulting from the motion of the ion sheath, and the current drops suddenly from a finite value to zero when the ions hit the cathode with a finite drift velocity. The current does not drop discontinuously to zero when the ion sheath reaches the cathode in virtue of diffusion and because the sheath has a finite thickness.

The transit time was measured and substituted into the following equation to obtain the mobility:[6]

$$k=\frac{b^2 \ln b/a}{2\tau(V_0+2Q_0 \ln b/a)},$$

where b=radius of the cathode cylinder, a=radius of the wire anode, V_0=potential across the gap, τ=transit time for the first ions to reach the cylinder, and Q_0 =charge per unit length in the ion sheath. Q_0 was obtained by measuring the pulse height (in volts) on the oscilloscope and multiplying by the capacity per unit length of the discharge tube and amplifier input. This space charge correction amounted to from 0.2 to 3.0 percent.

[6] H. Den Hartog and F. A. Muller, Physica **15**, 789 (1949).

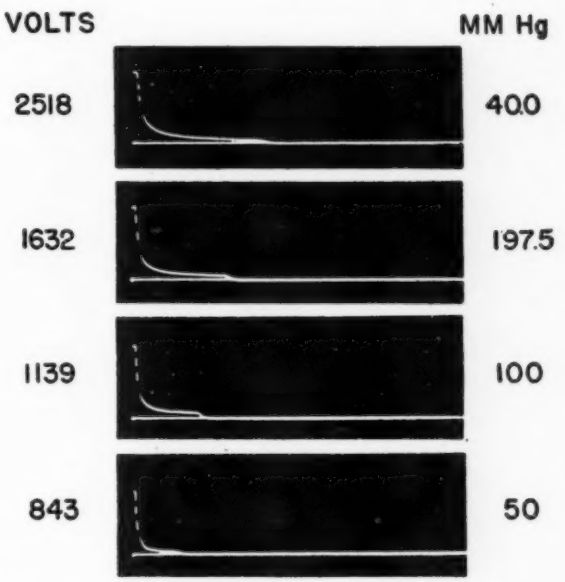

FIG. 2. α-particle pulses followed by current due to motion of positive ion sheath, hydrogen, 200 μsec full scale.

Figure 3 shows the measured values of $1/k$ plotted against pressure together with a straight line through the origin fitted to the data by least squares. The data points represent averages of from 2 to 5 measurements at the various pressures. The mobility extrapolated to a gas density corresponding to 760 mm and 20°C is 13.4 ($\pm$0.4) cm^2/volt$\times$sec.

The main purpose of this measurement is to identify the ions present in the discharge rather than to make an accurate mobility measurement. Although the electric field is not constant along the path of the ions, the ions spend most of their time in a relatively low E/p (electric field strength over pressure); e.g., at 650 mm the ions only spend 1 percent of their time in an E/p greater than 7 volts/cm$\times$mm. Table I summarizes the results of various authors for the mobility of hydrogen

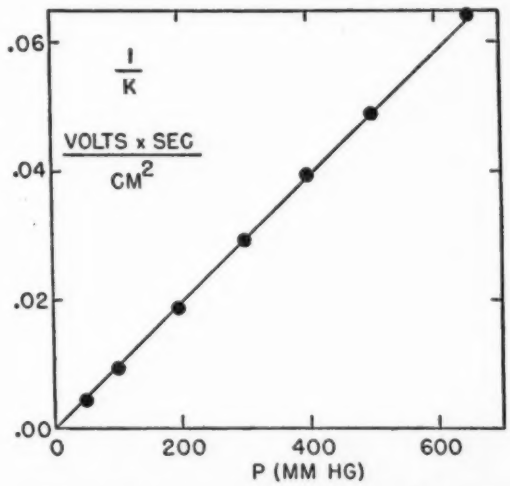

FIG. 3. Reciprocal mobility *vs* pressure, hydrogen ions in hydrogen.

TABLE I. Mobility of hydrogen ions in hydrogen (cm^2/volt×sec). 760 mm 20°C.

E. J. Lauer	13.4 (±0.4)
N. E. Bradbury[a]	13.1 (±0.3)
	8.2
J. H. Mitchell[b]	14.7
	13.8
H. R. Hasse' and O. W. R. Cook[c]	18 or 19

[a] N. E. Bradbury, Phys. Rev. **40**, 508 (1932).
[b] A. M. Tyndall, *The Mobility of Positive Ions in Gases* (Cambridge University Press, London, 1938), p. 53.
[c] H. R. Hasse' and O. W. R. Cook, Phil. Mag. **12**, 554 (1931).

ions in hydrogen. Lauer's 13.4, Bradbury's 13.1, and Mitchell's 13.8 mobility could all be the same ion. Bradbury's ions were 10,000 μsec old and most of them had the 8.2 mobility. Lauer's ions were from 30 to 100 μsec old and only the 13.4 mobility was detected. It is possible that Bradbury's ions all started as the fast type and most of them changed to the slow type during their transit time which was about 100 times longer than in Lauer's measurement. Mitchell got values from 13.8 to 14.7 and believed that the smaller values were due to an impurity effect. In case the ions in the present experiment are impurity ions, they must have been completely formed from hydrogen ions within 5 μsec in order for the current to have such a sharp discontinuity when the ions hit the cylinder. Since the hydrogen ions make about 3×10^3 collisions in 5 μsec at 50-mm pressure, the impurity would have to compose about 0.04 percent of the gas if an impurity ion were formed every time a hydrogen ion collided with an impurity molecule. Such a high probability for charge transfer is not common. This amount of *oxygen* could not have been present (compare Figs. 2 and 8 for the effect of adding oxygen to the hydrogen). The electrolytically prepared tank hydrogen could contain 0.04 percent of an impurity such as nitrogen which would not be removed by the hot copper tube or liquid nitrogen trap, but N_2 would not give up an electron to H_2^+.

The classical kinetic theory calculation of Hasse' and Cook for the mobility of H_2^+ ions in H_2 gas gives 18 or 19 depending upon the force law used. No calculation has been made taking account of the exchange energy of interaction between an H_2^+ ion and an H_2 molecule with identical nuclei and the probability for transfer of the electron in the case of exact resonance of the ionization potentials. These effects would increase the collision cross section that is used in diffusion and mobility calculations and result in a calculated mobility agreeing more closely with the 13.4 observed.

MOBILITY OF THE IONS IN THE POSITIVE WIRE ARGON CORONA

Figure 4 shows the argon ion pulses and Fig. 5 is the plot of $1/k$ *vs* pressure. The pulses differ from those in hydrogen in that there is a pulse of secondary electrons released when the ions reach the cathode. In some of the pictures several orders of secondary peaks can be seen.

The mobility reduced to a gas density corresponding to 760 mm and 20°C is 1.94 (±0.08) cm^2/volt×sec. The results of various authors on the mobility of argon ions in argon are summarized in Table II. Hornbeck has used helium, neon, and argon in a cylindrical tube and obtained pulses similar to these. He used photoelectric triggering from the cathode and his pressures were of the order of 1 mm. He found two ions in each of the above rare gases and has good arguments for identifying the slow ion in each case as the atomic ion (e.g., A^+) and the fast ion as the molecular ion (e.g., A_2^+).[7] Holstein has calculated the mobility of A^+ in A taking account of the special contributions to the diffusion cross section that arise for an ion moving in its own gas and obtained 1.64. Munson and Tyndall measured the mobility of argon ions in argon and assigned 1.94 for what they thought was A^+. This is the mobility obtained in the present experiment for what is now known to be A_2^+.

SECONDARY ELECTRONS DUE TO POSITIVE IONS AT THE CATHODE

The argon ion transit pictures show a pulse due to secondary electrons released when the ions reach the cathode (Fig. 4). Simple theory predicts that the ratio r of the number of ions in the nth secondary pulse to

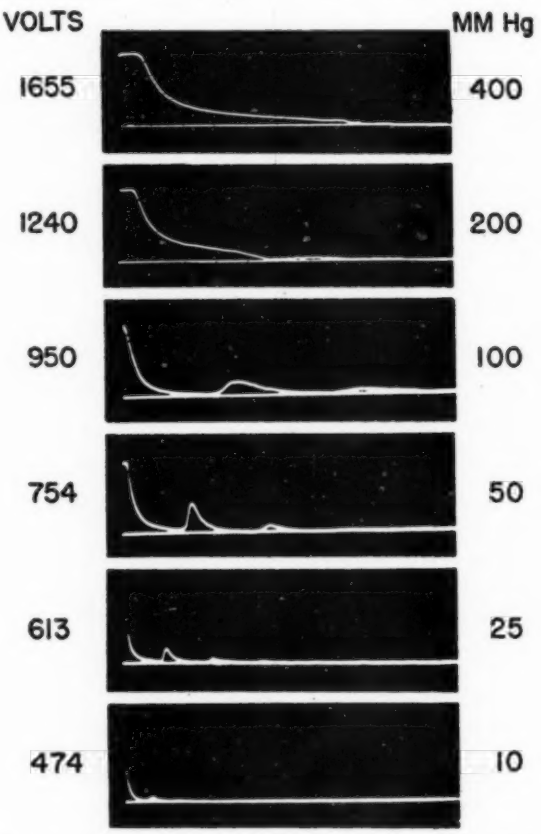

FIG. 4. α-particle pulses followed by secondary pulses due to positive ions at the cathode, argon, 1000 μsec full scale.

[7] J. A. Hornbeck, Phys. Rev. **80**, 297 (1950).

those in the $(n-1)$th is

$$r=\gamma M,$$

where M is the gas multiplication factor and γ is the average number of electrons released per ion incident at the cathode. In this experiment γ is evaluated by measuring r, the ratio of the *areas* under successive peaks (since the oscilloscope deflection is proportional to current) and dividing by M. M is obtained from a separate measurement discussed later. The apparent values of γ observed at the various pressures are listed in Table III. Since E/p at the cylinder is only 0.5 to 3 volt/cm×mm, the positive ions hit the cathode with very little more than the thermal kinetic energy of about 0.03 ev. The measured values of γ decrease with increasing pressure. This effect is to be expected since part of the electrons originally released from the cathode are returned by back diffusion due to collisions with gas molecules. The simple theory[8] for the pressure dependence of the number of electrons escaping back diffusion is

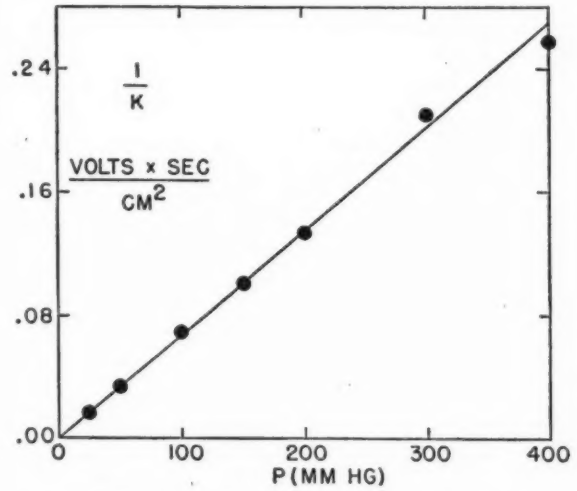

FIG. 5. Reciprocal mobility *vs* pressure, argon ions in argon.

$$\gamma=\gamma_i/(1+Ap),$$

where γ_i is the value γ would have if there were no back diffusion, A is a constant, and p is the pressure. The measured values of γ appear to have a pressure dependence of this form. γ_i is about 8.5×10^{-4}. The accuracy of the measurements is not better than ±20 percent.

Earlier work on the liberation of secondary electrons by inert gas ions has usually been for the case of *atomic* ions with volts of kinetic energy from surfaces in vacuum e.g., M. L. E. Oliphant[9] (with no back diffusion loss) found a γ from 0.3 at 80 volts kinetic energy to 1.2 at 1000 volts for He^+ ions on a cold molybdenum surface. γ_i for A_2^+ ions with 0.03 ev kinetic energy would be expected to be smaller since γ_i is thought to depend upon the relative ionization potential of the atom, the work function of the surface, and upon the kinetic energy of the ion.[10] Back diffusion can reduce the effective γ by another power of ten or more depending on the pressure.

TABLE II. Mobility of argon ions in argon, (cm^2/volt×sec), 760 mm, 20°C.

	A^+ in A	A_2^+ in A
E. J. Lauer		1.94 (±0.08)
J. A. Hornbeck[a]	1.5 (±0.1)	1.9
R. J. Munson and A. M. Tyndall[b]		1.94
T. Holstein[c]	1.64	

[a] Private communications from J. A. Hornbeck to Professor L. B. Loeb.
[b] R. J. Munson and A. M. Tyndall, Proc. Roy. Soc. (London) A177, 187 (1941).
[c] T. Holstein, Phys. Rev. 85, (A) (1952).

No secondary electron pulse can be detected when the hydrogen ions, presumably H_2^+, hit the cathode (Fig. 2). This sets an upper limit of $\gamma_i<10^{-6}$ for these hydrogen ions of thermal energy incident upon a nickel surface.

PHOTOELECTRONS FROM THE CATHODE IN POSITIVE WIRE CORONA

With a ten times faster sweep speed (and also a shorter *RC* constant where the signal is picked up from the discharge tube, e.g., 0.03 μsec instead of 0.3 μsec) the initial pulse of the hydrogen ion pulses (Fig. 2) is found to have a fine structure (Fig. 6). These pulses are due to photoelectrons released from the cathode by the photons radiated from the region of dense excitation and ionization around the positive wire. They are analogous to the argon ion secondary pulses except that now the period between pulses is the time for *electrons* to cross from the cylinder to the wire. Each of the pictures in Fig. 6 consists of 100 superimposed α-particle pulses. Single α-particle pulses could not be recorded on the photographic film at this sweep speed.

In order to ascertain whether the period between pulses corresponds to the transit time of electrons, the measured times were compared with the times calculated from direct measurements of electron drift velocity.[11] The drift velocity is proportional to $(E/p)^{\frac{1}{2}}$

TABLE III. Apparent γ for A_2^+ on Ni at thermal energy.

Pressure (mm)	γ
25	7.8×10^{-4}
50	7.0×10^{-4}
100	4.0×10^{-4}
200	0.6×10^{-4}
400	0.2×10^{-4}

[8] J. J. Thomson, *Conduction of Electricity Through Gases* (Cambridge University Press, Cambridge, 1928), 3rd edition, Vol. 1, p. 466.
[9] M. L. E. Oliphant, Proc. Roy. Soc. (London) A 127, 373 (1930).
[10] M. L. Oliphant and P. B. Moon, Proc. Roy. Soc. (London) A 127, 388 (1930).
[11] R. A. Nielsen and N. E. Bradbury, Phys. Rev. 49, 388 (1936).

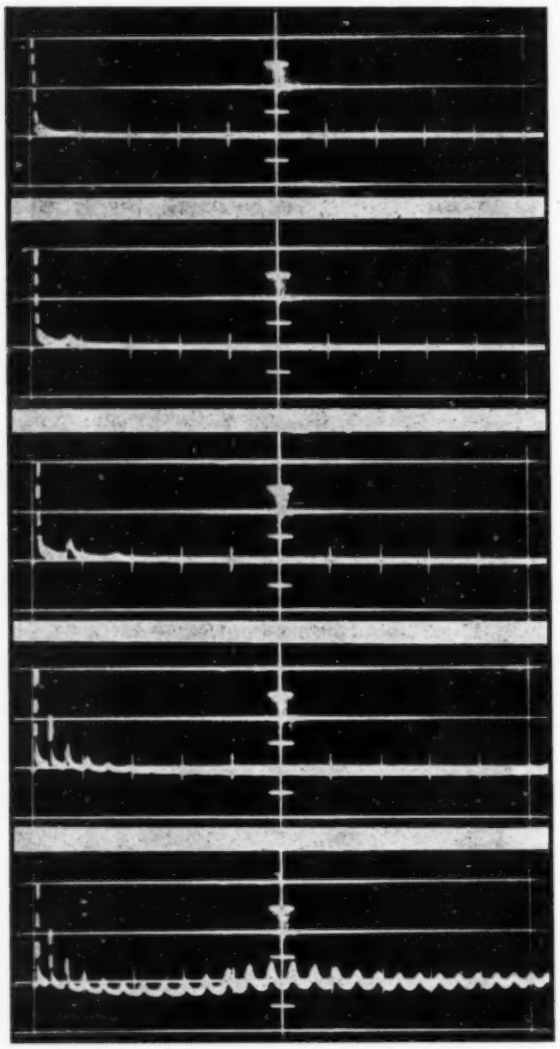

FIG. 6. α-particle pulses followed by secondary pulses due to photoelectrons from the cathode, hydrogen, 400 mm Hg, upper three pulses are 10 μsec full scale, lower two pulses are 20 μsec full scale. Gap volts from top to bottom: 2200, 2400, 2500, 2600, 2700.

over most of the range of E/p involved. The measured and calculated transit times are given in Table IV and agree within the experimental error.

The ratio of the number of ions in the nth to those in the $(n-1)$th pulse is

$$r=\gamma_p M.$$

γ_p is the number of photoelectrons released from the cathode per ion formed in the gap, and γ_p may be broken down into a product of several factors: (a) the number of photons (with energy greater than the work function of the cathode) radiated per ionization, (b) the probability that a photon which is radiated from a point near the wire goes in a direction to hit the cathode and does not get absorbed in the gas, (c) the probability that an electron is released from the cathode if one of these photons is incident, and (d) the probability that an electron which is released from the cathode escapes being captured by back diffusion. Actually γ_p is the sum of the values of the individual γ_{pi} corresponding to the various energies of the photons (i) which are radiated. The value of γ_p is determined by measuring r (the ratio of the amplitude of the nth to the $(n-1)$th pulse), and dividing by M. The values of γ_p at the various pressures are listed in Table V. The accuracy is not better than ± 20 percent.

γ_p decreases with increasing pressure and this is consistent with the fact that back diffusion and photon absorption in the gas both increase with increasing pressure.

Above a critical gap voltage the pulses become self-sustaining and do not terminate. For a particular gap voltage M and γ_p adjust themselves (by adjusting the space charge) until $r=1$ on the average. Figure 7 shows some of these pulses near the self-supporting corona onset potential. These are triggered by background ionization. The period between pulses is independent of external circuit constants. If a pulse series lasts more than a few hundred microseconds, different series operate simultaneously in various phases and the sharply separated pulses cannot be observed. Electron diffusion also broadens the pulses.

Over most of the range of pressures no pulses with separation corresponding to the transit time of electrons could be detected in argon. At the highest pressures one or two small secondary pulses could be seen that were probably photoelectrons from the cathode. L. Colli, U. Facchini, and E. Gatti[12] on the other hand, obtained photoelectric pulses with argon similar to those obtained in the experiment with hydrogen. They had a brass cathode and found a value of γ_p of about 10^{-3}. It should be noted that whichever of several secondary coefficients is larger will cause the discharge to become self-sustaining at a gap potential (and corresponding M) too small to allow detection of the pulses involving a much smaller γ. Thus it is concluded that in the present experiment (argon with an outgassed nickel cathode) the ion γ_i is larger than the photoelectric γ_p, whereas in the study with argon and a brass cathode (which has a lower work function) the photoelectric coefficient appears to have been larger than the ion one.

EFFECT OF A SMALL AMOUNT OF OXYGEN IN HYDROGEN

In some of the hydrogen runs a small amount (0.1 and 1.0 percent) of oxygen was added to the hydrogen.

TABLE IV. Electron transit time, hydrogen.

Pressure (mm)	Gap volts	Transit time (μsec) Meas	Calc
650	3400	1.12	1.13
400	2500	1.02	1.02
200	1650	0.90	0.88
100	1135	0.77	0.75

[12] Colli, Facchini, and Gatti, Phys. Rev. **80**, 92 (1950).

TABLE V. γ_p for hydrogen photons on nickel.

Pressure (mm)	γ_p
650	4.9×10^{-5}
400	7.4×10^{-5}
200	15×10^{-5}
100	69×10^{-5}

This might be expected to result in (a) attachment of electrons to O_2 molecules to produce slow negative ions and (b) increased photoionization in the gas.

Figure 7 includes pictures of the (nearly) self-sustaining photoelectric corona pulses with oxygen added to the hydrogen. It is seen that the secondary pulses fall off faster with oxygen present.

Figure 8 shows how the *ion* pulses are changed by adding oxygen (compare with Fig. 2). The *RC* is small in so far as the current due to ion motion is concerned but is long for seeing the pulses due to electron motion when avalanches occur. It appears that some of the photoelectrons starting from the cathode have been trapped by oxygen molecules after going various fractions of the gap distance. The arrival of the electrons at the wire is then delayed and the electrons detach from the oxygen molecules to produce new avalanches when the O_2^- ions get in the high field region near the wire.

It is difficult to detect the expected photoionization *in the gas* when oxygen is added to hydrogen in this experiment because the gas photoelectrons are created with a continuous distribution in the gap and so do not produce a sharp pulse similar to that due to cathode photoelectrons. The tail of the photoelectric pulses (i.e., the signal *between* cathode pulses) is composed of (a) current due to ion sheath motion, (b) *RC* decay, and (c) possibly photoelectrons from the gas. These are difficult to separate and further work is needed to devise techniques for observing photoionization in the gas.

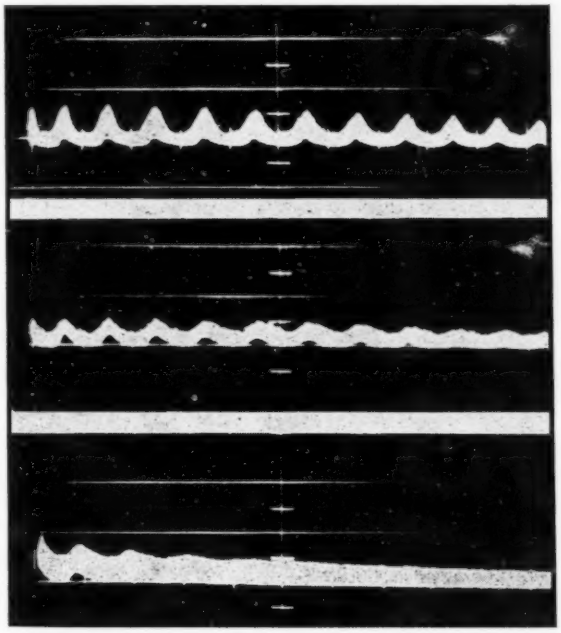

FIG. 7. Nearly nonterminating corona pulses, upper picture pure H_2, middle picture $H_2+0.1$ percent O_2, lower picture $H_2+1.0$ percent O_2, 10 μsec full scale.

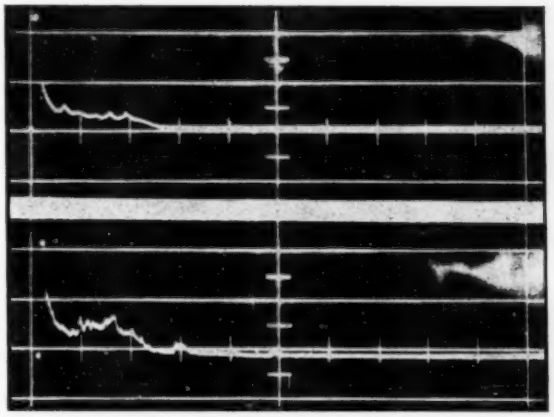

FIG. 8. α-particle pulses followed by current due to positive ion sheath motion with superimposed pulses due to delayed arrival of cathode photoelectrons at wire. Upper pulse $H_2+0.1$ percent O_2, lower pulse $H_2+1.0$ percent O_2, 500 μsec full scale.

POSITIVE WIRE GAS MULTIPLICATION CURVES

The gas multiplication factor M is needed in order to evaluate the secondary electron coefficients from the observed pulse ratios. The most direct way to measure M as a function of gap voltage is to measure the number of ions n, in the primary pulse from the α-particle at a particular voltage, and also measure the number of ions at a voltage low enough so that the initial n_0 ions from the α-particle are collected without multiplication. Then

$$M=n/n_0.$$

This is essentially what was done except that the amplifier did not have sufficient gain to see the n_0 ions from the α-particle without multiplication. At the highest pressures in hydrogen the α-particle pulses would produce a significant deflection on the oscilloscope with $M=20$ and in argon with $M=2$. An electrometer was used to measure the total current due to a γ-ray source as a function of voltage and the n/n_0 curve obtained from the pulses was joined to the J/J_0 curve at the lowest gap voltage for which the oscilloscope pulses were significant. The gas multiplication curves are shown in Figs. 9 and 10. The $\log(J/J_0)$ curves do not rise above the $\log(n/n_0)$ curves until M is about 50, so that probably not much error is introduced by combining the current and pulse measurements. At the lower pressures the initial ionization could not be measured even with the electrometer, so that n_0 was calculated from the measured value at a higher pressure by assuming the range of the α-particle to be inversely proportional to the pressure, and numerically integrat-

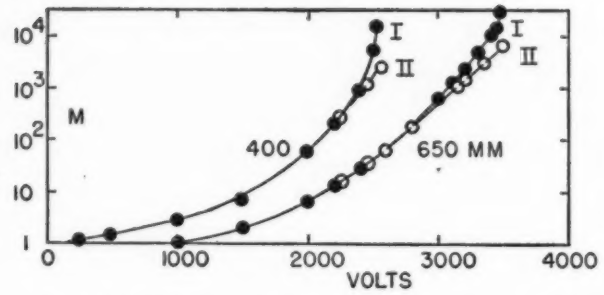

FIG. 9. Gas multiplication *vs* gap voltage, hydrogen, positive wire, I by total current due to γ-ray source, II by α-particle pulses with short *RC*.

ing an experimental curve of the rate of ionization along the path of an α-particle.[13]

POSITIVE WIRE CURRENT *VS* GAP VOLTAGE CURVES

Curves of dc current *vs* gap voltage for the positive wire in hydrogen and argon were taken at several pressures in the range from 25 to 650 mm (Figs. 11 and 12). These data are similar to those of C. G. Miller and L. B. Loeb[5] for the positive wire in nitrogen and oxygen. At voltages below the self-supporting corona onset potential the current represents the difference which was observed due to bringing a γ-ray source (thorianite ore) near the discharge tube. Above the self-supporting corona onset potential the current continues once started without initial ionization from an external source. In both gases and at all pressures the current became self-sustaining at about 0.1 to 1.0 microampere collected at the 6-cm long center cylinder. The initial ionization current without gas multiplication could only be detected at the highest pressures where it was from 10^{-14} to 10^{-13} ampere.

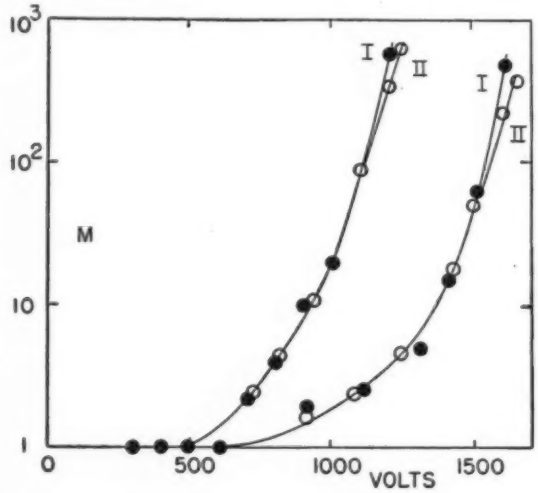

FIG. 10. Gas multiplication *vs* gap voltage, argon, positive wire, I by total current due to γ-ray source, II by α-particle pulses with short *RC*. Upper curves—200 mm Hg; lower curves—400 mm Hg.

[13] J. D. Stranathan, *The Particles of Modern Physics* (The Blakiston Company, Philadelphia, 1942).

In both gases the discharge first became visible above the self-supporting corona onset with tens of microamperes of current as a blue glow uniformly covering the wire surface. On the argon curves of Fig. 12 there are vertical arrows indicating where a spark occurred. No spark occurred with hydrogen although the curves were continued to relatively higher voltages above the self-supporting corona onset than the argon curves were. G. L. Weissler[4] found no corona at all with the positive *point in argon at atmospheric* pressure. As his gap voltage was raised, the ionization current was followed by a spark. The fact that argon seems to spark at lower gap voltages than hydrogen does might be associated with a greater probability for photoionization in the argon which would contain molecules in metastable states.

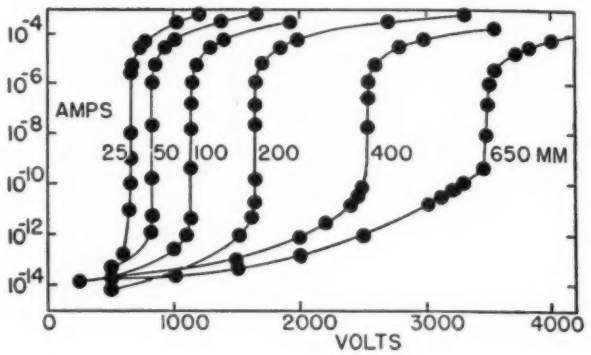

FIG. 11. Current *vs* gap volts, hydrogen, positive wire.

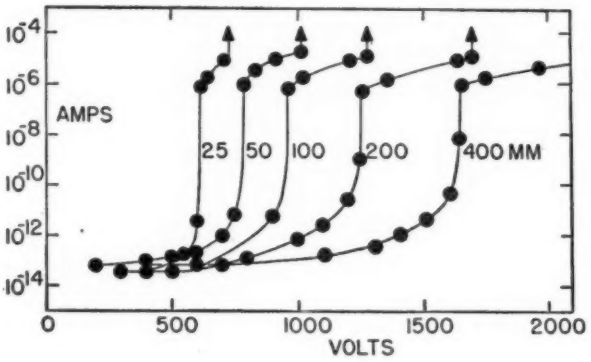

FIG. 12. Current *vs* gap volts, argon, positive wire.

NEGATIVE WIRE DATA

The gap current was also measured with the wire negative.

In hydrogen (Fig. 13) there were small (about 10^{-11} ampere) self-sustaining currents which are indicated by the dotted lines. At a higher voltage indicated by the vertical line with the arrow pointing up, the current jumped suddenly to a much larger value (of the order of 100 microamperes) and was only limited by the resistance in the power supply. The voltage could be lowered somewhat below the onset potential before the

current dropped suddenly to the small value. Visually no light could be seen until the microampere currents started when one or more localized spots of light appeared on the wire surface. This behavior of the negative wire in hydrogen is similar to the case of the negative wire in nitrogen as observed by C. G. Miller and L. B. Loeb.[5] The small predischarge current was probably supported mainly by the photoelectric effect at the wire surface since the ion γ was shown to be small. The sudden jump to a much larger current may be ascribed to a clean up of the wire surface at localized spots by positive ion bombardment resulting in a larger γ. The gas multiplication may have been increased by the increase in the electric field near the wire by positive ion space charge.[14]

The negative wire data for argon are given in Table VI. With argon pressures greater than 200 mm no current was observed as the gap potential was increased until a spark occurred. This is what Weissler

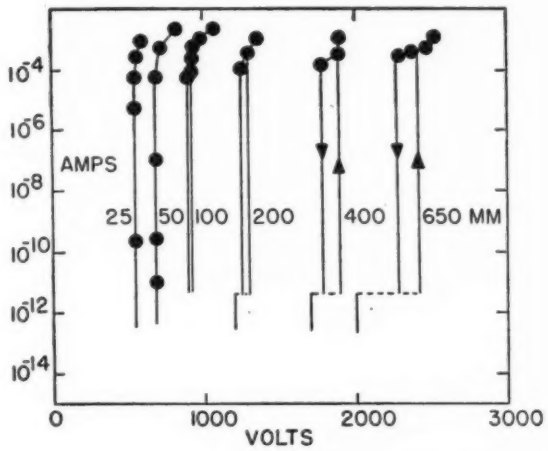

FIG. 13. Current *vs* gap volts, hydrogen, negative wire.

observed with the negative point in argon at atmospheric pressure.[4] At the lower pressures, the corona

[14] L. B. Loeb, Phys. Rev. **76**, 255 (1949).

TABLE VI. Argon negative wire data.

Pressure (mm)	Gap volts	Remarks
25	286	Onset uniform glow, 10 μamp, followed upon waiting by spark
50	392	onset uniform glow, 1 μamp
	424	spark
100	529	onset uniform glow, 1 μamp
	530	spark
200	900	spark
400	1000	spark

started as a blue glow spread uniformly over the wire. The appearance was similar to that observed with the positive wire in both argon and hydrogen and is to be contrasted with the localized spots on the negative wire in hydrogen. With the high values of γ for ions and metastable atoms in the inert gases, the clean-up phenomena characteristic of H_2 and N_2 are not required. Argon showed a relatively large ion γ-effect at the negative cylinder and this was probably also the case at the negative wire especially since the kinetic energy of the ions was larger at the wire. There was probably also some metastable γ-effect although this could not be measured by these techniques. At the lower pressures these γ-effects resulted in a glow discharge at gap voltages too low for a spark to occur. At higher pressure (and lower E/p) the effective γ is reduced and α/p is low, but once a low order self-sustaining discharge begins space charges become heavy, leading to a streamer spark as Fisher and Kachikas have recently shown.[15]

The author wishes to thank Professor L. B. Loeb, at whose suggestion this problem was undertaken, for his advice and guidance during its prosecution and especially for his assistance in the interpretation of some of the more complex phenomena observed.

[15] G. A. Kachikas, Ph.D. thesis, "Formative time lags of spark breakdown in nitrogen, argon, and oxygen," New York University, August, 1950.

Statistical Theory of Rubber-Like Elasticity. V. The Stress Birefringence*

AKIRA ISIHARA, NATSUKI HASHITSUME, AND MASAO TATIBANA
Department of Physics, Faculty of Science, University of Tokyo, Tokyo, Japan
(Received August 2, 1951)

The effects of network formation of non-Gaussian chains on the stress-birefringence are calculated. If the birefringence is plotted against the stress, the effects make the curve deviate from a straight line. When it is plotted against the elongation, the curve will rise above that corresponding to independent Gaussian chains in agreement with the experiments.

INTRODUCTION

THE stress birefringence is a useful tool for the investigation of the elastic properties of elastomers. As usual, elastomers are considered to have an ideal network structure such as represented by low vulcanized rubber. The statistical treatment of birefringence has been worked out by several authors.[1] They first pick out a single chain from the network, consider its optical properties, and then take the mean value of the results over possible orientations of such independent chains.

However, as has been investigated by Treloar,[2] some "deviation from the statistical theories" arises in the case of two-dimensional stretching of the sample. In addition to this, the Gaussian-chain-approximation is not suitable for the explanation of the characteristic *S*-shape of the stress-strain curve of these materials. Since these difficulties have been removed[3] by using a network composed of non-Gaussian chains, we wish further to calculate the birefringence with respect to such network, and to see the difference of the results from those of the Gaussian independent chain.

THEORY OF THE BIREFRINGENCE

As in the previous papers,* we shall assume that the network of our elastomers is ideal and use the similar notations with respect to the *free* and *fixed* junctions: the Roman suffices $i, j, \cdots$ are used for free junctions and the Greek $\alpha, \beta, \cdots$ for fixed junctions, whereas $a, b, \cdots$ for both kinds of junctions. In a coordinate system xyz fixed in space, let us consider a chain connecting the junctions a and b in positions $\mathbf{r}_a$ and $\mathbf{r}_b$, respectively, and designate the direction of the line connecting these junctions by (Θ_{ab}, Φ_{ab}). Taking this line as a polar axis, we shall define the distribution function $n_{ab}(\omega_{ab})=n_{ab}(\theta_{ab}, \varphi_{ab})$ of the orientation of the elements of the ab-chain. The calculations of the previous papers show that $n_{ab}(\omega_{ab})$ is a function only of the polar angle θ_{ab} and is expressed as

$$n_{ab}(\omega_{ab})=(1/\lambda_{ab})\exp(\mu_{ab}\cos\theta_{ab}), \tag{1}$$

where λ_{ab} and μ_{ab} are the constants determined by the conditions

$$\int n_{ab}(\omega_{ab})d\omega_{ab}=N_{ab},$$
$$\int n_{ab}(\omega_{ab})\cos\theta_{ab}d\omega_{ab}=|\mathbf{r}_a-\mathbf{r}_b|/l, \tag{2}$$

the ab-chain being considered to be composed of N_{ab} elements having the same length l.

Now, we shall suppose that an element of the chains of the network is optically symmetrical around its skeletal axis and has the following polarizability tensor in its diagonal form:

$$\boldsymbol{\alpha}=\begin{pmatrix}\alpha_1 & 0 & 0\\ 0 & \alpha_2 & 0\\ 0 & 0 & \alpha_3\end{pmatrix};\quad \alpha_1=\alpha_2. \tag{3}$$

In general, if the element has the orientation (θ, φ), its polarization tensor referred to xyz-coordinate system assumes the form:

$$\boldsymbol{\alpha}=a\mathbf{1}+b\begin{pmatrix}\sin^2\theta\cos^2\varphi-\frac{1}{3}, & \sin^2\theta\sin\varphi\cos\varphi, & \sin\theta\cos\theta\cos\varphi,\\ \sin^2\theta\sin\varphi\cos\varphi, & \sin^2\theta\sin^2\varphi-\frac{1}{3}, & \sin\theta\cos\theta\sin\varphi,\\ \sin\theta\cos\theta\cos\varphi, & \sin\theta\cos\theta\sin\varphi, & \cos^2\theta-\frac{1}{3}\end{pmatrix}, \tag{4}$$

$$a=\tfrac{1}{3}(2\alpha_1+\alpha_3) \quad \text{and} \quad b=\alpha_3-\alpha_1.$$

* The preceding articles of this series are: I. T. Sakai and A. Isihara, J. Phys. Soc. Japan **3**, 171 (1948); II. A. Isihara, J. Phys. Soc. Japan **3**, 289 (1948); III. T. Sakai and A. Isihara, J. Colloid Sci. **4**, 71 (1949); IV. Isihara, Hashitsume, and Tatibana, J. Chem. Phys. (to be published).

[1] H. Müller, Kolloid Z. **95**, 138 (1941); W. Kuhn and F. Grün, Kolloid Z. **101**, 248 (1942); L. R. G. Treloar, Trans. Faraday Soc. **43**, 277 (1947); *The Physics of Rubber Elasticity* (Oxford University Press, London, 1949); R. Kubo, J. Phys. Soc. Japan **2**, 84 (1947).

[2] L. R. G. Treloar, Proc. Phys. Soc. (London) **60**, 135 (1948).

[3] See article IV of reference 1.

The relation between the three directions (θ, φ), (Θ_{ab}, Φ_{ab}) and $(\theta_{ab}, \varphi_{ab})$ is shown in Fig. 1, which gives

$$\cos\theta_{ab}=\cos\theta\cos\Theta_{ab}+\sin\theta\sin\Theta_{ab}\cos(\varphi-\Phi_{ab}). \quad (5)$$

Hereafter we shall assume that stresses of magnitude l_x, l_y, and l_z are applied in the x, y, and z directions, the corresponding extension ratios being L_x, L_y, and L_z, respectively. In order to calculate the optical birefringence of the network, we must sum up such component polarizabilities as given by Eq. (4) over all the elements of the network in unit volume:

$$\mathbf{P}=\sum_{ab}\int \boldsymbol{\alpha} n_{ab}(\omega_{ab})d\omega_{ab}. \quad (6)$$

The integration can readily be effected if we remember that all the elements of the polarizability tensor are the spherical harmonic function $Y_2(\theta, \varphi)$ of the second order, and that the distribution function depends only on θ_{ab}:

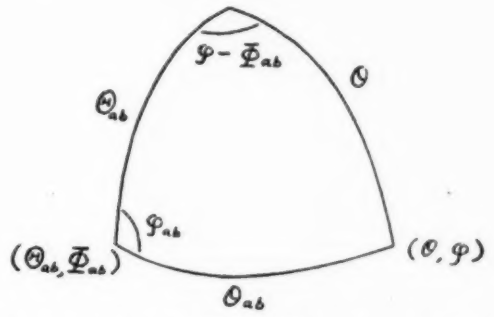

FIG. 1. Orientations of ab-chain (Θ_{ab}, Φ_{ab}) and of an element (θ, φ), the latter being in the direction $(\theta_{ab}, \varphi_{ab})$ referred to the direction of the former.

$$\int Y_2(\theta,\varphi)n_{ab}(\omega_{ab})d\omega_{ab}=Y_2(\Theta_{ab},\Phi_{ab})\frac{4\pi}{\lambda_{ab}\mu_{ab}}\left(\sinh\mu_{ab}-\frac{3\cosh\mu_{ab}}{\mu_{ab}}+\frac{3\sinh\mu_{ab}}{\mu_{ab}^2}\right) \quad (7)$$

$$=Y_2(\Theta_{ab},\Phi_{ab})F(\lambda_{ab},\mu_{ab}).$$

Thus, the polarizability tensor becomes

$$\mathbf{P}=aN\mathbf{1}+\frac{b}{15}\sum_{ab}F(\lambda_{ab},\mu_{ab})$$

$$\times\begin{bmatrix}\sin^2\Theta_{ab}\cos^2\Phi_{ab}-\frac{1}{3}, & \sin^2\Theta_{ab}\sin\Phi_{ab}\cos\Phi_{ab}, & \sin\Theta_{ab}\cos\Theta_{ab}\cos\Phi_{ab},\\ \sin^2\Theta_{ab}\sin\Phi_{ab}\cos\Phi_{ab}, & \sin^2\Theta_{ab}\sin^2\Phi_{ab}-\frac{1}{3}, & \sin\Theta_{ab}\cos\Theta_{ab}\sin\Phi_{ab},\\ \sin\Theta_{ab}\cos\Theta_{ab}\cos\Phi_{ab}, & \sin\Theta_{ab}\cos\Theta_{ab}\sin\Phi_{ab}, & \cos^2\Theta_{ab}-\frac{1}{3}\end{bmatrix}$$

$$=aN\mathbf{1}+\frac{b}{15}\sum_{ab}N_{ab}9\left\{1+\frac{12}{35}\left(\frac{|\mathbf{r}_a-\mathbf{r}_b|}{N_{ab}l}\right)^2+\cdots\right\}$$

$$\times\begin{bmatrix}\left(\frac{x_a-x_b}{N_{ab}l}\right)^2-\frac{1}{3}\left(\frac{|\mathbf{r}_a-\mathbf{r}_b|}{N_{ab}l}\right)^2, & \left(\frac{x_a-x_b}{N_{ab}l}\right)\left(\frac{y_a-y_b}{N_{ab}l}\right), & \left(\frac{x_a-x_b}{N_{ab}l}\right)\left(\frac{z_a-z_b}{N_{ab}l}\right),\\ \left(\frac{y_a-y_b}{N_{ab}l}\right)\left(\frac{x_a-x_b}{N_{ab}l}\right), & \left(\frac{y_a-y_b}{N_{ab}l}\right)^2-\frac{1}{3}\left(\frac{|\mathbf{r}_a-\mathbf{r}_b|}{N_{ab}l}\right)^2, & \left(\frac{y_a-y_b}{N_{ab}l}\right)\left(\frac{z_a-z_b}{N_{ab}l}\right),\\ \left(\frac{z_a-z_b}{N_{ab}l}\right)\left(\frac{x_a-x_b}{N_{ab}l}\right), & \left(\frac{z_a-z_b}{N_{ab}l}\right)\left(\frac{y_a-y_b}{N_{ab}l}\right), & \left(\frac{z_a-z_b}{N_{ab}l}\right)^2-\frac{1}{3}\left(\frac{|\mathbf{r}_a-\mathbf{r}_b|}{N_{ab}l}\right)^2\end{bmatrix} \quad (8)$$

in which we have used the relation derived from Eq. (2)

$$\frac{4\pi}{\lambda_{ab}}=N_{ab}\left\{1-\frac{3}{2}\left(\frac{|\mathbf{r}_a-\mathbf{r}_b|}{N_{ab}l}\right)^2-\frac{9}{40}\left(\frac{|\mathbf{r}_a-\mathbf{r}_b|}{N_{ab}l}\right)^4+\cdots\right\},$$

$$\mu_{ab}^2=9\left(\frac{|\mathbf{r}_a-\mathbf{r}_b|}{N_{ab}l}\right)^2\left\{1+\frac{6}{5}\left(\frac{|\mathbf{r}_a-\mathbf{r}_b|}{N_{ab}l}\right)^2+\cdots\right\}, \quad (9)$$

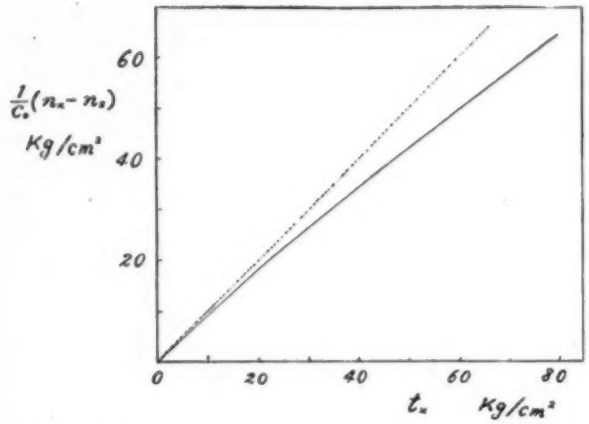

FIG. 2. Optical birefringence *vs* stress in the case of simple elongation. The constant C_0 is

$$C_0=\frac{(\bar{n}^2+2)^2}{\bar{n}}\frac{2\pi b}{45kT}.$$

The dotted corve corresponds to the case of Gaussian-chain-approximation.

and denoted by N the total number of elements of the network per unit volume:

$$N=\sum_{ab} N_{ab}. \tag{10}$$

Equation (8) can be expressed in terms of the extension ratios L_x, L_y, and L_z. When the fixed junctions are displaced in proportion to the extension ratios, the relations between the coordinates of the free junction and the extension ratios assume the form:*

$$x_i=L_x(D_x{}^i+D_{xx}{}^iL_x{}^2+D_{xy}{}^iL_y{}^2+D_{zz}{}^iL_z{}^2). \tag{11}$$

Here, the higher terms of L's come from the non-Gaussian property of chains and are characteristic of their network structure, and D's are the constants of the network:

$$D_x{}^i=-\frac{1}{\Gamma}\sum_\alpha x_\alpha{}^0\sum_j \gamma_{j\alpha}\Gamma_{ji},$$

$$D_{zz}{}^i=-\tfrac{3}{5}\sum_j\sum_{b(\neq j)}\left(\frac{x_j{}^0-x_b{}^0}{N_{jb}l}\right)^2\frac{\Gamma_{ji}}{\Gamma},$$

$$D_{xy}{}^i=-\tfrac{3}{5}\sum_j\sum_{b(\neq j)}\left(\frac{x_j{}^0-x_b{}^0}{N_{jb}l}\right)\left(\frac{y_j{}^0-y_b{}^0}{N_{jb}l}\right)\frac{\Gamma_{ji}}{\Gamma}, \tag{12}$$

$$\Gamma=\det(\gamma_{ab}),$$

$$\gamma_{aa}=\sum_{b(\neq a)}1/(N_{ab}l),$$

$$\gamma_{ab}=\gamma_{ba}=-1/(N_{ab}l),$$

where Γ_{ij} is the cofactor of γ_{ij}, and the suffix zero expresses quantities before deformation. Introducing these quantities into Eq. (8), we can obtain, for example, the following expressions for the elements of the polarizability tensor:

$$P_{zz}=aN+\frac{b}{15}\Big[2A(2L_z{}^2-L_y{}^2-L_z{}^2)+3\Big(J_1+\frac{12}{35}I_1\Big)(2L_z{}^4-L_y{}^4-L_z{}^4)+3\Big(J_2+\frac{12}{35}I_2\Big)(L_z{}^2L_y{}^2-2L_y{}^2L_z{}^2+L_z{}^2L_z{}^2)\Big], \tag{13}$$

$$P_{xy}=0,$$

using the abbreviations

$$A=-\frac{3}{2}\left\{\sum_{i\neq j}N_{ij}\left(\frac{D_x{}^i-D_x{}^j}{N_{ij}l}\right)^2+\sum_{i,\alpha}N_{i\alpha}\left(\frac{D_x{}^i-x_\alpha{}^0}{N_{i\alpha}l}\right)^2+\sum_{\alpha\neq\beta}N_{\alpha\beta}\left(\frac{x_\alpha{}^0-x_\beta{}^0}{N_{\alpha\beta}l}\right)^2\right\},$$

$$J_1=\sum_{i\neq j}N_{ij}2\left(\frac{D_x{}^i-D_x{}^j}{N_{ij}l}\right)\left(\frac{D_{zz}{}^i-D_{zz}{}^j}{N_{ij}l}\right)+\sum_{i,\alpha}N_{i\alpha}2\left(\frac{D_x{}^i-x_\alpha{}^0}{N_{i\alpha}l}\right)\frac{D_{zz}{}^i}{N_{i\alpha}l},$$

$$J_2=\sum_{i\neq j}N_{ij}2\left(\frac{D_x{}^i-D_x{}^j}{N_{ij}l}\right)\left(\frac{D_{xy}{}^i-D_{xy}{}^j}{N_{ij}l}\right)+\sum_{i,\alpha}N_{i\alpha}2\left(\frac{D_x{}^i-x_\alpha{}^0}{N_{i\alpha}l}\right)\frac{D_{xy}{}^i}{N_{i\alpha}l}, \tag{14}$$

$$I_1=\sum_{i\neq j}N_{ij}\left(\frac{D_x{}^i-D_x{}^j}{N_{ij}l}\right)^4+\sum_{i,\alpha}N_{i\alpha}\left(\frac{D_x{}^i-x_\alpha{}^0}{N_{i\alpha}l}\right)^4+\sum_{\alpha\neq\beta}N_{\alpha\beta}\left(\frac{x_\alpha{}^0-x_\beta{}^0}{N_{\alpha\beta}l}\right)^4,$$

$$I_2=\sum_{i\neq j}N_{ij}\left(\frac{D_x{}^i-D_x{}^j}{N_{ij}l}\right)^2\left(\frac{D_y{}^i-D_y{}^j}{N_{ij}l}\right)^2+\sum_{i,\alpha}N_{i\alpha}\left(\frac{D_x{}^i-x_\alpha{}^0}{N_{i\alpha}l}\right)^2\left(\frac{D_y{}^i-y_\alpha{}^0}{N_{i\alpha}l}\right)^2+\sum_{\alpha\neq\beta}N_{\alpha\beta}\left(\frac{x_\alpha{}^0-x_\beta{}^0}{N_{\alpha\beta}l}\right)^2\left(\frac{y_\alpha{}^0-y_\beta{}^0}{N_{\alpha\beta}l}\right)^2.$$

In deriving these equations, we have assumed that the sample is isotropic before stretching.

On the other hand, the calculations of the previous paper show that the stress is expressed by

$$\begin{aligned} t_x &= -\varphi L_x L_y L_z + 2kT\{A + 2BL_x^2 \\ &\qquad + C(L_y^2 + L_z^2)\}L_x^2, \\ t_y &= -\varphi L_x L_y L_z + 2kT\{A + 2BL_y^2 \\ &\qquad + C(L_z^2 + L_x^2)\}L_y^2, \\ t_z &= -\varphi L_x L_y L_z + 2kT\{A + 2BL_z^2 \\ &\qquad + C(L_x^2 + L_y^2)\}L_z^2; \end{aligned} \tag{15}$$

$$\begin{aligned} 2B &= 3\left(J_1 + \frac{3}{10}I_1\right), \\ C &= 3\left(J_2 + \frac{3}{10}I_2\right), \end{aligned} \tag{16}$$

where $-\varphi$ is the internal pressure. Thus, if we approximate the numerical factor 12/35 that appears in the correction terms of Eq. (13) by 3/10, the components of the polarizability tensor are related to the elastic constants A, B, and C in the following way:

$$\begin{aligned} P_{xx} &= aN + \frac{b}{15}[2A(2L_x^2 - L_y^2 - L_z^2) \\ &\qquad + 2B(2L_x^4 - L_y^4 - L_z^4) \\ &\qquad + C\{L_x^2(L_y^2 + L_z^2) - 2L_y^2L_z^2\}], \\ P_{yy} &= aN + \frac{b}{15}[2A(2L_y^2 - L_z^2 - L_x^2) \\ &\qquad + 2B(2L_y^4 - L_z^4 - L_x^4) \\ &\qquad + C\{L_y^2(L_z^2 + L_x^2) - 2L_z^2L_x^2\}], \\ P_{zz} &= aN + \frac{b}{15}[2A(2L_z^2 - L_x^2 - L_y^2) \\ &\qquad + 2B(2L_z^4 - L_x^4 - L_y^4) \\ &\qquad + C\{L_z^2(L_x^2 + L_y^2) - 2L_x^2L_y^2\}], \\ P_{xy} &= P_{yz} = P_{zx} = P_{yx} = P_{xy} = P_{zz} = 0. \end{aligned} \tag{17}$$

RESULTS AND DISCUSSIONS

From the polarizability tensor just obtained, we can readily calculate the birefringence. The result can be written as

$$\begin{aligned} P_{xx} - P_{zz} &= \frac{b}{5}(L_x^2 - L_z^2)\{2A \\ &\qquad + 2B(L_x^2 + L_z^2) + CL_y^2\}, \end{aligned} \tag{18}$$

or combining with the equations of stresses (15),

$$\begin{aligned} P_{xx} - P_{zz} = \frac{b}{5}\Big[&\frac{t_x - t_z}{kT} \\ &- (L_x^2 - L_z^2)\{2B(L_x^2 + L_z^2) + CL_y^2\}\Big]. \end{aligned} \tag{19}$$

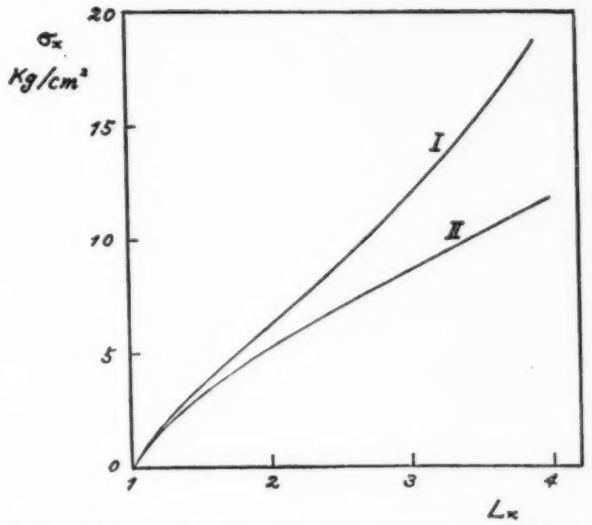

FIG. 3. Theoretical stress-strain curve corresponding to Fig. 2.

The birefringence in the case of simple elongation along the x-axis can be obtained if we merely substitute

$$L_y = L_z = 1/(L_x)^{\frac{1}{2}}; \quad t_z = 0, \tag{20}$$

into Eq. (19). Using the Clausius-Mosotti's formula, we arrive at

$$\begin{aligned} n_x - n_z = \frac{(\bar{n}^2+2)^2}{\bar{n}}\frac{2\pi b}{45kT}\Big[&t_x - \left(L_x^2 - \frac{1}{L_x}\right) \\ &\times\left\{2kTB\left(L_x^2 + \frac{1}{L_x}\right) + kTC\frac{1}{L_x}\right\}\Big], \end{aligned} \tag{21}$$

where $\bar{n}$ is the mean value of the refractive index of the

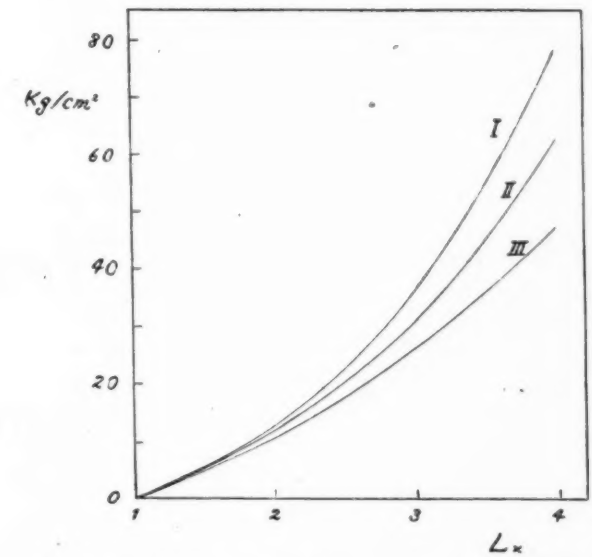

FIG. 4. Birefringence or stress *vs* extension ratio. Curve I: The stress of non-Gaussian network; II: The corresponding birefringence; III: The stress of Gaussian-chains. The birefringence in this case coincides with the curve III.

sample, and the stress t_z is given by

$$t_z=2kT\left[A+2B\left(L_z^2+\frac{1}{L_z}\right)+C\frac{1}{L_z}\right]\left(L_z^2-\frac{1}{L_z}\right). \quad (22)$$

Figure 2 illustrates Eq. (21). The dotted curve corresponds to the Gaussian-chain-approximation. As we can see, the effects of the *network* formation from *non-Gaussian* chains make the straight line bend towards the abscissa. This agrees with the experiments.[2] Figure 3 is the corresponding stress-strain relation. In these diagrams the following values are adopted for the elastic constants:

$$2kTA=3 \quad \text{Kg/cm}^2,$$
$$4kTB=0.04 \text{ Kg/cm}^2,$$
$$2kTC=0.12 \text{ Kg/cm}^2.$$

Tentatively, four times of the values of the previous paper (IV) have been used for the elastic constants B and C for the purpose of representating the non-Gaussian effects clearly.

The curves I and III of Fig. 4 represent the stresses for actual cross section, the former corresponds to non-Gaussian network whereas the latter to Gaussian chains. Curve II illustrates the birefringence in the case of non-Gaussian network as a function of extension ratios; in the case of Gaussian chains the corresponding curve of the birefringence must coincide with the curve III. As we can see, the non-Gaussian-network-effects bend the birefringence curve upward in conformity with the experiments.[2]

Thus, we believe that the effects of the network formation and of non-Gaussian character of chains can be detected by the optical birefringence as well as the elastic measurement. In reality, the effects are somewhat masked by the phenomena of crystallization, but they are diminished, for example, by raising the temperature. Since the theoretical determination of the exact values of the three elastic constants characterizing our formulas is rather difficult, we hope that it can be accomplished by experiment. For this aim, the parallel measurements of the optical and dynamical properties will be powerful, since the factors to B or C of stress (15) and of birefringence (18) are different with each other by the factor 2.

JOURNAL OF APPLIED PHYSICS VOLUME 23, NUMBER 3 MARCH, 1952

Measurement of the DC Resistance of Selenium and Copper Oxide Rectifiers below Room Temperature*

D. M. GRIMES AND SAM LEGVOLD
Institute for Atomic Research and Department of Physics, Iowa State College,† Ames, Iowa
(Received October 3, 1951)

Values of the steady-state dc resistance of copper oxide and selenium rectifiers as a function of temperature from 79°K to 300°K have been obtained. The maximum potentials used were 2.5 volts in the forward direction and 6.0 volts in the backward direction.

It was found that a plot of the logarithm of the resistance against the reciprocal of the temperature was nearly linear for all except the reverse direction of the selenium rectifier. For the latter case at 6.0 volts the resistance went through a minimum below 200°K.

EXPERIMENTAL METHODS

A CONSTANT voltage was placed across a rectifier which was initially at room temperature and which was then cooled slowly to the temperature of liquid nitrogen. The resulting current was measured by placing in series with the rectifier a 25-ohm resistor calibrated against a Leeds & Northrup precision resistor. The voltage drop was measured with a Rubicon type B potentiometer. The applied voltage was obtained from lead storage batteries. The voltage was measured with the same Rubicon type B potentiometer. For voltages greater than 1.5 volts a voltage divider circuit was used.

The temperature was measured with a platinum resistance thermometer. It was calibrated against a Leeds & Northrup platinum thermometer that had been calibrated by the Bureau of Standards. The copper oxide rectifiers used were type H, series 500 of the Conant Laboratories, Lincoln, Nebraska. The selenium rectifiers were type 402D3151 of the Federal Telephone and Radio Corporation, East Newark, New Jersey. Both rectifiers had a rectifying area of about 1 cm². Resistance measurements were made on four copper oxide rectifiers and six selenium rectifiers.

A cryostat that could be immersed in liquid nitrogen was designed and built especially for this purpose. See Fig. 1. The working compartment (A), in which the rectifiers (R_1, R_2, R_3, R_4) and the thermometer (T) were placed, was a cylinder four inches long and two inches in diameter. The cylinder was made of monel

* This paper is from the first author's thesis for the partial fulfillment of the requirements for the degree of Master of Science from the Iowa State College.

† Contribution No. 157 from the Institute for Atomic Research and Department of Physics, Iowa State College, Ames, Iowa. Work was performed in the Ames Laboratory of the AEC.

metal to decrease the heat leak from the compartment to the bath. The space (B) between the compartment and the outer brass sleeve was filled with carbon dioxide and the commerical insulation Santocel. The solidification of the carbon dioxide, when the cryostat was immersed in liquid nitrogen, produced a high vacuum between the cylinders.

Above the experimental chamber there was placed a $\frac{1}{4}$-inch monel tube (F) around which was wound the leads to the rectifiers and the thermometer. A nylon sack (E) was tied around the tube and filled with Santocel to reduce the heat leak. The leads were brought out through Cannon plugs (D) which were soldered into the top of the cryostat. The rubber gasket (G) used as a seal between the flanges was not vacuum tight. The heater consisted of about six feet of wire with a resistance of 27.0 ohms per foot wound noninductively around the outside of the working chamber. The heater leads entered the vacuum jacket through a $\frac{3}{8}$-in. monel tube which was sealed at the top by two Kovar to glass seals (H) manufactured by the Stupakoff Ceramic & Manufacturing Company of Latrobe, Pennsylvania.

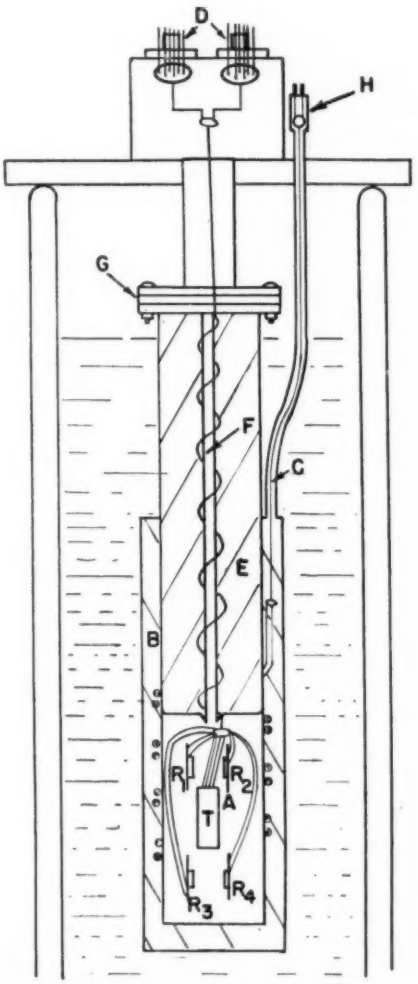

FIG. 1. The immersion cryostat.

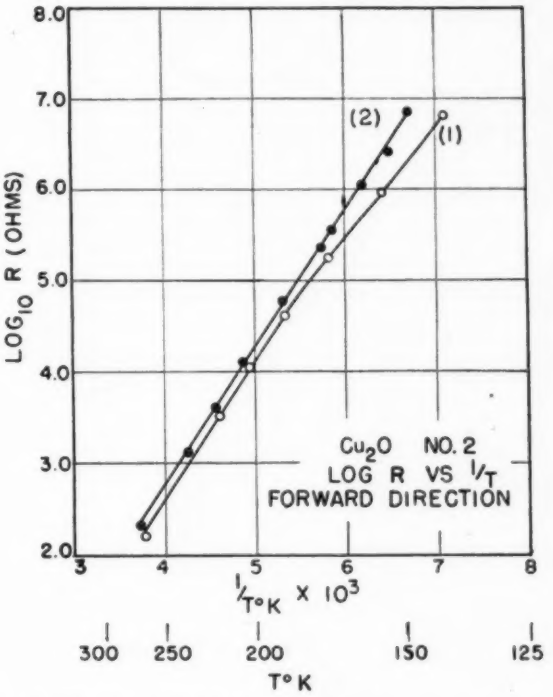

FIG. 2. 2.7 volts applied in the direction of easy current flow on a copper oxide rectifier. (1) cooling curve, (2) heating curve.

The desired temperature was obtained by establishing an equilibrium between the heat coming in from the heater or leaking down the internal leads, and the heat going out either by conduction through the vacuum jacket or along the monel pipe. It was observed experimentally that approximately 45 volts on the heater, an input of about 11 watts, was necessary to maintain a temperature of 273°K in the experimental chamber with the cryostat in a nitrogen bath. With no voltage impressed on the heater an equilibrium temperature of 79°K was obtained.

The rectifiers and the thermometer first were placed in the cryostat and then cooled over a 4 to 8 hour period to the temperature of liquid nitrogen. They were left at this temperature for periods ranging from 0 to 48 hours, then warmed to room temperature within a period of from four to eight hours. Readings were taken on cooling down and on warming up.

In order to obtain consistent results currents were maintained through the samples under test at all times.

RESULTS

For the copper oxide rectifiers the resistance values were nearly reproducible and on a log$R$ *vs* $1/T$ plot they closely approximated a straight line. See Figs. 2 and 3. This is what would be expected from Mott's[1,2] barrier layer theory. The values of voltage used were 2.7 volts in the direction of easy current flow or the forward direc-

[1] N. F. Mott, Proc. Roy. Soc. (London) A **171**, 27 (1939).
[2] H. K. Henisch, *Metal Rectifiers* (Oxford at the Clarendon Press, 1949).

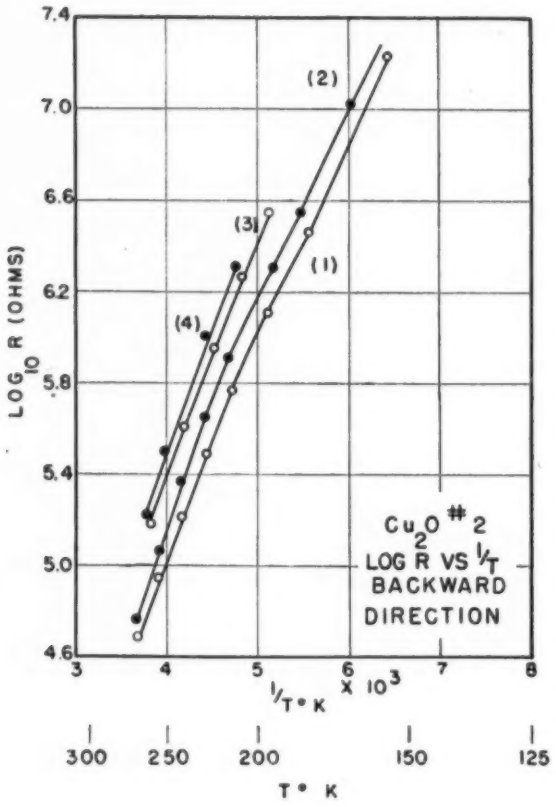

FIG. 3. Voltage applied in the blocking direction. (1) 6.1 volts, cooling curve; (2) 6.1 volts, heating curve; (3) 2.6 volts, cooling curve; (4) 2.6 volts, heating curve.

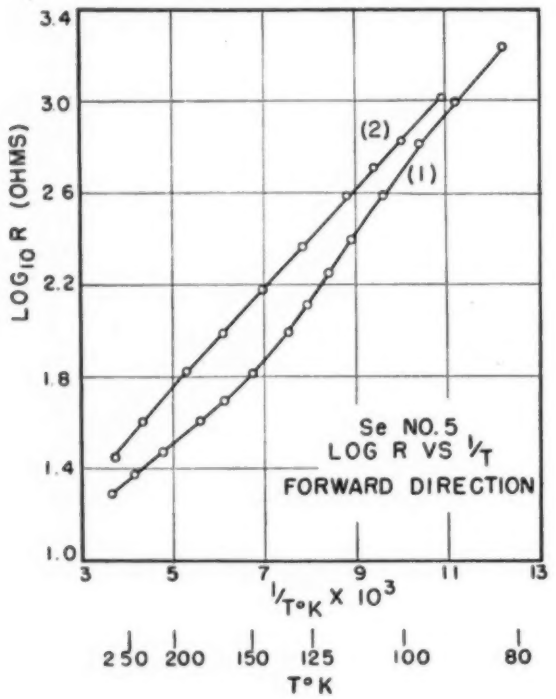

FIG. 4. 2.7 volts applied in the direction of easy current flow on a selenium rectifier: (1) cooling curve; (2) heating curve.

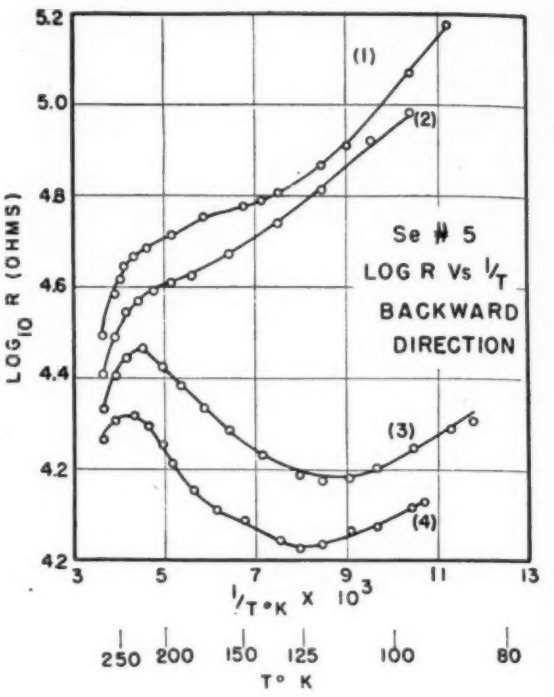

FIG. 5. The blocking direction for a selenium rectifier. The top two curves are the cooling (1) and heating (2) curves for 2.2 volts. The bottom two are cooling (3) and heating (4) curves for 6.1 volts applied.

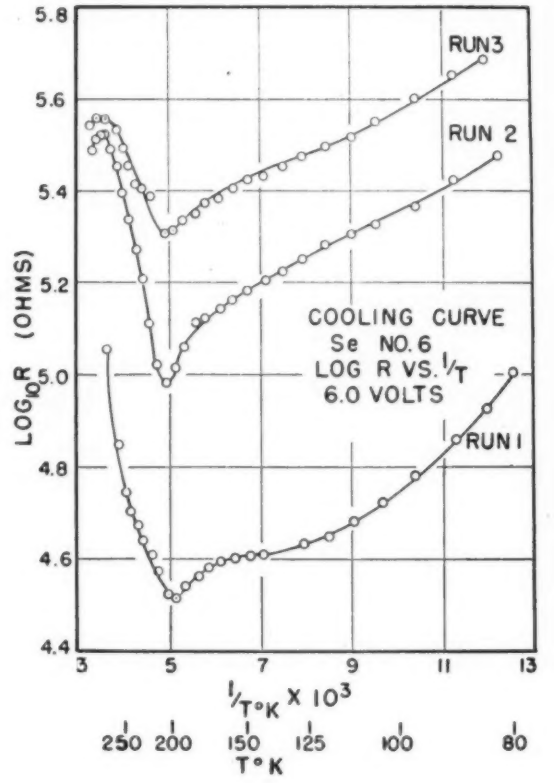

FIG. 6. 6.0 volts applied in the blocking direction for a selenium rectifier. These are cooling curves.

tion and 2.6 and 6.1 volts in the backward or blocking direction.

Upon cooling, the selenium rectifiers gave a nearly linear curve with 2.7 volts applied in the forward direction; on heating the curve was linear. See Fig. 4. In the backward direction at the higher applied voltage the resistance went through a minimum. The value of the resistance at the minimum point decreased with applied voltage. See Fig. 5. The temperature of the minimum varied from rectifier to rectifier through a range of 125°K to 200°K. However, the minimum was reproducible for each particular specimen. Although the shape of the curve remained essentially the same,

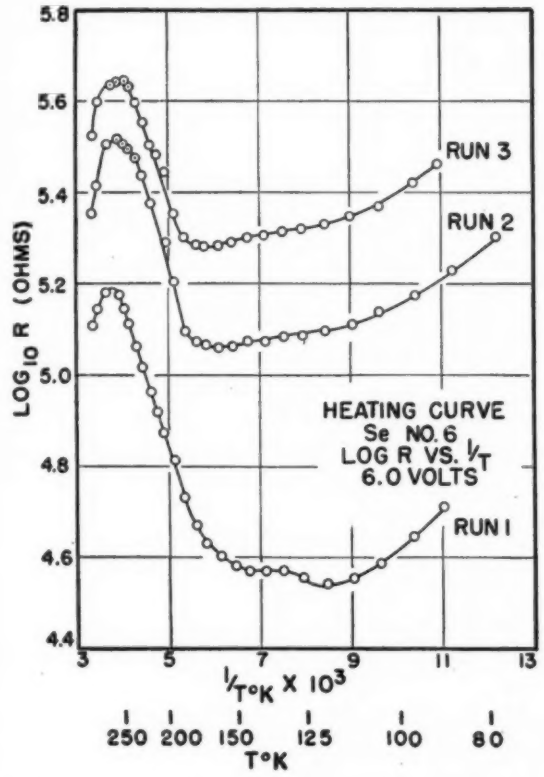

FIG. 7. The heating curves to accompany the cooling curves of Fig. 6.

the resistance at a given temperature increased on successive runs. The form of the cooling and heating curves was not the same for all specimens. See Figs. 6 and 7. A comparison of the size of the effect is given in Fig. 8.

DISCUSSION

In searching for a basis for understanding the resistance minima it was observed that at the temperature

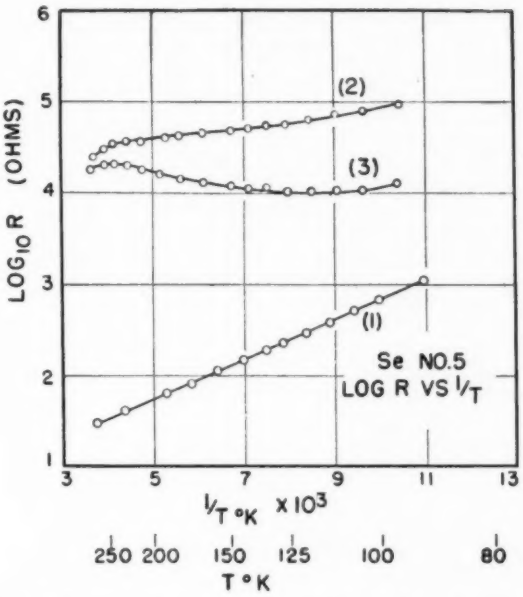

FIG. 8. A comparison of the magnitude of the resistance characteristics of selenium under different circumstances. (1) 2.2 volts applied in the forward direction. (2) 2.2 volts applied in the backward direction. (3) 6.1 volts applied in the backward direction.

at which these minima occur the mean free path of the electrons could be of the same order as the barrier thickness. This suggested that one should change from the diffusion theory to the diode theory[2] at the temperature of the minima. Such a change, however, appears to be in the wrong direction to account for the minima.

About the time this work was completed an abstract of similar work appeared in the March, 1951 issue of *Science Abstracts*. Tomura[3] had measured the resistance of selenium rectifiers with momentary dc pulses as a function of temperature over this same region both before and after the rectifiers had gone through a forming period. In the overlapping regions, the results reported in this paper are in agreement with those reported by Tomura.

CRITICISMS

The rectifiers measured herein were those available commercially and, therefore, no control was exercised over the construction of the rectifiers or over their impurity content.

The heat generated in the rectifiers would cause a higher temperature across the barrier than that actually measured. This effect was thought to be within the limits of reproducibility.

[3] Masao Tomura, J. Phys. Soc. Japan **5**, 349–353 (1950).

Domain Structure of Perminvar Having a Rectangular Hysteresis Loop

H. J. Williams and Matilda Goertz
Bell Telephone Laboratories, Incorporated, Murray Hill, New Jersey

(Received October 1, 1951)

An investigation has been made of the magnetic domain structure of Perminvar (43 percent Ni, 34 percent Fe, 23 percent Co) ring specimens having rectangular hysteresis loops after heat-treatment in a magnetic field. Domain patterns obtained with colloidal magnetite showed curved domain boundaries extending completely around the rings, forming circles concentric with them. Changes in magnetization occur when an applied field causes the circular boundaries either to expand or contract so that there is a change in the relative values of clockwise and counter-clockwise flux. A nucleus of reversed magnetization was formed by making a small notch in a specimen, and this decreased the coercive force and hysteresis loss by a factor of two. It was found that in a 180° domain boundary it was possible to make the change in spin orientations, which occurs in going from one side of the boundary to the other, have either a right- or left-hand screw relation, by the application of a field of appropriate sign perpendicular to the surface. The effect of superposing an applied alternating field was also investigated, and an effective permeability of 4,000,000 was obtained.

INTRODUCTION

PREVIOUS investigations of a Perminvar (45 percent Ni, 30 percent Fe, 25 percent Co) heat treated in a magnetic field showed the material to have a very high maximum permeability[1] and a rectangular loop.[2] A study made in 1942 by G. A. Kelsall and M. Goertz of these laboratories on the effect of composition on the magnetic properties of Perminvars heat treated in a magnetic field showed that a Perminvar having a composition of 43 percent nickel, 34 percent iron, and 23 percent cobalt had the highest maximum permeability, 415,000, after an anneal at 1000°C for one hour followed by cooling from the Curie temperature in a magnetic field of about 15 oersteds. Figure 1 shows the hysteresis loops for the above composition before and after the magnetic anneal as recorded on the Cioffi fluxmeter.[3] The magnetic anneal changes the "wasp-waisted" loop to one having vertical sides, and the maximum permeability is much higher.

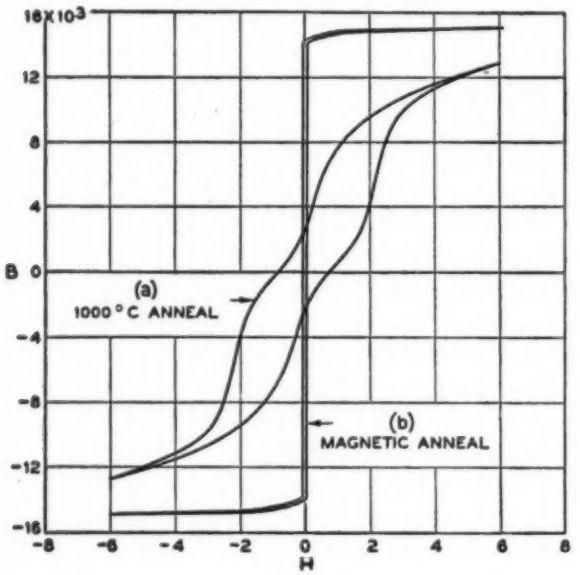

FIG. 1. Comparison of hysteresis loops of a Perminvar ring, (3.8 cm outside diameter, 3.2 cm inside diameter, 0.04 cm thick) after (a) 1000°C anneal, (b) a subsequent magnetic anneal.

The purpose of this work was to investigate the domain structure of polycrystalline Perminvar after heat treatment in a magnetic field, to observe the manner in which this domain structure changes with an applied field, and to correlate these observations with the magnetic properties of this material. Magnetic materials having rectangular hysteresis loops are of practical value for mechanical contact rectifiers and for memory storage devices.[4]

MAGNETIC DOMAIN PATTERNS

It has been known for some time that heat treatment of certain alloys in a magnetic field produces in them a direction of easy magnetization parallel or antiparallel to this field. The alloys that respond to this treatment, such as the iron-nickel alloys containing about 50 to 85 percent nickel, and the iron-cobalt-nickel alloys of the Perminvar type, have low magnetic crystal anisotropy and a Curie point of about 500°C or higher. The assembly of adjacent magnetic domain patterns of Fig. 2 shows a single domain boundary extending part way around a polycrystalline ring and forming two oppositely directed circular flux circuits, as indicated in the accompanying sketch. These patterns show visually the expected direction of easy magnetization and show that this direction follows very closely the direction of the heat-treating field across crystal boundaries and along curved paths, a behavior consistent with the low crystal anisotropy known to exist in the alloy used.

For a smaller ring having an outside diameter of 3 mm certain sections of the ring had three distinct boundaries, two of which could be traced all around the ring. In some instances there were slight irregularities in the

[1] G. A. Kelsall, Physics **5**, 169 (1934).
[2] J. F. Dillinger and R. M. Bozorth, Physics **6**, 279 (1935).
[3] P. P. Cioffi, Rev. Sci. Instr. **21**, 624 (1950).
[4] An Wang, Proc. Inst. Radio Engrs. **34**, 401 (1951).

boundaries, probably due to the polycrystalline structure of the material. These patterns were obtained after electrolytic polishing, which does not make the crystal boundaries clearly visible. However, Fig. 3 shows some of the crystal boundaries and a domain boundary extending across them. A similar type of curved boundary has been observed on a polycrystalline ring of 68 percent nickel and 32 percent iron after heat-treatment in a magnetic field.

The domain boundaries are sometimes difficult to observe, and are not readily traced because of their faintness. To overcome this difficulty somewhat, a normal field was superposed as described in a later section. The domain patterns are obtained, as previously described,[5] by placing a drop of magnetite in colloidal suspension on the surface of the ring and then putting a thin cover glass on the drop; this leaves a thin layer of the liquid between the cover glass and the surface of the ring. The stray magnetic fields at the domain boundaries cause the particles of magnetite to collect along the boundaries so that the outline of the domains can be seen with a microscope.

MECHANISM OF CHANGE OF MAGNETIZATION

In this material the mechanism of change in magnetization is similar to that described by Sixtus,[6] who obtained a single axis of easy magnetization in iron-nickel alloys by the application of tension. After saturation in one direction, when the magnetization begins to reverse, a *nucleus of reverse magnetization* forms at some favorable point in the ring and then grows until it spreads over the entire specimen. A higher field (starting field) is required to form a nucleus than to continue its growth once it has started (critical field). Sixtus used an auxiliary winding to produce a higher field in part of the specimen than in the rest of it. This caused an elongated nucleus to form in this region and the size and shape, which approximated an ellipsoid of revolution, were determined by means of a search coil. The exact mechanism of nucleation, which involves the surface energy of the surrounding boundary and the demagnetizing field of the nucleus, is not known. Dijkstra[7] has proposed a mechanism involving the continuous rotation of a region large enough to overcome the difficulty of the surface energy for very small nuclei, and has calculated a value for the starting field of the right order of magnitude for 78.5 permalloy under tension. He has also pointed out that lattice inhomogeneities such as inclusions can greatly decrease the value of the starting field. Quantitative aspects of the growth of nuclei have been discussed by Döring.[8]

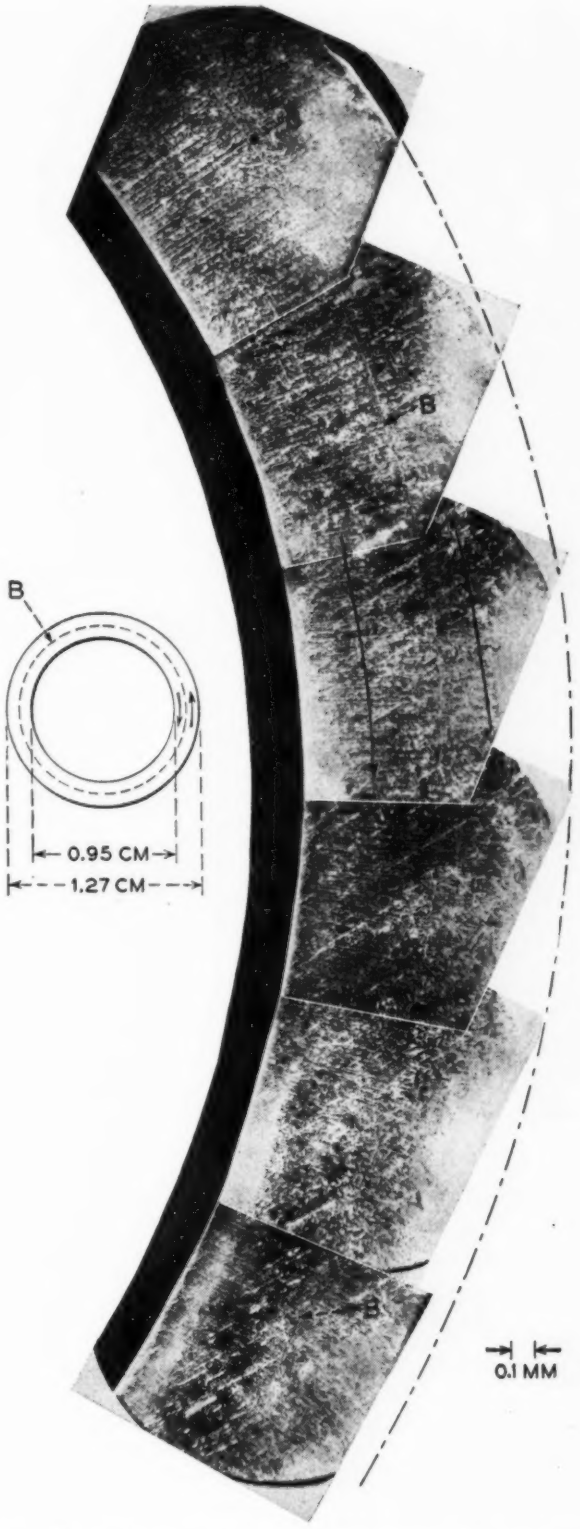

FIG. 2. A series of pictures of adjacent areas showing a circumferential domain boundary (*B*) in a Perminvar ring.

In Fig. 4, at the point *A* the starting field has been reached and the magnetization starts to decrease rapidly; if the field had not been decreased, the curve

[5] Williams, Bozorth, and Shockley, Phys. Rev. **75**, 155 (1949); C. Kittel, Revs. Modern Phys. **21**, 541 (1949).
[6] K. J. Sixtus, Phys. Rev. **48**, 425 (1935); Becker and Döring, *Ferromagnetismus* (1939).
[7] L. J. Dijkstra, *Thermodynamics in Physical Metallurgy* (Am. Soc. Metals, Cleveland, Ohio, 1950).
[8] W. Döring, *Probleme der Technischen Magnetizierungskurve* (Verlag. Julius Springer, Berlin, 1938).

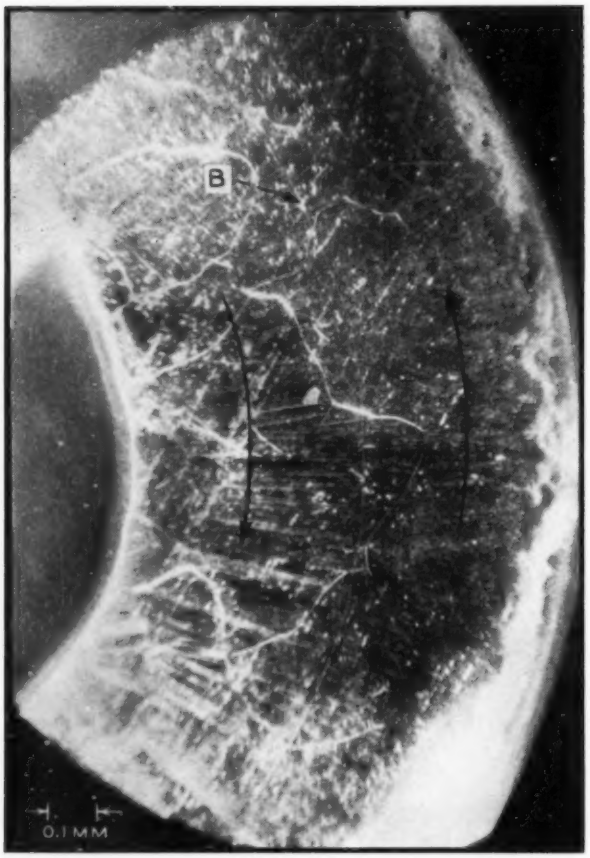

FIG. 3. Photograph showing crystal boundaries and a circumferential domain boundary (B) crossing them.

would have followed the dotted line and a vertical side similar to the one on the right-hand side would have been

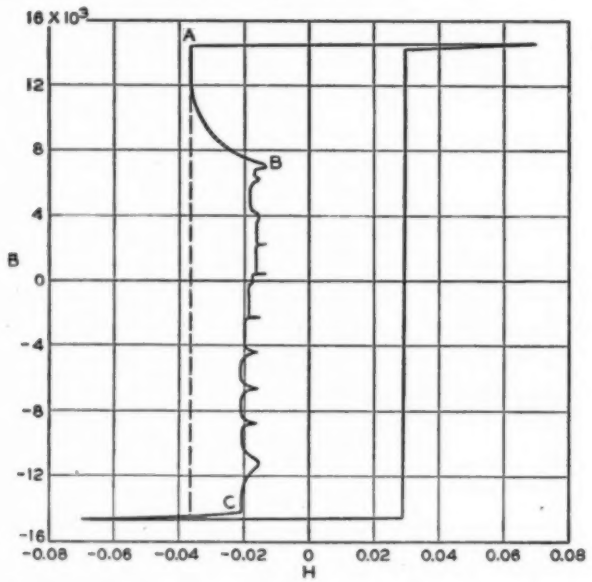

FIG. 4. Hysteresis loop of Perminvar after magnetic anneal. A—Starting field; A–B—rapid decrease of applied field; B–C—traced under equilibrium conditions. Dotted line indicates path described if field had not been reduced to critical field.

traced. However, decreasing the field to a value slightly less than the value of the critical field stopped the change in magnetization. Along most of the section from B to C the loop is being traced under equilibrium conditions. The short horizontal lines show that when the strength of the field is decreased slightly there is no change in magnetization. Similar curves, obtained by sudden decrease of the field strength from the starting field strength, have been reported by Stewart[9] and by Bozorth.[10]

The outer hysteresis loops in Fig. 5 are not traced under equilibrium conditions. The equilibrium hysteresis loop for saturation is difficult to trace on the fluxmeter because the change in magnetization occurs so rapidly when the field reaches the value of the starting field that it is difficult to decrease the field quickly enough. For the inner loops of Fig. 5 the specimen never becomes completely saturated. This means that there are regions

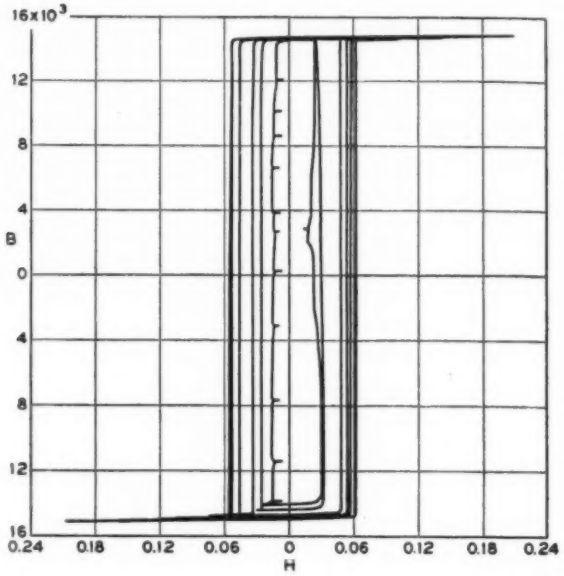

FIG. 5. Family of hysteresis loops. (Inner loops are slightly displaced upward due to drift of fluxmeter.)

or nuclei of reversed magnetization, which require a relatively small starting field, or the regions may extend completely around the ring so that there are circular domain boundaries forming clockwise and counterclockwise flux circuits similar to those obtained in single crystals of silicon iron by Williams and Shockley.[11] Figures 2 and 3 show such circular domain boundaries. When this domain configuration occurs, the changes in magnetization are due to the applied field exerting a pressure on the domain boundaries, causing them to move so that one type of flux circuit grows at the expense of the other. The net flux flowing around the ring

[9] K. H. Stewart, J. phys. et radium **12**, 325 (1951).
[10] R. M. Bozorth, *Ferromagnetism* (D. Van Nostrand Company, Inc., New York, 1951).
[11] H. J. Williams and W. Shockley, Phys. Rev. **75**, 178 (1949).

is, of course, the difference of the clockwise and counter-clockwise flux circuits.

In the case of the previously mentioned crystal of silicon-iron[11] it was found that small secondary domains which form at imperfections in the crystal tend to cling to the moving domain boundary, and, because of their surface tension, pull the boundary back as much as halfway across the crystal when the applied field is reduced to zero. In these Perminvar specimens this is not the case because there is only one axis of easy magnetization, so that the same type of secondary domains are not formed.

The back-pull on a domain boundary by an imperfection in silicon-iron depends on the existence of 90° boundaries, which are inclined 45° to the direction of the applied field. The resulting configuration permits the boundaries originating at an imperfection to be ex-

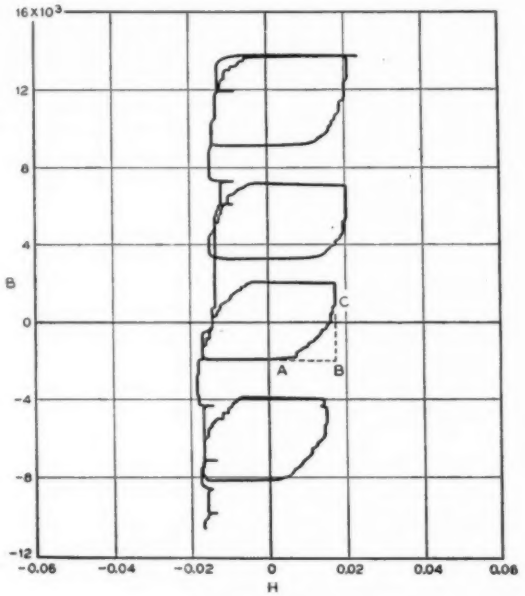

FIG. 6. Minor hysteresis loops.

tended by the change in magnetization, and the extension causes a back-pull on the boundary. In Perminvar heat-treated in a magnetic field, on the contrary, where there is only one axis of easy magnetization, there are only 180° boundaries, which lie nearly parallel to the applied field. As a result there is no long range pull on the movement of the large domain boundaries and release of the applied field causes no change in magnetization. However, the fact that two of the corners of the minor hysteresis loops are not square, as shown at *ABC* in Fig. 6, indicates that here there are small forces tending to move domain boundaries. A smaller value of the field will start to reverse the motion of the boundary than is required to continue its forward motion. These forces do not extend as far as those of the silicon-iron crystal and are probably due to imperfections, or strains, or slight crystal or strain anisotropy, or to lack

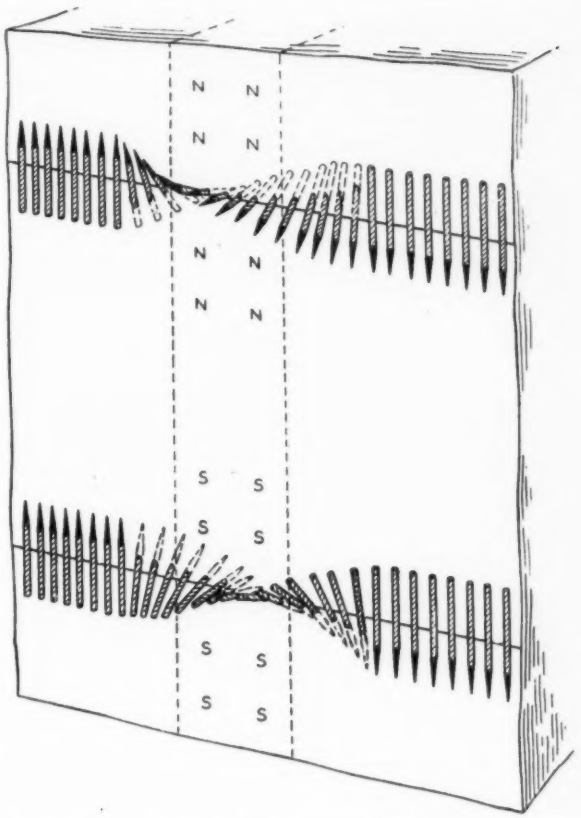

FIG. 7. Schematic of a 180° domain boundary showing spin orientations having right- and left-hand screw relations.

of perfection in the external shape of the specimen. Any of these factors might cause local curvature in the boundaries.

REVERSAL OF SPIN ORIENTATION IN A BOUNDARY

In some instances it was noted that when a vertical field was applied to a ring (field perpendicular to surface) some segments of a domain boundary showed a higher

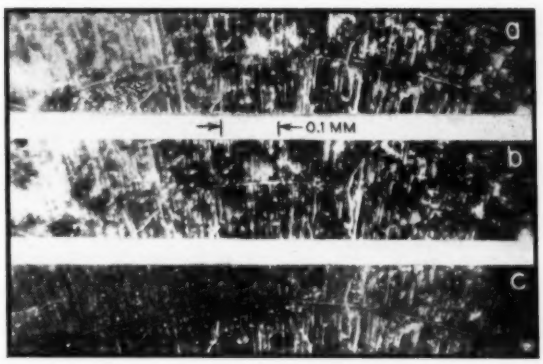

FIG. 8. Domain boundary showing segments with different spin orientations. (a) Small positive vertical field. (Colloid concentrated along segments having a north magnetic pole.) (b) Field reversed (Colloid concentrated along segments having a south magnetic pole.) (c) After applying a high positive field and reducing it to the value used in (a). Now the entire boundary has a north magnetic pole.

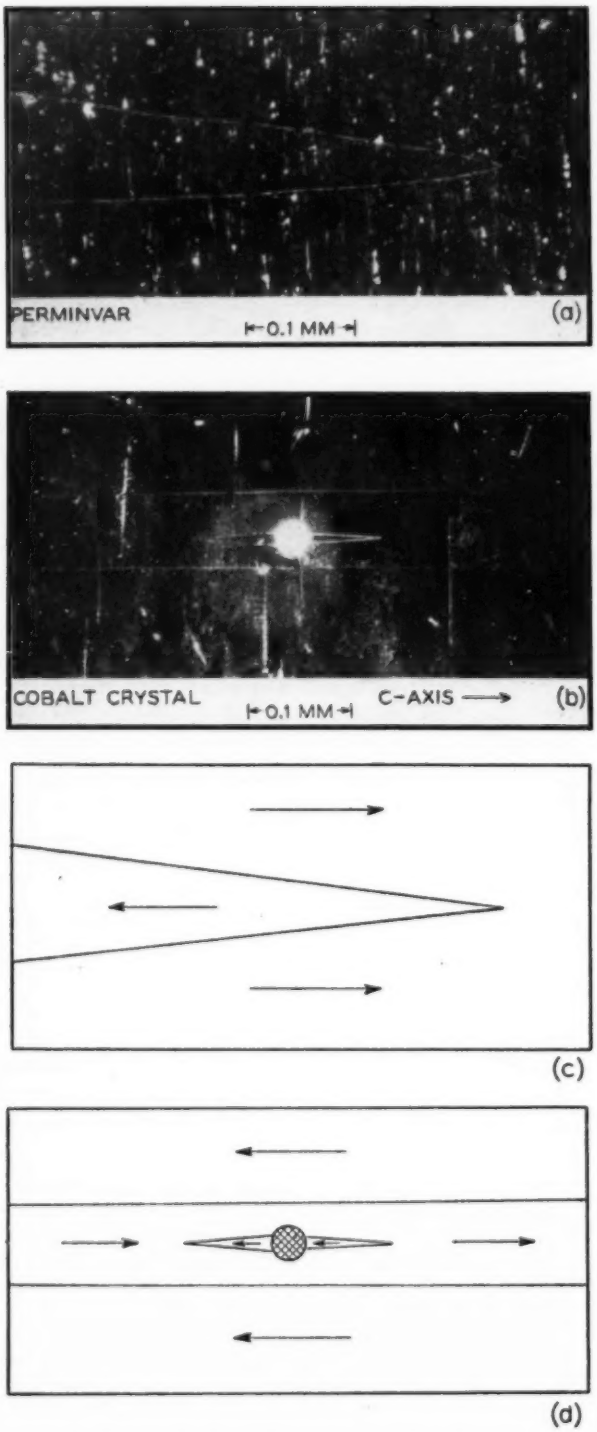

FIG. 9. Nuclei of reversed magnetization. Domain patterns showing region of reversed magnetization in (a) magnetically annealed Perminvar, and (b) a single crystal of cobalt (axis horizontal). Interpretations of (a) and (b) are shown in (c) and (d).

concentration of colloidal particles while others showed a lower concentration than the surrounding region. Reversing the vertical field caused this situation to reverse; the particles disappeared from the segments with high concentration and collected along the segments of low concentration. This indicated that the magnetic polarity of the surface was different on some segments of the boundary than on others. When a positive vertical field is applied, it aids the field due to a north magnetic pole and opposes the field due to a south magnetic pole, and the particles of colloid collect in the regions having the stronger field.[12] By this method the polarity of a boundary can be determined.

In a domain all the electron spins which are the atomic magnets responsible for ferromagnetism have a similar alignment. However, in a boundary which is two or three hundred atomic diameters in width, the successive spins across it gradually change in orientation from parallelism with the spins in one domain to parallelism with those of the adjacent domain. Furthermore, as pointed out by Néel,[13] they change so as to keep the normal component of the magnetization constant across the boundary. This prevents the formation of magnetic poles at a boundary inside the specimen, and leaves only a small strip of magnetic pole where the wall intersects the surface. In the 180° walls of Perminvar the successive spin orientations across the boundary may change with either a right-hand or a left-hand screw relation, since these two modes are energetically equivalent when no vertical field is applied.

Figure 7 is a schematic drawing of a 180° domain boundary, one segment of which shows the right-hand screw relation in spin orientation and the other the left-hand screw relation. In one segment spins point to the surface forming a strip of north magnetic poles, and in the other, a strip of south magnetic poles. In this schematic, a single line of spins has been considered. Actually, the boundary is made up of an array of these forming a succession of sheets of parallel spins. The

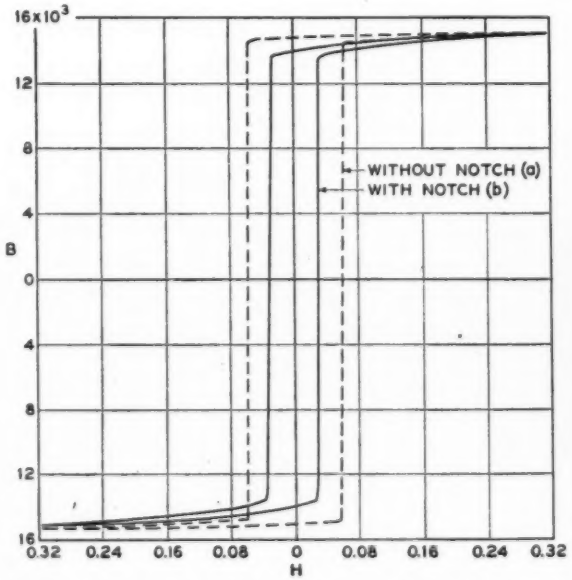

FIG. 10. Hysteresis loops showing effect of a notch in a ring.

[12] C. Kittel, Phys. Rev. **76**, 1527 (1949).
[13] L. Néel, J. phys. [8] **5**, 241 (1944).

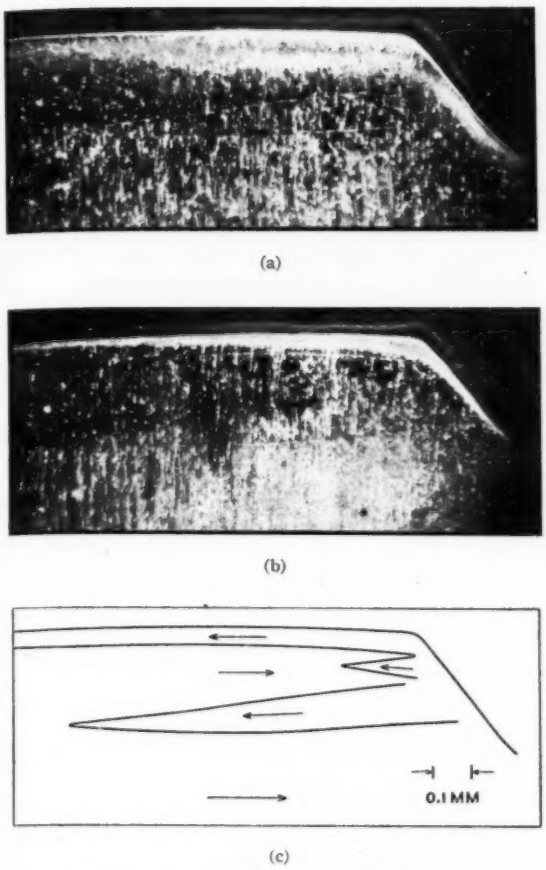

FIG. 11. Domain patterns showing nuclei of reversed magnetization at a notch. (a) Positive vertical field applied. (b) Negative vertical field applied. (c) Interpretation.

central sheets in the boundary are magnetized in either a positive or negative sense, perpendicular to the surface, depending upon whether the spins have a right- or left-hand screw relation.

When a vertical field of sufficient strength is applied it reverses the magnetization in the segments which are magnetized antiparallel to the field. This is shown by the domain patterns in Fig. 8. Here (a) is the pattern obtained with a small positive vertical field, and (b) is the pattern obtained with the field reversed, and (c) is obtained after applying a high positive field and then decreasing the field to its original value. This last pattern shows a continuous concentration of magnetite along the boundary, indicating that the segments which originally were magnetized antiparallel to the field have been reversed. Further experiments showed that it was possible to reverse the spin relation in the entire boundary.

A PROPOSED METHOD OF MEASURING BOUNDARY ENERGY

The surface energy σ of a curved boundary exerts a pressure σ/r, where r is the radius of curvature of the boundary, and this pressure tends to make the circular boundary decrease in size. The field exerts an opposing pressure on the boundary of magnitude $2HI_s$, where I_s is the saturation intensity of magnetization. Equating these two forces we have

$$\sigma/r=2HI_s.$$

When the boundary is ring-shaped the surface tension may be expected to collapse the boundary when σ/r exceeds $2H_0I_s$, H_0 being the critical field strength necessary to move the wall. In Perminvar H_0 is about 0.02 oersted and, assuming σ to be one erg/cm^2, the calculated value of r is about 0.2 mm; a boundary with a smaller radius of curvature may be expected to collapse. By observing boundaries on rings of this size one may be able to determine the radius for which the circular boundaries actually do collapse, and from this determine the surface energy of the boundary σ.

NUCLEI OF REVERSE MAGNETIZATION

Previous work on magnetic domain patterns, especially on a single crystal of cobalt, which also has a single axis of easy magnetization, has shown small secondary domains of reversed magnetization at imperfections (see Fig. 9(b)). These regions form to decrease

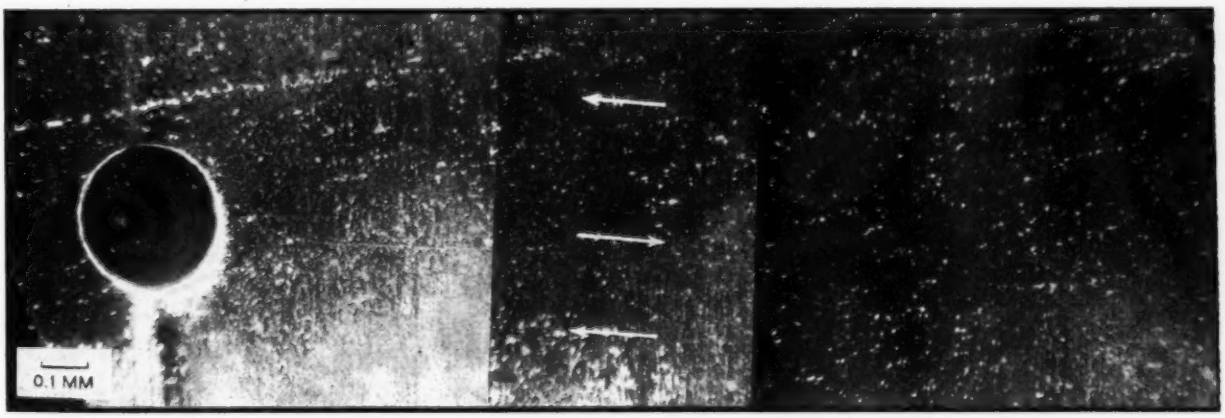

FIG. 12. Domain pattern of a nucleus of reversed magnetization at a 0.2-mm hole in a Perminvar ring. Arrows indicate direction of magnetization.

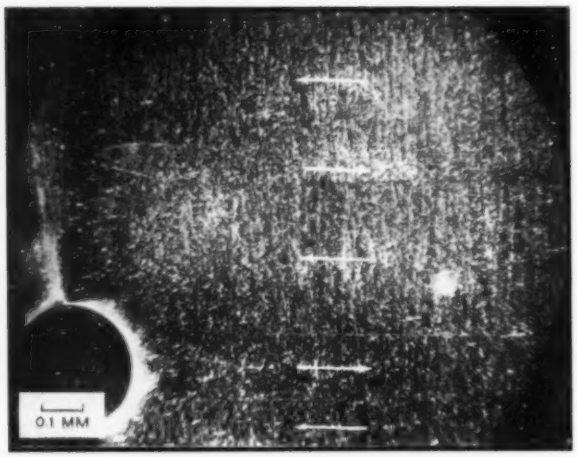

FIG. 13. Domain pattern showing a nucleus of reverse magnetization occurring some distance away from a hole.

the magnetostatic energy at the imperfection, as was first pointed out by Néel.[14] The formation of secondary domains at imperfections suggested the possibility of making an artificial imperfection in a ring to form a favorable region of reversed magnetization, which would grow with a smaller starting field than would be necessary without the imperfection. An imperfection was introduced by filing a notch about 0.1 mm deep on the outer circumference of the ring. Figure 10 (a) and (b) shows hysteresis loops taken before and after making the notch. The coercive force and the hysteresis loss are decreased by a factor of about two.

Figure 11(a) is the photograph of a domain pattern showing nuclei of reverse magnetization formed at a somewhat larger notch than the one previously mentioned. In order to observe the boundaries it was

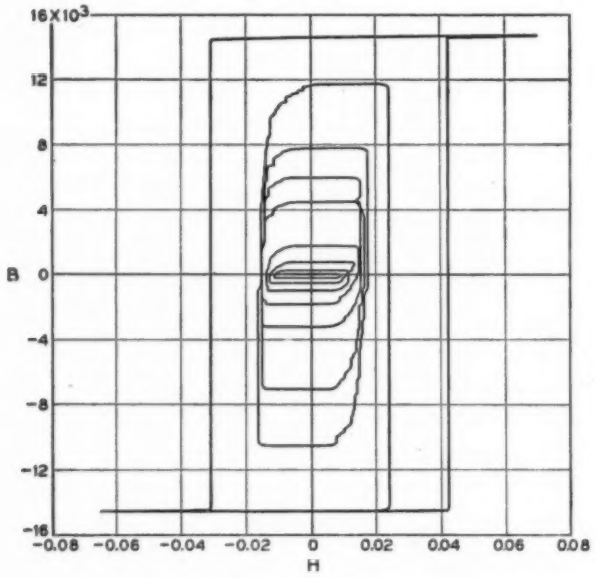

FIG. 14. Demagnetization of a Perminvar specimen.

[14] L. Néel, Cahiers phys. No. 25, 21 (1944).

necessary to apply a field normal to the surface of the ring. This field aids the local fields at boundaries when the two fields are in the same direction, and so causes the colloid to collect and the boundaries to become visible. To observe the boundaries having opposite fields the applied field was reversed. In Fig. 11, (a) and (b) show the effect of reversing the field and (c) is the interpretation of the domain patterns, with the arrows indicating the direction of magnetization. The upper domain on the edge of the ring was observed to taper gradually to a point about one-eighth the way around the ring.

Drilling a hole 0.2 mm in diameter in a ring also introduced nuclei of reverse magnetization in the ring. In this case the specimen was annealed both at 1000°C and in a magnetic field, before and after drilling the hole. The effect on the hysteresis loops was similar to that of making a notch on the side of the ring. Figure 12 shows

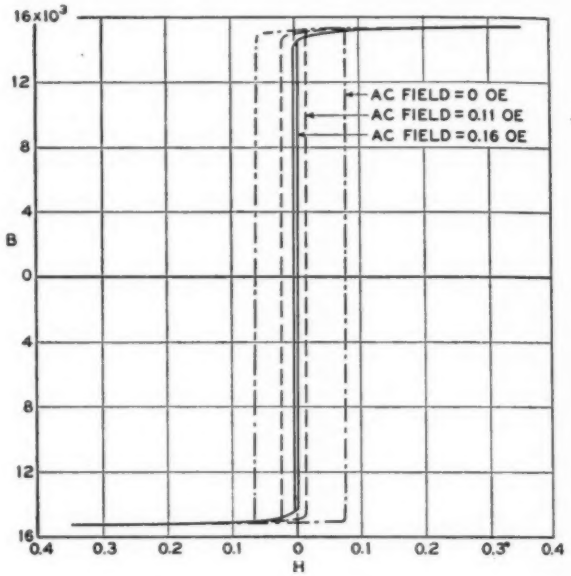

FIG. 15. Hysteresis loops with varying ac superposed fields.

a nucleus of reverse magnetization near such a hole. Observation of the surrounding region showed that other nuclei, such as that shown in Fig. 13, were also formed.

DEMAGNETIZATION

In demagnetizing these specimens it is not sufficient to apply an ac field and gradually decrease the field to zero. This was tried a number of times while the secondary was connected to the Cioffi fluxmeter so that the final flux value could be observed, and in most instances the flux did not reduce to zero. This is due to the rectangular nature of the hysteresis loops. If the field is decreased too much while a horizontal portion of the loop is being traversed, the flux will not change and subsequent cycling merely means that the operating point is shifting back and forth on the horizontal part of

the loop. Or it may happen that while the vertical side of the loop is being traversed the flux suddenly stops changing, and in this case also subsequent cycling with decreasing field produces no change in magnetization, and the operating point shifts back and forth on the horizontal part of a minor hysteresis loop. In terms of the domain picture this means that the domain boundary or boundaries become "stuck" when the clockwise and counter-clockwise flux circuits are not equal, so the net flux is not zero and the decreasing fields fail to shake the boundaries loose.

The specimens can be demagnetized by observing the flux changes and coordinating the field reversals with them as shown in Fig. 14, or the field can be reduced to zero when the flux is observed to be zero while tracing the side of one of the inner hysteresis loops.

Figure 15 shows the effect of superposing an ac field on the specimen while tracing a hysteresis loop. This gives the material an effective permeability of approximately 4,000,000. The effective coercive force is decreased from 0.08 to 0.003 oersted under these conditions.

The authors wish to thank S. O. Morgan, R. M. Bozorth, and J. K. Galt for helpful discussions, and F. J. Dempsey for his cooperation in operating the Cioffi fluxmeter.

JOURNAL OF APPLIED PHYSICS VOLUME 23, NUMBER 3 MARCH, 1952

Study of Imperfections of Crystal Structure in Polycrystalline Materials: Low Carbon Alloy and Silicon Ferrite*

J. J. Slade, Jr., and Sigmund Weissmann
Materials Research Laboratory, College of Engineering, Rutgers University, New Brunswick, New Jersey

(Received October 1, 1951)

The technique of the new x-ray double spectrometer method as described in a former paper[1] is applied to the study of angular misalignment of crystal structure in alloys.

To obtain a better statistical evaluation of the x-ray intensity data the method is extended to include arrays of spots on the Debye-Scherrer lines at high elevations. A complete mathematical discussion of the photometric transformation of the crystallite rocking curves is presented.

The specimens investigated include a low carbon alloy annealed at 850°C and three silicon ferrite samples annealed at 980°, 1100°, and 1200°C.

The quantitative data obtained disclose a significant dependence of crystal perfection on annealing temperature, and demonstrate clearly that the angular misalignment of the coherently reflecting regions within the grains decreases with annealing temperature provided this temperature is not excessive.

Valuable information regarding the influence of cold rolling on the subsequent annealing process is obtained. Thus, the extent of partial recrystallization of the silicon ferrite is deduced from the statistical data, and the differential grain size between the surface layers and the interior of the specimen is revealed through the study of the diffraction effects with radiation of different wavelengths.

A mechanism of grain bending during plastic deformation is suggested and a relationship between magnetic properties, annealing temperature, and crystal perfection of the silicon ferrite is pointed out.

PHOTOMETRIC TRANSFORMATION OF THE CRYSTALLITE ROCKING CURVES

THE angular range of reflection of the coherently reflecting domain in a crystallite was previously obtained[1] through the assumption that both the irradiating beam and the rocking curve of the crystallite have well-defined boundaries. The simple corrections obtained through such an assumption, however, cannot be used except near the equatorial plane, where the intensity distribution of the photographic array of spots is similar to the rocking curve of the crystallite. At higher elevations the distribution of photometric intensities is quite different from the distribution of imperfections that gives rise to it. Since the incidence of reflection is never observed, it becomes necessary to determine the photometric transformation of the measurable parameters of the rocking curve, such as the variance or the width between half-peak intensities—here called the half-width.

Figure 1 represents the unit sphere with center at the specimen S. The vector $\bar{r}$ represents a ray of the pencil that converges to the specimen. With this ray and the Bragg angle θ is associated the Debye-Scherrer cone of which a typical element is the ray $\bar{p}_1$. With the converging pencil is associated a two-parameter family of conjugate cones with vertices at S that intersect the unit sphere in a zone B, which will be called the reflecting zone. A configuration such as this will be associated with each point of the small, but finite, irradiated area. For the purpose of the present investigation, however, all such points may be considered to be concentrated at S, since only the integrated photographic intensities will be required.

The region A represents an area on the surface of the unit sphere pierced by the misaligned normals of a crystallite, one of which is marked $\bar{n}$. When the specimen is rotated about the vertical axis, reflection from

* Supported by the ONR under Contract ONR-454 Task No. 1.
[1] Reis, Slade, and Weissmann, J. Appl. Phys. 22, 665 (1951).

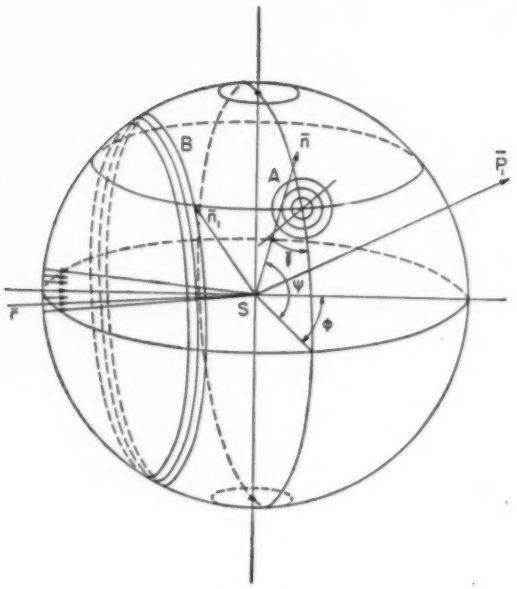

FIG. 1. Reflecting zone and coordinate system.

this facet will occur when $\bar{n}$ coincides with one of the typical vectors $\bar{n}_1$. That is, reflection occurs when the area A intersects the reflecting zone B, and the intensity of the resulting photographic spot will depend, among other things, on the amount of this intersection.

Let $U(\xi)$, $V(\eta)$ be the normalized x-ray intensity distributions in the horizontal and vertical directions of the converging beam. Since the maximum angle subtended by the beam is small, there will be values[2] of (ξ, η) say (a, b) such that $a^2, b^2 \approx 0$ and $U(\xi), V(\eta) \approx 0$, when $|\xi| > a$, $|\eta| > b$.

With every element dA of the area A will be associated a reflecting power $w(A)dA$ in which $w(A)$ is a two-dimensional point function. Let x be the angular measure along a great circle passing through the centroid of the distribution and making the angle γ with the circle of longitude through this centroid. If y is the geodetic measure in the direction perpendicular to the x-circle and

$$W(x) = \int w(A)dy, \tag{1}$$

then $W(x)dx$ is the one-dimensional reflecting power of the strip of width dx shown in Fig. 2, and $W(x)$ is the true rocking curve of the crystallite in the direction of x. In terms of a rotation φ of the specimen, x may be written

$$x = \varphi \cos\psi \sin\gamma, \tag{2}$$

as shown in Fig. 3.

It should be noted that, if φ is the general coordinate shown in Fig. 1, a rotation of the specimen is given by the difference $\varphi_2 - \varphi_1$ of two locations of the normal $\bar{n}$. The origin of φ is immaterial. For general relations on the surface of the sphere φ is taken to be the angle shown in Fig. 1, but when referring to rotations of the specimen, φ is measured as shown in Figs. 3 and 4. In what follows the origin of φ is always specified.

In particular let the origin of φ be the point of intersection of the circle of latitude and the conjugate cone determined by the ray $(1, 0, 0)$, and let φ_1 be the coordinate of the intersection of this circle and the cone determined by the ray $(1, \xi, \eta)$, as shown in Fig. 4. Using Eq. (2) we have

$$W(x)dx = \cos\psi \sin\gamma W[(\varphi - \varphi_1)\cos\psi \sin\gamma]d\varphi. \tag{3}$$

The intensity of the x-rays associated with a point of the reflecting zone is the sum of the intensities associated with the conjugate cones that intersect at this point and is, therefore, $\int_c U(\xi)V(\eta)dc$ where c is the arc of the circle with center at the point and geodetic radius equal to $\pi/2 - \theta$. Since the extremes of (ξ, η) at which the illumination is measurable are extremely small, the maximum angles of intersection of relevant conjugate cones are very small except for θ nearly equal to 90°. Hence, locally the illumination may be considered constant in the direction of the circle determined by the cone $(1, 0, 0)$, the gradient of x-ray intensities being perpendicular to this direction (except, possibly, in cases of extreme back reflection).

Letting γ be the angle the circle $(1, 0, 0)$ makes with the circle of latitude, the total light that reaches the photographic film from the misaligned region at this setting is

$$I(\varphi) = \cos\psi \sin\gamma \times \int\int U(\xi)V(\eta)W[(\varphi - \varphi_1)\cos\psi \sin\gamma]d\xi d\eta, \tag{4}$$

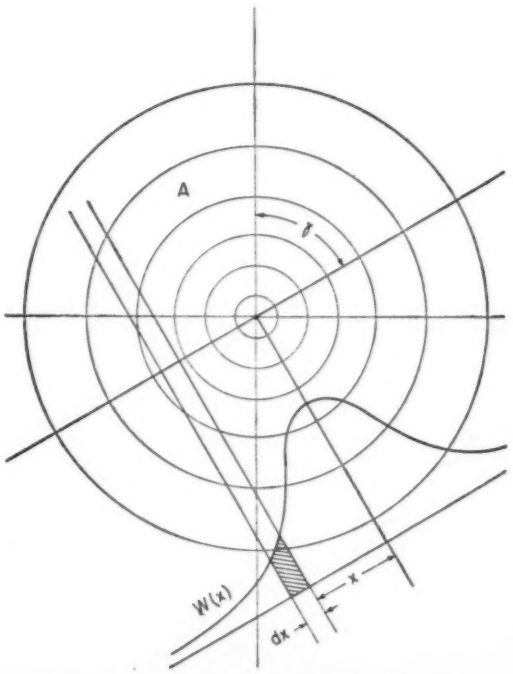

FIG. 2. Distribution of misaligned normals.

[2] The notation used here is the same as that introduced in the former paper (see reference 1).

where the double integration extends over all values of (ξ, η). This is shown schematically in Fig. 4.

We may obtain φ_1 and $\sin\gamma$ in terms of ξ, η, ψ, and θ in the following manner: Let φ be the general longitudinal coordinate of $\bar{n}$ as shown in Fig. 1. The equation of the conjugate cone associated with the ray $(1, 0, 0)$ is

$$\cos\psi\cos\varphi+\sin\theta=0, \tag{5}$$

and that of the cone associated with the ray $(1, \xi, \eta)$ is

$$\cos\psi\cos(\varphi+\varphi_1)+\eta\cos\psi\sin(\varphi+\varphi_1)+\xi\sin\psi+\sin\theta=0. \tag{6}$$

From these two equations and the relations $\xi^2, \eta^2, \varphi^2 \approx 0$ we find

$$\varphi_1=\eta+\frac{\xi\sin\psi}{\sin\varphi\cos\psi}=\eta+\frac{\xi\sin\psi}{(\cos^2\psi-\sin^2\theta)^{\frac{1}{2}}}. \tag{7}$$

Also

$$\tan\gamma=\frac{d\psi}{\cos\psi d\varphi}=-\frac{\tan\varphi}{\sin\psi}\ \text{(from Eq. (5))};$$

$$=\frac{(\cos^2\psi-\sin^2\theta)^{\frac{1}{2}}}{\sin\theta\sin\psi}.$$

Therefore

$$\sin\gamma=\frac{(\cos^2\psi-\sin^2\theta)^{\frac{1}{2}}}{\cos\theta\cos\psi}. \tag{8}$$

Let σ_ξ^2, σ_η^2, σ^2 be the variances of $U(\xi)$, $V(\eta)$, $W(x)$. If Σ^2 is the variance of the photometric intensities, then

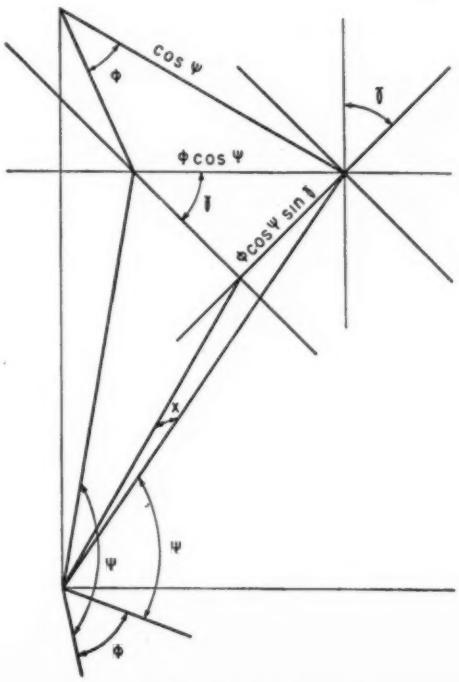

FIG. 3. Great circle measure x.

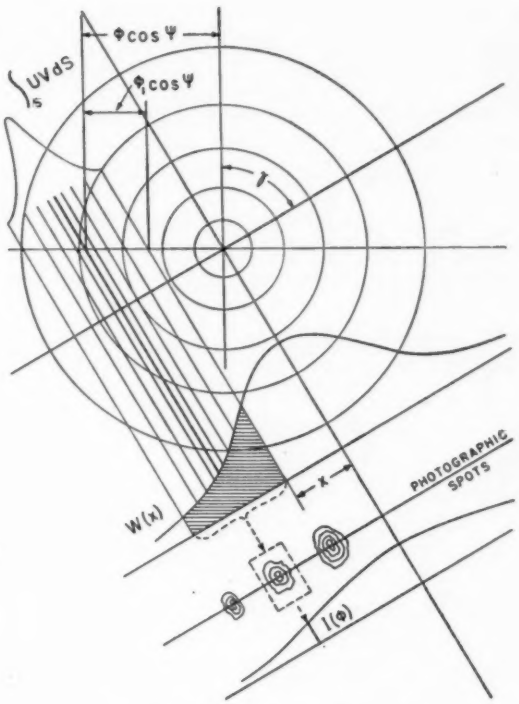

FIG. 4. Photometric transformation.

$$\Sigma^2=\int\varphi^2 I(\varphi)d\varphi=\cos\psi\sin\gamma$$

$$\times\int\int\int\varphi^2 U(\xi)V(\eta)W[(\varphi-\varphi_1)\cos\psi\sin\gamma]d\xi d\eta d\varphi$$

$$=\frac{\sigma^2}{\cos^2\psi\sin^2\gamma}+\sigma_\eta^2+\frac{\sigma_\xi^2\sin^2\psi}{\cos^2\psi-\sin^2\theta}. \tag{9}$$

This relation between the four variances is independent of the analytical forms of U, V, W. Generally, the half-width is a more convenient parameter than the variance, but a relation between half-widths may be obtained from Eq. (9) only when the analytical forms of the distribution functions are given.

A reasonable hypothesis is

$$U(\xi)=1/K, \quad |\xi|<K/2;$$
$$=0, \quad |\xi|>K/2;$$

$$V(\eta)=\frac{1}{(2\pi)^{\frac{1}{2}}\sigma_\eta}\exp[-\eta^2/2\sigma_\eta^2]; \tag{10}$$

$$W(x)=\frac{1}{(2\pi)^{\frac{1}{2}}\sigma}\exp[-x^2/2\sigma^2].$$

For these forms of the distributions it is readily found that

$$\sigma_\xi^2=K^2/12, \quad L=2.36\sigma_\eta^2, \quad H=2.36\sigma^2,$$

where L is the half-width of the horizontal intensities of

the irradiating beam and H is the half-width of the true rocking curve of the crystallite in the x-direction. Substituting these values in Eq. (9) we obtain

$$H=(5.57\Sigma^2-L^2-0.464\Delta\varphi_2^2)^{\frac{1}{2}}\cos\psi\sin\gamma, \quad (11)$$

where

$$\Delta\varphi_2=K\sin\psi/(\cos^2\psi-\sin^2\theta)^{\frac{1}{2}}. \quad (12)$$

Equation (11) may be used only when the array of photographic spots is sufficiently complete to yield a fair estimate of the variance Σ^2. From an incomplete array it may be possible to make an estimate of H', the half-width of the photographic distribution. Equation (4) together with assumptions (10) imply a relation between H' and H, which may be obtained as follows:

The result of substituting Eqs. (10) in Eq. (4) is

$$I(\varphi)=\frac{\cos\psi\sin\gamma}{2\pi\sigma\sigma_\eta K}\int_{-K/2}^{K/2}\int_{-\infty}^{\infty}\times\exp\left[-\frac{(\varphi-\varphi_1)^2\cos^2\psi\sin^2\gamma}{2\sigma^2}-\frac{\eta^2}{2\sigma_\eta^2}\right]d\xi d\eta. \quad (13)$$

The integration with respect to η is readily performed.

TABLE I. Auxiliary table for the calculation of H.

μ	ν	μ	ν	μ	ν	μ	μ
1.01	0.50	1.10	0.76	1.40	1.20	2.50	2.41
1.02	0.54	1.15	0.85	1.50	1.32	3.00	2.91
1.04	0.62	1.20	0.92	1.60	1.43	4.00	3.95
1.06	0.68	1.25	1.00	1.80	1.66	5.00	4.95
1.08	0.72	1.30	1.07	2.00	1.88	6.00	5.96

After some manipulations one obtains:

$$I(\varphi)=\frac{1}{(2\pi)^{\frac{1}{2}}a}\times\int_{-K/2}^{K/2}\exp\left[-\frac{1}{2a^2}\left(\varphi-\frac{\xi\sin\psi}{(\cos^2\psi-\sin^2\theta)^{\frac{1}{2}}}\right)^2\right]d\xi$$

$$=\frac{1}{(2\pi)^{\frac{1}{2}}\Delta\varphi_2}\int_{x_1}^{x_2}\exp[-v^2/2]dv=\frac{1}{\Delta\varphi_2}\{E(x_2)-E(x_1)\}, \quad (14)$$

where

$$\begin{cases} a=(\sigma^2+\sigma_\eta^2\cos^2\psi\sin^2\gamma)^{\frac{1}{2}}/\cos\psi\sin\gamma, \\ E(x)=\dfrac{1}{(2\pi)^{\frac{1}{2}}}\displaystyle\int_0^x\exp[-v^2/2]dv, \\ x_r=(\varphi+(-1)^r\Delta\varphi_2/2)^{\frac{1}{2}}/a, \quad r=1,2. \end{cases} \quad (15)$$

Since $E(x)$ is a tabulated function, we may, by trial, find the value of φ that yields $I(\varphi)=\frac{1}{2}I(0)$ for any value of a and $\Delta\varphi_2$; but since the unknown quantity is a, it is necessary to construct a table.

Let

$$\alpha=\Delta\varphi_2/2a, \quad \beta=(2\varphi+\Delta\varphi_2)/2a.$$

For a set of values assigned to α we have found from Pearson's tables[3] for $z(x)=\frac{1}{2}+E(x)$ the maximum intensity

$$\Delta\varphi_2 I(0)=E(\alpha)-E(-\alpha)=2E(\alpha).$$

Then from these tables we find the corresponding set of numbers β such that

$$\tfrac{1}{2}\Delta\varphi_2 I(0)=E(\alpha)=E(\beta)-E(\beta-2\alpha).$$

For any pair of values (α, β) we have $\Delta\varphi_2/H_1=\alpha/1.18$, $H'/\Delta\varphi_2=\beta/\alpha-1$, where we have let $H'=2\varphi$, since it is the angular displacement between two points at half-peak intensities, and $H_1=2.36a$—the half-width of the distribution of imperfections uncorrected for the effects of the horizontal convergence and the elevation of the array. Now, if we write $\mu=\beta/\alpha-1$, $\nu=1.18/\alpha$, then

$$\mu=H'/\Delta\varphi_2, \; H_1=\nu\Delta\varphi_2,$$
$$H=(H_1^2-L^2)^{\frac{1}{2}}\cos\psi\sin\gamma. \quad (16)$$

Table I gives the values of ν corresponding to selected values of μ. Linear interpolation may be used with two-place accuracy.

When $\mu\approx 1$, Eq. (16) may no longer be used. However, the rate of attenuation of the photographic intensities at half-peak intensity is sensitive to changes in a. Differentiating Eq. (14) we obtain

$$\frac{dI}{d\varphi}=\frac{1}{(2\pi)^{\frac{1}{2}}a\Delta\varphi_2}(\exp[-x_2^2/2]-\exp[-x_1^2/2]).$$

When $\Delta\varphi_2/2a\gg 1$, then, by the first of Eq. (16), $H'=2\varphi=\Delta\varphi_2$ and Eq. (14) becomes, at $\varphi=0$, $I_m=I(0)=1/\Delta\varphi_2$; while, at $\varphi=-\Delta\varphi_2/2$,

$$\frac{dI}{d\varphi}=\frac{1}{(2\pi)^{\frac{1}{2}}a\Delta\varphi_2}$$

whence

$$a=\frac{I_m}{(2\pi)^{\frac{1}{2}}I'(-H_1/2)}$$

or

$$H=.94I_m\Delta\varphi/\Delta I, \quad (17)$$

where ΔI is the decay in photographic intensity at the half-peak when the specimen is rotated through the small angle $\Delta\varphi$, and I_m is the peak intensity. H is then found by the last of Eqs. (16).

The condition $H'=\Delta\varphi_2$ also leads to the equation

$$K=H'(\cos^2\psi-\sin^2\theta)^{\frac{1}{2}}/\sin\psi, \quad (18)$$

a formula that may be used to determine K by using the minimum value of H' observed at high inclinations.

[3] Karl Pearson, *Tables for Statisticians and Biometricians* (Cambridge University Press, London, 1914).

SOME OBSERVATIONS ON THE APPLICATION OF THE THEORY

In order to apply the foregoing theory to a set of data obtained by the new double spectrometer method, it is first necessary to determine the characteristics K, L of the irradiating beam. For a study of all samples described in this paper a cleaved calcite monochromatizing crystal was selected and its reflecting position was kept constant during all exposures. Its half-width, which was the L value of the beam in these experiments, was found from rocking curve studies to be 1.3 minutes.

From a particularly favorable array of spots K was found to be 10.8′ by Eq. (18). This effective value of the vertical convergence was verified by using other favorable arrays. There appears to be no other convenient method of measuring K accurately.

In a number of cases at least two of the Eqs. (11), (16), (17) were used to compute the H of an array, where the array permitted the use of several formulas. The results obtained by the use of the several formulas were always in good agreement.

The assumed forms of U, V, W as given by Eqs. (10) were also verified. $V(\eta)$, being the rocking curve of a monocrystal, is known to be Gaussian. If $W(x)$ is Gaussian, then $I(\varphi)$ (Eq. (14)) for an array of spots on the equatorial plane ($\psi=0$) is Gaussian with variance $\sigma^2+\sigma_\eta^2$. The hypothesis that the observed intensities of arrays at the equatorial plane are samples obtained from normally distributed populations was verified satisfactorily. It is more difficult to verify the form of $U(\xi)$. Eq. (18) merely gives an effective value of the vertical convergence. It is easy to see, however, that a photographic array at high inclination arising from a crystallite of small imperfection would tend to show any marked fluctuations from constancy in $U(\xi)$. The proper arrays in these tests showed only random variations from uniformity, so that within the fluctuations introduced by the measuring technique, the beam used in these experiments could be considered as having a uniform vertical intensity.

Finally, the distributions of half-widths within each Debye-Scherrer line were found to be random with respect to inclination, as they need be if no bias is introduced by the computations involving ψ.

The general formula (9) and the special formula (11) are more reliable than formulas (16), since with the former use is made of the entire statistical series in the determination of σ or H, whereas with the latter, H' is estimated graphically. Though necessarily $\mu>1$, it is possible to observe a sample H' which is smaller than $\Delta\varphi_2$ on account of errors inherent in the photometric process. Because of these errors the individual values of H are determined only within unspecified limits. This indeterminacy is not important when, as in the present study, the average value of H for a Debye-Scherrer line is required. A study of the instrumental variance of the method is being undertaken.

DESCRIPTION OF SPECIMENS

The specimens studied by the new double spectrometer method were obtained from the Research Laboratory of the General Electric Company in Schenectady, New York, through the kind services of Dr. David Harker and Mrs. Buelah Decker. These were all 14 mm strips, $1\times\frac{1}{2}$ in.

The silicon ferrite samples containing 3.2 percent silicon by weight were subjected to a specific work hardening and heat treatment the general outline of which is the following:

(1) The ingot was hot-rolled at 1000°C to 100 mil.

(2) A 100-mil strip was cold-rolled to 29 mil.

(3) The 29-mil strip was annealed for 4–5 minutes, at 925–950°C in neutral atmosphere.

(4) The 29-mil strip was cold-rolled to 14 mil.

(5) The 14-mil strip was annealed for about 5 minutes at 800°C in wet hydrogen atmosphere to produce decarbonization and primary recrystallization.

(6) The silicon samples (a, b, c) were then annealed for 5 hours in pure dry hydrogen at the following temperatures: (a) 980°C, (b) 1100°C, and (c) 1200°C.

A fourth specimen, a commercial low carbon alloy which after cold rolling was annealed at 850°C, was also investigated.

ANALYSIS AND DISCUSSION OF THE RESULTS

The first important fact which was revealed by the study of the annealed silicon ferrite was the different grain size formation in the interior and the surface layers of the specimen. This fact was established by stationary single exposure diagrams using first crystal monochromatized molybdenum and then iron radiations. In the former case an x-ray pattern was obtained of predominantly large, irregular diffraction spots with some fine spots interspersed along the Debye-Scherrer curves; while in the latter case only a fine spot diagram was obtained. The large-spot pattern was characteristic of reflections from large grains, and since only the more penetrating molybdenum radiation disclosed their presence, it follows that these large grains must be located in the interior of the specimens. There can be no doubt that the large spots derived from large grains because, after powdering the specimens and thus breaking up the large grains, the fine-spot diagram obtained with the molybdenum radiation was similar to that obtained with iron radiation.

The nonuniformity of grain size in the annealed silicon ferrite can be explained on the basis of the different degrees of deformation suffered by the various layers of the alloys before the annealing operation. This differential grain size formation is rather surprising, however, in view of the drastic cold reduction to which the samples were subjected. In the case of the low carbon alloy no such phenomenon could be observed. When irradiated with monochromatized molybdenum radiation, the sample gave rise to a fine, uniform spot pattern, as expected.

TABLE II. Statistical characteristics of angular misalignment. 81-M = low carbon alloy annealed at 850°C; 82-M = silicon ferrite (3.2% Si content) annealed at 980°C; 73-M = silicon ferrite (3.2% Si content) annealed at 1100°C; 54-M = silicon ferrite (3.2% Si content) annealed at 1200°C; H = average half-width; τ = standard deviation; ϵ = standard error of mean.

Increasing annealing temperatures	Specimen	X-radiation	(110) H	(110) τ	(110) ϵ	(220) H	(220) τ	(220) ϵ	(200) H	(200) τ	(200) ϵ	(211) H	(211) τ	(211) ϵ
	81-M	Mo	2.17′	0.66	0.33	2.03	0.97	0.93	2.77	1.07	0.32	3.00′	1.19	0.32
	82-M		above 20′	...	...	above 20′	...	...	3′–4′[a]	...	...	above 20′	...	...
	73-M	Fe	5.10	1.61	0.54	5.22	1.52	0.52	2.52	0.67	0.30	3.70′	1.36	0.52
	54-M		7.41	1.99	0.53	7.34	2.39	0.98	5.32	1.46	0.85	7.00′	0.91	0.34

[a] Only one reliable half-width (H = 3.92′) could be obtained, although a number of arrays of low intensities exhibiting half-width values between 3 and 4 minutes could be observed.

The angular misalignment of the coherently reflecting regions in the subgrain structure was then studied by means of the new method. Multiple exposure photographs were taken only of the reflections from the fine grains located in the surface layers, since it was felt that the misalignment of the coarser grains in the interior could be studied by more conventional methods.

Because of the high degree of film absorption to iron radiation the multiple film technique was entirely inadequate for the study of the intensity variations of the diffracted spots, and it was necessary to develop a photometric projection technique based on the Dawton[4] method.

By means of this technique it is possible to print a "positive" film from the original x-ray "negative" under such photographic processing conditions that a change in transparency of the positive film is made directly proportional, over an extended range, to the intensity of the original x-ray beam. The transmitted light enables one to record the integrated value of the diffracted spots photometrically. The exact photographic and photoprocessing conditions will be given in another paper.

For each (h, k, l) reflection the half-widths of the rocking curves of the crystallites were computed by the use of Eqs. (11), (16), or (17). From these values the average half-width $\bar{H}$, the standard deviation τ, and the standard error of the mean ϵ were calculated. The values for the more significant (h, k, l) reflections are shown in Table II.

An examination of the average half-width data of the commercial low carbon alloy shows that the lowest values obtained are those of the (110) and (220) reflections. They are 2.17′ and 2.03′, respectively. The close agreement of the two values is, of course, not surprising since the (220) reflection is the second-order reflection of (110). The fact that the differences of these values is smaller than the standard error of the mean gives confidence in the reliability of the statistical method. These low values may be explained on the basis of the slip mechanism during plastic deformation. If the (110) planes are the active slip planes in a body-centered cubic lattice, then they will be more affected by the cold-rolling operation than any other planes. Since recrystallization starts in the most severely deformed region and since recrystallization usually improves the angular alignment, it is the (110) reflection which should display the smallest angular range of reflection upon annealing. This is indeed borne out by the experimental observations.

If we now examine the average half-width data of the silicon ferrite samples, we observe the opposite phenomenon. It is the (110) and its higher order reflection which exhibit statistically the largest average half-width. Here recrystallization has only been partially effected and some of the old distorted grains have not been entirely replaced by new more perfect grains and still linger on. Their presence increases the average value of the half-width. They are most conspicuous in reflections deriving from those (h, k, l) planes which have experienced the greatest amount of deformation prior to the annealing operation.

In comparing the angular range of reflection of the grains as a function of the annealing temperature it becomes apparent that the average half-width of the silicon ferrite sample decreases with increasing temperature. Thus, for the specimen annealed at 980°C the misalignment is so large that the total angular range of reflections of the individual grains lies beyond the selected experimental range of specimen settings. The average half-width, however, could be estimated to extend well over 20 minutes of an arc for all (h, k, l) reflections excepting the (200) reflection. Annealing the silicon ferrite specimen to 1100°C and keeping the time of annealing constant decreases the angular range of reflection drastically. For the (110) reflection the average half-width has been reduced to 5.10′; and for the (211) and (200) reflections the values are 3.70′ and 2.52′, respectively. As has been pointed out before, recrystallization has not been fully completed even at this elevated temperature. The presence of some old, distorted grains is responsible for the relatively high half-width value in the (110) reflection.

Increasing the temperature to 1200°C results surprisingly in an increase of the angular range of the reflecting domains within the grains and is statistically indicated by an increase in the average half-width

[4] Ralph H. Dawton, Proc. Phys. Soc. (London) **50**, 419 (1938).

values. Parallel with this increase one may observe a marked rise of diffracted spot intensity. These observations suggest the following interpretation:

The elevation of the annealing temperature to 1200°C improves locally the angular alignment so that the density of misalignment in the grain decreases, while the angular displacement at the misfits of the coherently reflecting domains increases. Because of the local improvement of the imperfections larger coherently reflecting volumes between misfits result, and these give rise to stronger x-ray intensities. According to this picture, then, the domains of small angular misalignment in a grain are amalgamated at higher temperatures to larger, more perfect, coherently reflecting domains at the expense of the finer misalignment.

It may be seen from Table II that for the silicon ferrite samples the largest misalignments are found in the (110) reflections while the smallest imperfections are visible in the (200) reflections. The misalignments of the (211) exhibit intermediate values. An interesting explanation has been offered by Dr. David Harker.[5] If the mechanism of bending is accepted as the mechanism of grain distortion, then the (110) set of planes will experience the greatest amount of deformation, since these planes are the active slip planes and bending would therefore take place preferentially along them. The planes perpendicular to the (110) planes should then be least deformed since the *d*-spacing of these planes will hardly be affected by the bending operation. Hence, the (200) set of planes, which contains planes oriented at 45° and 90° to the (110) planes, should show the smallest angular misalignment, while the (211) planes would exhibit intermediate values.

If the deformation by bending were random and not preferential along the (110) planes, then the largest number of excessive misalignments should be observed in the (211) reflections because twelve equivalent planes contribute to this reflection, whereas only six contribute to (110) reflection. The greatest number of excessive misalignments is found, however, in the (110) and not in the (211) reflection. This observation gives considerable support to the theory of preferential bending of the (110) planes.

The study of silicon ferrite has received considerable attention in recent years because of the great application this steel has found in the production of transformer cores. Closely connected with its industrial use is the improvement of its magnetic properties, especially the low hysteresis loss and the high permeability. These properties have been highly developed in the direction of the orientation of the grains, and the efficient transformer cores are so designed that the direction of the flux is always in the direction of the grain. It is believed, however, that the improvement of the magnetic properties does not only depend on improved preferred orientation of the grain but also on the angular misalignment in the subgrain structure. The marked improvement in the hysteresis loss of the silicon ferrite obtained by raising the annealing temperature from 980°C to 1100°C is characteristically reflected in the marked decrease of angular misalignment in the subgrain structure.

The results of the x-ray investigation seem to emphasize the close relationship between crystal perfection and magnetic properties, and the double spectrometer technique promises to reveal the interconnection not only qualitatively but also quantitatively.

ACKNOWLEDGMENT

The authors are indebted to the late Dr. A. J. Reis for initiating this investigation and guiding it through its early stages.

[5] Dr. David Harker, Polytechnique Institute of Brooklyn (private communications).

Lattice Parameters, Coefficients of Thermal Expansion, and Atomic Weights of Purest Silicon and Germanium*

M. E. STRAUMANIS AND E. Z. AKA
The University of Missouri, School of Mines and Metallurgy, Department of Metallurgy, Rolla, Missouri
(Received August 16, 1951)

Lattice parameter determinations of 99.97 percent pure silicon (containing 0.03 percent carbon) were carried out using the asymmetric method, a 64-mm precision camera in a thermostat at constant temperatures (10, 20, 30, 40, and 50°C). The powder mounts, about 0.12-mm in diameter, were translated and rotated during the exposure. Only the (444)-CuKα_1 line was used for the determinations. The lattice parameter $a=5.41991\pm0.00003kX$ (5.43086A) at 20°C, corrected for refraction, was obtained; the linear lattice expansion coefficient (between 10 and 50°C) was 4.15×10^{-6}, the density at 20°C was 2.32831 ± 0.00031 g/cm³ (determined by the suspension method), and the atomic weight was 28.083 ± 0.013 (in agreement with the new chemical weight 28.09) showing that the silicon crystals used, under certain limitations, were sound although the possibility of interstitial atoms is not excluded.

The lattice parameter of purest germanium (99.99 and 99.999 percent) was measured by the same method using the (422)-CrKα_1 and α_2 lines: $a_{20}=5.64607\pm0.00004kX$ (5.65748A) for both materials. The expansion coefficients were $\alpha=6.65\times10^{-6}$ and 5.92×10^{-6}, respectively. The density was 5.3234 ± 0.0025 g/cm³ at 25°C and the calculated atomic weight 72.593 ± 0.037 in agreement with the present chemical weight 72.60. Thus, germanium crystals are sound; however, interstitial atoms are possible.

The precision of lattice parameter determination was about 1:200,000, but in the case of 99.999 percent germanium the precision was considerably better. This shows again that lattice constant determinations can be performed with highest precision and without use of any extrapolation method. The method of lattice parameter determination applied is an absolute one.

INTRODUCTION

SILICON and germanium were selected for the investigation because of the following reasons: (1) although these elements were known for a long time, it is only recently that they were obtained in a very pure form, and, therefore, the lattice parameters, expansion coefficients, and the degree of perfection of silicon and germanium crystals were not exactly known; and (2) the two elements are gaining increasing attention which may be attributed to the variability, diversity, and peculiarity of many of their properties, especially of germanium,[1] which have been studied very little until recent years.

The data available in the literature concerning the lattice parameter of silicon, and especially of germanium, are rather limited and to a certain extent, unreliable, because of the relatively impure materials used (99.8–99.9 percent). The best results attained concerning the constants of both elements (being cubic and of diamond type of structure) are given in Table I.

The expansion coefficient of germanium at room temperature is not even known. Table I shows that the revision of the values of lattice parameters, expansion coefficients, and densities with highest purity materials is, therefore, justified.

I. THE MATERIAL USED

The hyper-pure silicon was received from Dr. C. M. Olson of du Pont Company and used both for x-ray investigations and density determinations. It was prepared by Lyon, Olson, and Lewis,[2] who reduced silicon tetrachloride by zinc vapor at 950°C. The silicon thus obtained consisted of metallic gray crystals which were practically free from metallic impurities (not over 0.001 percent) and had an extremely low electrical conductivity (0.01 ohm^{-1} cm^{-1} at 25°). However, the silicon contained small amounts of carbon (about 0.03 percent). Thus, the element was about 99.97 percent pure.

Two samples of germanium obtained from Mr. E. J. Ritchie of the Eagle-Picher Company (Joplin, Missouri) of the purity 99.99 and better than 99.999 percent were investigated. The spectrographic analysis of the last germanium sample was given in a private communication with Mr. Ritchie, as follows (in percent by weight):

Ca—0.00024	Cu—0.000047
Mg—0.00005	Si—0.00002.

This purity was reported to be in agreement with the electrical properties observed by the producers of the particular slug.

The germanium samples were in the form of small ingots with strong optical reflection of silvery color.

Small quantities of each of the metals were ground in an agate mortar and the x-ray mounts were made from the resulting powder. Since the material was brittle, the grinding was effected so easily that no sieving and annealing of the resulting powder was necessary before the preparation of the powder specimens. The x-ray pictures obtained were sharp enough to attain the highest precision.

II. EXPERIMENTAL PROCEDURE

Determination of Lattice Parameters

The exact values of the lattice parameters of silicon and germanium were determined at ten-degree intervals

* Extract from a thesis submitted by E. Z. Aka in partial fulfillment of the requirements for the Ph.D. degree at the Graduate School of the University of Missouri. The article was presented to the Eighth Annual Pittsburgh Conference on X-ray and Electron Diffraction (November 3, 1950).

[1] W. C. Dunlap, Jr., Gen. Elec. Research Lab. Rept. 1595.

[2] Lyon, Olson, and Lewis, J. Electrochem. Soc. 96, 359 (1949).

between 10 and 50°C, using the following equipment: (1) a precise camera 64 mm in diameter, (2) a jacket into which the camera fitted and in which a constant temperature (±0.02°C) could be maintained by a circulating bath system, and (3) a comparator accurate to 0.001 mm for measuring the films 18 cm in length.[3] Bare films could be inserted into the camera in the asymmetric position; this arrangement permits the computation of the exact Bragg angles without knowledge of the camera radius, without use of a standard substance, and without any corrections for film shrinkage. The powder mounts, 0.12 mm in diameter were thin enough and quite transparent to x-rays so that the absorption correction could be neglected.[3] Sharpest and most uniform lines were obtained when the mounts were almost perfectly centered by means of a sample holder, which was rotated and simultaneously scanned over a range of 3 mm in the inside of the camera.[4] The 6 cm long pinholes (collimators) had a bore of 0.5 or 0.8 mm. The lines were measured from peak to peak intensity. The patterns were indexed by a graphical method.[5]

Copper radiation ($\lambda K\alpha_1 = 1.537395kX$) was selected for production of asymmetric powder patterns of silicon at all temperatures (exposure 1 hour). Only the last $\alpha_1(444)$ line with $\vartheta \cong 80°$ was used for the calculation of lattice constants because the $\alpha_2(444)$ line was superimposed by the $\beta(731)$ line, and hence was too broad to allow accurate measurements.

The germanium powder yielded, with chromium radiation the α_1 and $\alpha_2(422)$ lines under $\vartheta \cong 83°$ ($\lambda K\alpha_1 = 2.28503kX$, $\lambda K\alpha_2 = 2.28891kX$). This doublet was clearly resolved, and the lines were strong and uniform if the samples were rotated and scanned for the twenty minutes of exposure. Both of these last lines were measured and used for the calculation of lattice constants.

Two sets of lines in the front reflection region, namely, $\alpha(111)$ and $\beta(111)$ were also measured on each of the silicon and germanium films for calculation of effective circumferences of the films and the factors of conversion.[3]

Density Determination

The density of silicon was determined by two methods: by the powder method of Baker and Martin[6] based on Archimedes principle, and by the suspension method[7] using single silicon crystals. Both methods were modified in order to make them more convenient for work.

The following distinguishing operations were performed in the density determination of silicon (in g/cm³)

[3] M. E. Straumanis, J. Appl. Phys. **20**, 726 (1949).
[4] M. E. Straumanis and E. Z. Aka, Rev. Sci. Instr. **22**, 843 (1951).
[5] M. E. Straumanis, Am. Mineral. (to be published).
[6] I. Baker and G. Martin, Ind. Eng. Chem. Anal. Ed. **15**, 279 (1943).
[7] H. L. Johnston and C. A. Hutchison, J. Chem. Phys. **8**, 870 (1940). D. A. Hutchison, Phys. Rev. **66**, 144 (1944).

TABLE I. Lattice parameter a and linear expansion coefficient α of Si and Ge.

		a in kX	°C	α in deg $C^{-1} \times 10^6$
v. Arkel[a]	Si	5.418	—	—
Jette, Foote[b]	Si	5.4198±0.00034	25	—
Neuburger[c]	Si	5.4173±0.0005	20	—
Fizeau[d]	Si	—	40	7.63
Erfling[e]	Si	—	20–50	2.42
			0–20	2.16
Goldschmidt[f]	Ge	5.647	—	—
Nitka[g]	Ge	5.648	20	6.0 at 290°

[a] A. E. v. Arkel, Z. Krist. **67**, 235 (1928).
[b] E. R. Jette and F. Foote, J. Chem. Phys. **3**, 605 (1935).
[c] M. C. Neuburger, Z. Krist. **92**, 313 (1935).
[d] H. Fizeau, Compt. rend. **68**, 1125 (1869).
[e] H. D. Erfling, Ann. Physik **41**, 471 (1942).
[f] V. M. Goldschmidt, "Geochemiche Verteilungsgesetze der Elemente VIII," Skrifter Norske Videnskaps-Akad. Oslo. I. Mat.-Natur. Kl., (1927).
[g] H. Nitka, Physik. Z. **38**, 896 (1937).

at a certain temperature by the first method: (1) Purest benzene was added to the powdered silicon, and the powder-liquid mixture was outgassed as well as possible by the application of a suitable vacuum while magnetically stirring the mixture. (2) The first weighing was done while the powdered material, together with its container, was completely immersed in the benzene at a temperature measured. (3) The benzene in the container of the powdered material was evaporated completely after the first weighing. (4) The second weighing of the dry silicon powder was made in air. The first and the second weighings may be repeated by adding a little liquid medium (the same or different) to the dry powder in the container and proceeding as forementioned. The other weighings did not differ from the usual practice. The density was computed by a formula derived from that of Baker and Martin.[6] The precision of the method is $\pm 5 \times 10^{-3}$ g/cm³.

The density of silicon crystals was checked by the suspension method, since the values shown by the powder method are usually lower than they are actually. For this purpose a pycnometer of a special design was used. It was filled (over the mark) with a bromoform-ethanol solution of such composition that the silicon crystal or fragment, which was in the liquid, became suspended in it at a certain temperature. The temperature could be exactly controlled because the pycnometer was placed into a water bath. At the suspension temperature the liquid in excess was removed (down to the mark), and the pycnometer with the liquid and crystal was weighed. Knowing the volume of the pycnometer at the suspension temperature, the density of the liquid, which was equal to the density of the crystal, could be easily computed.

Single, well-developed crystals of silicon with bright, shiny planes were chosen for the determinations. They were 2–5 mm in length, 0.2–0.5 mm in diameter, and their weight was between 0.23–3.85 mg. It was impossible to inspect the crystals as to the presence of cracks or gaps because of the opaqueness of silicon. The crystals were treated with alcohol and some of them with

TABLE II. Variation of lattice parameter of 99.97 percent pure silicon with temperature: $\varphi-(444)\alpha_1$ back reflection angle, Cu-radiation.

Temp. in °C	φ in degrees	Parameter in kX	Parameter av
10.0	10.683	5.41962	
10.0	87	69	5.41966
10.0	86	67	
20.0	10.689	5.41973	
20.0	706	2003	5.41984
20.0	690	1975	
30.0	10.708	5.42007	
30.0	12	14	5.42009
30.0	07	05	
40.0	10.720	5.42028	
40.0	20	28	5.42029
40.0	22	32	
50.0	10.737	5.42059	
50.0	34	53	5.42056
50.0	36	57	

hydrofluoric acid. No heat treatment was applied as the formation of the crystals, according to the manufacturers, occurred at 950°C.[2]

The precision of this density determination method is not as high as the method of D. A. Hutchison ($\sim\pm4\times10^{-6}$ g/cm³)[7] but is at least $\pm3\times10^{-4}$ g/cm³ which is sufficient in order to answer questions concerning the soundness of crystals. Besides, one density determination can be performed in three hours and all operations are simple. The reliability of the method was checked by the determination of density of sublimed sodium chloride crystals.

III. EXPERIMENTAL RESULTS

Lattice Parameters and Expansion Coefficients of Silicon and Germanium

The purpose of Table II is to show (1) the values of the lattice parameters of silicon obtained at different temperatures, (2) the variations in the values at one constant temperature, and (3) the method of attack. At every temperature three photographs were made.

TABLE III. Lattice parameter a of 99.97 percent pure silicon reduced to 20, 18, and 25°C ($\alpha=4.15\times10^{-6}$).

Temp. °C	a_{kX} in kX	a reduced to 20°	
10.0	5.41966	5.41989	
20.0	5.41984	4	
30.0	5.42009	7	
40.0	5.42029	4	
50.0	5.42056	9	
	Average	5.41987kX	
Corrected for refraction[a]		5.41991±0.00003	or 5.43086A
	At 18°C	5.41987	5.43082
	25°	5.42002	5.43097

[a] Correction for refraction: P. P. Ewald in W. Wien and F. Harms, *Handbuch der Experimentalphysik* XXIV/2, 94, 116 (1930).

From these data the average lattice expansion coefficient between 10° and 50° was computed, assuming that in this interval the expansion is linear: $\alpha=4.15\times10^{-6}$. This value lies between the coefficients obtained by Fizeau and Erfling (Table I). By means of $\alpha=4.15\times10^{-6}$ the average parameters of Table II were reduced to standard temperatures of 18, 20, and 25°C.[8] (Table III).

The error given represents the maximum deviation from the average value and the precision of determination is close to 1:200,000.

In Table IV the lattice parameters obtained with 99.99 percent germanium are reported. Since the value of the parameter at 20°C was slightly too high (see Table V), the results were checked using 99.999 percent germanium. The average constants of all these measurements are shown in Table IV.

From these data the expansion coefficients were computed. It was obtained as an average value for 99.99 percent Ge—$\alpha=6.65\times10^{-6}$ and for the purest metal—$\alpha=5.92\times10^{-6}$. In Table V are recorded the lattice parameters of these two kinds of germanium, reduced to the three standard temperatures.

TABLE IV. Lattice parameter a of 99.99 and of 99.999 percent pure germanium at different temperatures. Average values of measurements of 3 and 2 films, respectively. Cr $K\alpha_1$ and α_2 radiation, plane 422. Accuracy of temperature readings: ±0.02°C.

	a in kX of	
Temp. in °C	99.99 percent	99.999 percent Ge
10.0	5.64547	5.645518
20.0	5.64589	—
30.0	5.64618	5.646185
40.0	5.64657	—
50.0	5.64699	5.646856

Table V shows that the precision of determination of 99.99 percent germanium is about the same as in the case of silicon. The precision was lowered because of the results at 20°, which for some unknown reason became too high. An unusually high reproducibility was attained in the case of 99.999 percent germanium which gave sharper lines than the first sample. Further work will show whether it will be possible to reproduce this high precision (better than 1:2,000,000) or not.

Density and Atomic Weight of Silicon and Germanium

The atomic weight A_x of silicon and germanium was calculated using Avogadro's number:[9]

$$A_x=kN_s vd/n. \quad (1)$$

v is the volume of the unit cell (in kX^3), d—the density (g/cm³), n—the number of atoms per unit cell, N_s—

[8] M. Straumanis and A. Ievins, Z. anorg. u. allgem. Chem. 238, 175 (1938).

[9] M. E. Straumanis, Acta Cryst. 2, 82 (1949); Z. Physik 126, 49 (1949).

TABLE V. Lattice parameter a in kX of 99.99 and 99.999 percent pure germanium reduced to 20, 18, and 25°C. ($\alpha = 6.65\times10^{-6}$ and 5.92×10^{-6}, respectively.)

Temp. in °C	a_{Ar}	99.99 percent a red. to 20°C	a_{Ar}	99.999 percent a red. to 20°C
10.0	5.64547	5.64585	5.645518	5.645852
20.0	589	9	—	—
30.0	618	1	5.646185	51
40.0	657	2	—	—
50.0	699	6	5.646856	54
	Av.	5.64585		5.645852
	Ref. corr.	22		216
		5.64607 ±0.00004kX		5.646068 ±0.000002kX
	or	5.65748A		5.657473A
At 18°C		5.64599kX		5.646002kX or 5.657407A
25°		5.64627kX		5.646235 5.657640

Siegbahn's Avogadro number,[10] and k is a constant factor equal to 1.0002.[9,11]

The relative error by which the atomic weights from x-ray and density data is affected, was calculated from the next Eq. (2) which is derived by logarithmic differentiation of Eq. (1), and elimination of v:

$$\Delta A_x/A = 3\Delta a/a + \Delta k/k + \Delta d/d. \qquad (2)$$

N, and n are constants.

In Table VI are reported the densities of silicon determined by the Baker and Martin[6] method. Since the accuracy of determination is only $\pm5\times10^{-3}$ and since there is a tendency to get lower results with the methods using powder, single silicon crystals were used for density determination with the suspension method. The measurements revealed that the crystals have densities which differ appreciably from each other, and the computed atomic weight of silicon showed for most of the determinations a considerably larger value than 28.06, its present atomic weight. Only three crystals out of twelve had lower values. One of these values, some of the middle values, the largest atomic weight, and the average value of 16 determinations (8 crystals) showing an $A_x \geqslant 28.07$, are summarized in Table VI.

The density of germanium was determined by Mr. Ritchie of the Eagle-Picher Company, using the Baker-Martin method.[6] Five samples of purest germanium (three prepared from Tri-State ore and two from African ore) had a density 5.3234±0.0025 g/cm³ at 25.0°C. The atomic weight computed, and the observed and calculated errors (Eq. (2)) are shown in Table VI.

IV. DISCUSSION

Soundness of Silicon and Germanium Crystals

The present value for the lattice constant of 99.97 percent pure silicon is about 2×10^{-4} unit higher than that one determined by Jette and Foote (see reference b in Table I); the agreement is still within the error limits given by them, although the silicon of Jette and Foote was of 99.84 percent purity.

No such comparison can be made in the case of germanium, because the only values for germanium available in the literature (Table I) are not of sufficient precision. The same is true concerning the linear lattice expansion coefficient of this element. (See reference g in Table I.)

The precision attained is about 1:200,000 while in the case of purest germanium it is considerably better. There might be some doubt concerning the high precision attained with a small camera, 64 mm in diameter. However, it was recently proven by Keith[12] that the 64-cm camera works as well as a large 19-cm "Unican" camera.

The data for the density of silicon given in the literature differ considerably[13] because of the difference in purity of the samples. But also in the case of 99.97 percent silicon, there are differences in the densities of single silicon crystals which exceed the error limits of the method of determination (see Table VI). It is believed that these differences are due to two reasons; the presence of carbon (0.03 percent) and of microscopic cracks in the crystals. As silicon carbide that

TABLE VI. Densities and atomic weights of silicon and germanium. p—powder, c—crystal.

		d_t g/cm³	t °C	$d_{25°}$ g/cm³	A_x	A_{chem}[a]	Diff.	$\pm\Delta A_x$
Si+0.03% C	p	2.326	20.0	···	28.055	28.09	−0.035	0.14[b]
Si+0.03% C	c	2.3240	28.58	2.32426	28.034	28.09	−0.056	0.012
Si+0.03% C	c	2.32635	25.34	2.32651	28.0612			
Si+0.03% C	c	2.32539	25.42	2.32649	28.0610	28.09	−0.029	0.0045[c]
Si+0.03% C	c	2.32629	28.33	2.32653	28.0615			
Si+0.03% C	c	2.32764	25.83	2.32781	28.075	···	−0.015	0.012
Si+0.03% C	c	2.32997	28.73	2.33022	28.106	28.09	+0.016	0.012
Av. of 8 Si[d]	c	···	···	2.32831	28.083	28.09	−0.007	0.012
Ge 99.999%	p	5.3234	25.0	···	72.593	72.60	−0.007	0.037

[a] New atomic weight of silicon, see Chem. Eng. News **29**, 4077 (1951).
[b] Assuming that $\Delta a/a = 3\times10^{-5}$, $\Delta k/k = 5\times10^{-3}$ and $\Delta d/d = 5\times10^{-3}$ (Eq. (2)).
[c] Highest precision attained with the same crystal: here $\Delta d/d = 2\times10^{-5}$.
[d] All 8 showing an atomic weight $A_x \geqslant 28.07$.

[10] M. Siegbahn, *Spektroskopie der Röntgenstrahlen* (Verlag. Julius Springer, Berlin, Germany, 1931), 2 Aufl., p. 43.
[11] M. Straumanis, Z. Physik, **126**, 62 (1949).
[12] H. D. Keith, Proc. Phys. Soc. **LXIII**, 1034 (1950).
[13] International Critical Tables, Vol. III, p. 29 (1928).

might have been formed during the preparation has a higher density (3.17 g/cm³) than silicon itself, it might have influenced the density of the resulting product. However, the degree of this influence would also depend on the solubility of the silicon carbide in silicon, of which very little is known.[14]

Usually, the presence of microscopic cracks lowers the density of crystals. Therefore, crystals with fewer cracks will have a larger density, and for the silicon of such crystals a more correct x-ray atomic weight will be obtained. Eight crystals out of twelve had the highest densities observed, which corresponded to the atomic weight of 28.085 for silicon within the limit of ±0.015. Hence, the x-ray atomic weight was calculated only from the densities of these 8 crystals. An average value of 28.083±0.013 was obtained. This value agrees within the error limits (±0.012−0.013) with the new chemical atomic weight of silicon 28.09 recommended by the International Commission of Atomic Weights in September, 1951. Thus, silicon crystals are either sound (the difference −0.007, Table VI, is within the error limits), or they may contain silicon carbide inclusions. The possibility of interstitial atoms in silicon[9] can be discussed only after the investigation of a purer material. But it seems very probable that there are no vacant sites in silicon.

Purest germanium has an x-ray atomic weight which agrees within the error limits (Table VI) with its present chemical atomic weight. But as the densities of a substance determined by its powder are in the most cases slightly too low, the x-ray atomic weight might be higher than the present chemical atomic weight. Thus, germanium crystals are sound, or they contain interstitial atoms. It seems that there is no possibility of vacant sites in germanium.

The objection can be made that the lattice parameters of both elements are too high because no corrections, except that one for refraction, were applied, and besides the Eq. (1) for atomic weight contains a factor $k>1$. However, the introduction of the correction for absorption, which is negligibly small in the high back reflection region, would shift the lattice parameters to higher values, which would emphasize still more the possibility of interstitial atoms in silicon and germanium. The necessity of the factor k (Eq. (1)) has been proven already in an earlier work,[9] and recently it was shown that also in the case of diamond,[15] in order to get the right atomic weight for carbon, this factor is indispensable.

ACKNOWLEDGMENT

The authors wish to express their appreciation to Dr. C. M. Olson, E. I. du Pont de Nemours and Company, Inc., Newport, Delaware for the silicon sample and to Mr. E. J. Ritchie, The Eagle-Picher Company, Joplin, Missouri, for the germanium samples, and for much useful information.

[14] A. E. van Arkel, *Reine Metalle* (Verlag J. Springer, Berlin, Germany, 1939), p. 478; H. von Wartenberg, Z. anorg., u. allgem. Chem. **265**, 186 (1951).

[15] M. E. Straumanis and E. Z. Aka, J. Am. Chem. Soc. **73**, 5643 (1951).

Approximate Elastic Spectrum of β-Brass from X-Ray Scattering*

H. COLE AND B. E. WARREN
Massachusetts Institute of Technology, Cambridge, Massachusetts
(Received November 5, 1951)

The temperature diffuse scattering of x-rays from a single crystal of β-brass has been measured at room temperature using a Geiger counter spectrometer and crystal monochromated CuKα radiation. Measurements were made throughout a large region in reciprocal space, with special attention given to the *hko* plane. The results were in excellent qualitative agreement with the theory developed by Laval and James in which temperature vibrations are expressed in terms of elastic waves. From the measurements, dispersion curves are obtained giving the velocity and frequency of the elastic waves, in the [100], [110], and [111] directions, as a function of their wavelengths. An approximate frequency spectrum is then calculated on the basis of these dispersion curves. The velocities at infinite wavelength are shown to agree with those given by elastic theory using the static elastic constants.

INTRODUCTION

THE displacement of an atom in a crystal lattice due to temperature vibration can be expressed in terms of plane traveling elastic waves. Each traveling wave is denoted by a wave vector $\mathbf{g}$, which is normal to the wave front and of magnitude $1/\lambda$. For a cubic monatomic crystal of N atoms there are N wave vectors, and associated with each wave vector are three independent directions of vibration, which, for certain propagation directions in the crystal, correspond to a longitudinal and two transverse waves. If the N wave vectors are drawn in the reciprocal lattice using as origin any lattice point, then the vectors completely fill the first Brillouin zone with a uniform density of vector tips.

For a crystal in which there is no temperature displacement of the atoms, the diffracted x-ray intensity is sharply confined to the reciprocal lattice points. These points are located by the vectors $h\mathbf{b}_1+k\mathbf{b}_2+l\mathbf{b}_3$ where hkl are the Miller indices and $\mathbf{b}_1\mathbf{b}_2\mathbf{b}_3$ are the reciprocal vectors of the crystal. If the crystal is traversed by an elastic wave of wave vector $\mathbf{g}$, there will be less diffracted intensity at the reciprocal lattice points $h\mathbf{b}_1+k\mathbf{b}_2+l\mathbf{b}_3$ but additional intensity maxima will appear at the positions $h\mathbf{b}_1+k\mathbf{b}_2+l\mathbf{b}_3\pm\mathbf{g}$. The intensity of the diffracted x-rays at these new positions, aside from some geometrical factors, depends upon the mean square amplitude of the elastic wave. In any real crystal a lattice point is surrounded by N, such new maxima giving essentially a continuous diffuse scattering. Measuring the intensity at some position $h\mathbf{b}_1+k\mathbf{b}_2+l\mathbf{b}_3+\mathbf{g}$ in reciprocal space gives the mean square amplitude of the elastic wave with wave vector $\mathbf{g}$.

The mean square amplitude of the wave can be expressed in terms of its frequency and the temperature of the crystal by treating each elastic wave as a harmonic oscillator and assuming the crystal to be in thermal equilibrium at a temperature high enough for equipartition of energy. Hence when we measure the intensity of the temperature diffuse scattering at a position $h\mathbf{b}_1+k\mathbf{b}_2+l\mathbf{b}_3+\mathbf{g}$ in reciprocal space we have picked out a single wave whose direction of propagation and wavelength we know and whose frequency we deduce from the measured intensity.

The preceding discussion is oversimplified in that the intensity measured at a position in reciprocal space may contain contributions from all three modes associated with each wave vector. The weighting of the three modes depends upon the angles between the vibration directions and the vector from the origin of the reciprocal lattice to the point at which the measurement is made. The rigorous theory has been developed by Laval[1] and is presented in a particularly readable form by James.[2]

Following James, the intensity of the diffuse scattering at a position $h\mathbf{b}_1+k\mathbf{b}_2+l\mathbf{b}_3+\mathbf{g}$ in the reciprocal lattice of a cubic monatomic crystal is given by:

$$I_{TD}=NI_e f^2 e^{-2M}\times\frac{kT}{m}\frac{|\mathbf{S}|^2}{|\mathbf{g}|^2}\sum_j\frac{\cos^2(S,e_{gj})}{V_{gj}^2}, \quad (1)$$

where the frequency of the wave has been replaced by the product of the wave vector and the wave velocity, so as to bring out the variation of I_{TD} with position in reciprocal space. The terms have the following meanings:

N is the number of atoms; I_e is the Thomson scattering per electron; f is the atomic scattering factor; e^{-2M} is the Debye temperature factor; k is Boltzmann's constant; T is the absolute temperature; m is the mass of the atom; $|\mathbf{S}|=|h\mathbf{b}_1+k\mathbf{b}_2+l\mathbf{b}_3+\mathbf{g}|=2\sin\theta/\lambda$ is the vector from the origin of the reciprocal lattice to the point of measurement; $\mathbf{g}$ is the wave vector (it is the vector from the nearest nonvanishing reciprocal lattice point to the point of measurement); $\mathbf{e}_{gj}$ is a unit vector in the direction of vibration of the jth mode of the wave with wave vector $\mathbf{g}$ (here $j=1, 2, 3$); V_{gj} is the phase velocity of the gjth mode; $\sum_j$ is the summation over the three independent modes associated with the wave vector $\mathbf{g}$; (S, e) is the angle between $\mathbf{S}$ and $\mathbf{e}$; I_{TD}/NI_e is the intensity in electron units per atom.

* Research sponsored by the ONR under Contract N5ori-07832.

[1] J. Laval, Bull. Soc. Franc. Mineralogie **64** (1941).
[2] R. W. James, *The Optical Principles of the Diffraction of X-Rays* (G. Bell and Sons, London, 1948), Chapter V.

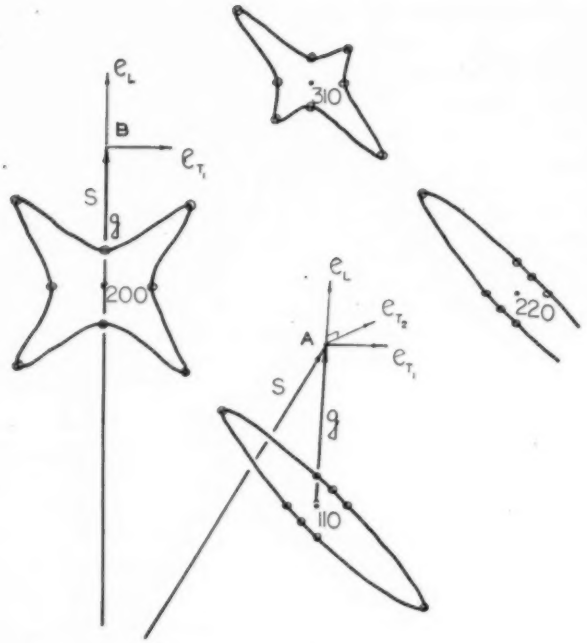

FIG. 1. Approximate equi-intensity contour in the *hko* plane of β-brass computed from the elastic constants. The vectors shown are those appearing in Eq. (1).

For elastic waves propagating in simple directions such as [100], [110], and [111] the three modes become purely longitudinal and transverse and the summation over j may be written:

$$\frac{\cos^2(S, e_l)}{V_l^2}+\frac{\cos^2(S, e_{t1})}{V_{t1}^2}+\frac{\cos^2(S, e_{t2})}{V_{t2}^2}.$$

The velocities, as calculated from the elastic constants, may be used in Eq. (1) to obtain approximate equi-intensity contours in reciprocal space. This method was first pointed out by Jahn.[3] Such contours for β-brass are shown in Fig. 1 in a planar section of reciprocal space containing *hko* points. The velocities used are those tabulated in Table I.

The measured intensity at some point such as point A of Fig. 1 will in general contain contributions from all three modes, the contribution of each mode depending upon the velocity of the mode and the angle between the vector **S** from the origin and the vector $\mathbf{e}_{gj}$ pointing in the direction of vibration of the mode. By choosing special positions in reciprocal space where one of the angles is zero and the other two are 90° it is possible to eliminate the contributions of two modes and thus determine one of the velocities independent of the other two. For example, at point B of Fig. 1 the measured intensity is due to waves propagating in the [100] direction with wavelength $\lambda=1/|\mathbf{g}|$, but since the vibration directions for the two transverse modes are perpendicular to **S**, the intensity is due only to the longitudinal mode. For such a point the intensity expression reduces to:

$$I_{TD}=NI_e f^2 e^{-2M}\frac{kT}{m}\frac{|\mathbf{S}|^2}{|\mathbf{g}|^2}\frac{1}{V_{l100}^2}$$

and an independent determination of V_{l100} is obtained. By measuring the intensity at different points along the line through the 200 and 400 points, we obtain the velocity of the longitudinal mode in the [100] direction for various wavelengths. In a similar way the dispersion curves of other modes may be obtained.

Laval has shown that there will be a slight frequency shift in the x-ray beam due to its interaction with the traveling elastic waves, but this effect is too small to measure. In addition, he derives expressions for the second, third, and higher order terms in the exact intensity expression of which Eq. (1) is just the first order term. Olmer's[4] work on a single crystal of aluminum has beautifully verified Laval's predictions. However, in the work on β-brass the higher order terms were found to be negligible, so the theory as presented in James was sufficient and applicable if β-brass were considered to be an element with $Z=29.5$ and a b.c.c. lattice.

TABLE I. Comparison of the velocities of elastic waves of long wavelength in β-brass at 295°K as obtained by ultrasonic and x-ray methods. (ρ=density.)

Mode	Elastic theory	Lazarus ($\times 10^5$ cm/sec)	X-ray ($\times 10^5$ cm/sec)	%
l_{100}	$\rho v^2=c_{11}$	3.92	3.45	−12
l_{110}	$2\rho v^2=c_{11}+c_{12}+2c_{44}$	4.93	4.5	−14
l_{111}	$3\rho v^2=c_{11}+2c_{12}+4c_{44}$	5.21	4.5	−14
t_{100}	$\rho v^2=c_{44}$	3.15	3.15	0
$t_{110(1)}$	$\rho v^2=c_{44}$	3.15	3.15	0
$t_{110(2)}$	$2\rho v^2=c_{11}-c_{12}$	1.06	1.15	+ 8
t_{111}	$3\rho v^2=c_{11}-c_{12}+c_{44}$	2.01	1.95	− 3

PROCEDURE

Present day counter spectrometer techniques are particularly well adapted for studying the temperature diffuse scattering from single crystals since measurements can be taken throughout specific volumes in reciprocal space. The apparatus was identical to that used by Cowley.[5] X-rays from a full wave rectified copper target tube run at 35 kv and 16 ma were monochromated by a bent quartz crystal set to reflect CuKα. The beam was focused on the face of the crystal. The crystal was mounted in a goniometer so that the best crystal orientation for easy absorption correction could be maintained. A nickel-aluminum balanced filter was used to eliminate the half-wavelength reflected by the quartz crystal.

The crystal used was a single crystal of β-brass approximately 2.0×2.0×0.6 cm cut so that its face was parallel to the (100) planes. It was slightly copper

[3] H. Jahn, Proc. Roy. Soc. **A179**, 320 (1942).

[4] Ph. Olmer, Acta Cryst. **7**, 57 (1948).

[5] J. M. Cowley, J. Appl. Phys. **21**, 24 (1950).

rich, 54.6 percent by weight. After cutting, polishing, annealing, and etching, the face was scanned by means of Laue back reflection photographs. The Laue spots were very sharp over the whole face.

The data were taken at room temperature since this was sufficiently high to insure equipartition in the case of β-brass. The volume element averaged over in reciprocal space at each reading was that defined by a three-degree horizontal divergence of the primary beam and a counter slit height and width subtending angles of three-fourths of a degree at the crystal. Even with this small volume element, the number of counts recorded in those regions of least intensity was roughly twice the background. A two-minute counting interval was used, and the counts were converted to absolute intensity units by comparing with the intensity of scattering at high angle from a thick block of paraffin. The Compton modified component was then subtracted,

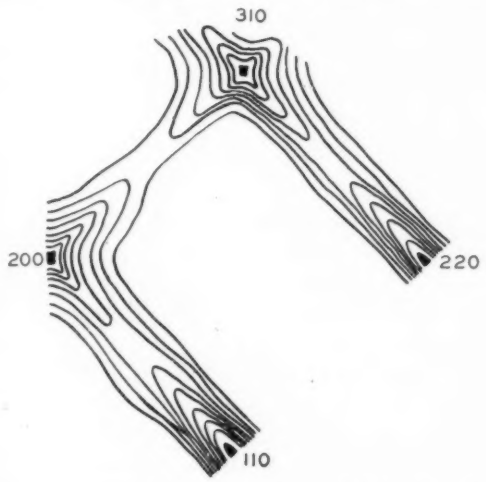

FIG. 2. Contour plot of the measured intensity of diffuse scattering (temperature diffuse plus Compton modified), in the *hko* plane of β-brass at 295°K. Each contour line represents a doubling of the total diffuse intensity.

and the remainder treated as temperature diffuse scattering. Air scattering was unimportant.

RESULTS

(a) Contours

Figure 2 is a contour plot of actual counter readings in the *hko* plane. Since the Compton modified component varies slowly, the general shape of the contours is due to temperature diffuse scattering. Comparison with Fig. 1 shows that it agrees remarkably well with the predicted contours. Each contour line represents approximately a doubling of the counts on the lower contour. In the regions between the bridges the temperature diffuse scattering is roughly half of the total scattering. Enough readings were taken in the region about the 200 point to construct a three-dimensional equi-intensity contour. Figure 3 shows this contour enclosed in the first Brillouin zone. From Figs. 2 and 3

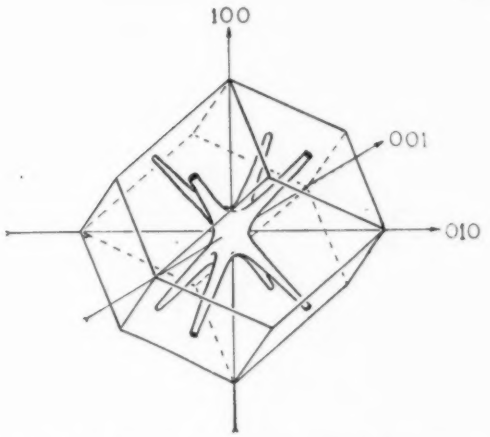

FIG. 3. An equi-intensity contour for the 200 point, enclosed in the first Brillouin zone, from measurements of diffuse scattering in β-brass.

it is evident that the temperature diffuse scattering in β-brass is sharply concentrated to bridges running in [110] directions between the reciprocal lattice points, with large intermediate regions of small intensity.

(b) Dispersion Plots

Figures 4 through 9 are plots of the phase velocity and frequency *versus* $1/\lambda$ for each of the three modes in the [100], [110], and [111] directions as calculated from Eq. (1) using smoothed intensity data taken along the paths indicated on the plots. The open circles and triangles represent measurements in different regions of reciprocal space.

The limiting velocities as $1/\lambda$ goes to zero should agree with those obtained by elastic constant measurements. A comparison between the x-ray values and those obtained by Lazarus[6] is shown in Table I. The discrepancies may be consistently explained in terms

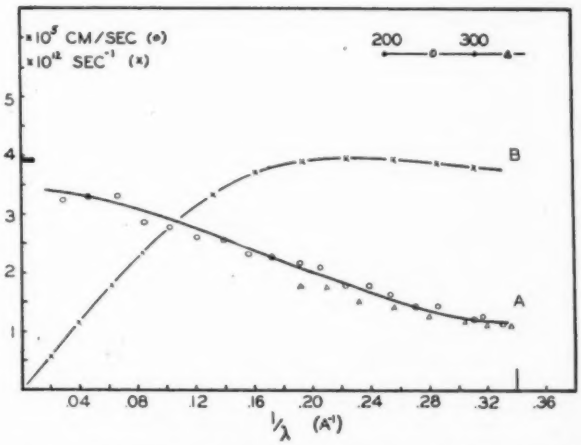

FIG. 4. Dispersion of the longitudinal mode in the [100] direction in β-brass at 295°K. Curve *A* is a plot of velocity ($\times 10^{-5}$ cm/sec) *vs* wave vector length (A^{-1}). Curve *B* is frequency ($\times 10^{-12}$ sec^{-1}) *vs* wave vector length (A^{-1}). The velocity intercept shown is that predicted by elastic theory.

[6] D. Lazarus, Phys. Rev. **74**, 1726 (1948).

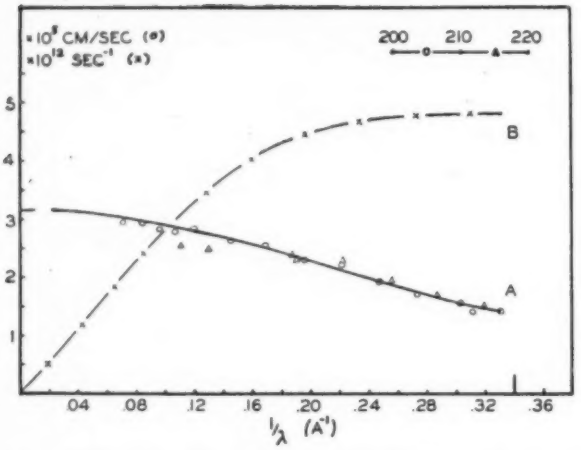

FIG. 5. Dispersion of the transverse mode in the [100] direction in β-brass at 295°K. Curve A is a plot of velocity ($\times 10^{-5}$ cm/sec) *vs* wave vector length (A^{-1}). Curve B is frequency ($\times 10^{-12}$ sec^{-1}) *vs* wave vector length (A^{-1}). The velocity intercept shown is that predicted by elastic theory.

of the intensity distribution in reciprocal space and the size and shape of the volume element averaged over. Some data taken at 400°C indicate smaller limiting velocities and thus a lowering of the elastic constants with temperature.

(c) Frequency Spectrum

The number of waves propagating within a solid angle $d\Omega$ and having frequencies lying between ν and $\nu+d\nu$ is[7]

$$dn=\rho\nu^2 d\nu d\Omega/V^2U,$$

where V is the phase velocity and U is the group velocity, $d\nu/d(g)$, or the slope of the ν *versus* $1/\lambda$ curve (Figs. 4 through 9), and ρ is the density of wave vector

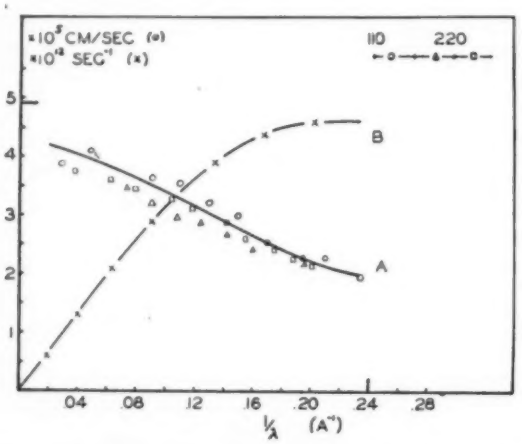

FIG. 6. Dispersion of the longitudinal mode in the [110] direction in β-brass at 295°K. Curve A is a plot of velocity ($\times 10^{-5}$ cm/sec) *vs* wave vector length (A^{-1}). Curve B is frequency ($\times 10^{-12}$ sec^{-1}) *vs* wave vector length (A^{-1}). The velocity intercept shown is that predicted by elastic theory.

[7] L. Brillouin, *Wave Propagation in Periodic Structures* (McGraw-Hill Book Company, Inc., New York, 1946), p. 151.

tips in the first Brillouin zone. Since for each wave there are three modes, the final expression becomes

$$dn=\rho\nu^2\left[\frac{1}{V_l^2U_l}+\frac{1}{V_{t_1}^2U_{t_1}}+\frac{1}{V_{t_2}^2U_{t_2}}\right]d\nu d\Omega.$$

Following Debye, if all the modes have the same velocity, V_0, then we get the well-known parabolic frequency distribution:

$$dn/d\nu=(4\pi\rho 3/V_0^3)\nu^2.$$

However, with dispersion present, it is necessary to know how V and U vary with ν and Ω to get the correct spectrum. Since we know how V and U vary with ν in only twenty-six directions, we need some method of interpolation. One procedure, proposed by Houston,[8] is to make use of Kubic Harmonics; however a simpler

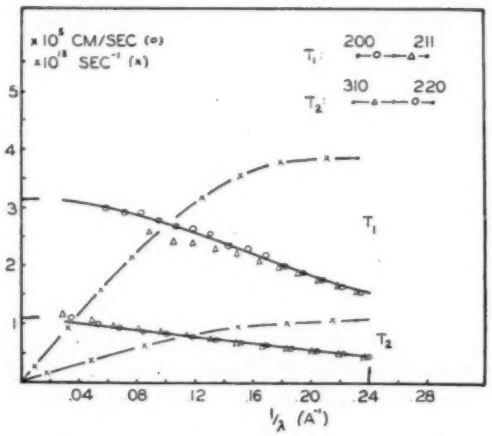

FIG. 7. Dispersion of the transverse modes in the [110] direction in β-brass at 295°K. The upper set of curves gives velocity ($\times 10^{-5}$ cm/sec) and frequency ($\times 10^{-12}$ sec^{-1}) of the $t_{110(1)}$ mode *vs* wave vector length in A^{-1}. The lower curves give the corresponding information for the $t_{110(2)}$ mode. The intercepts are those predicted by elastic theory.

but cruder approach was used, namely: $dn/d\nu$ as a function of ν was calculated for the waves traveling in the [100], [110], and [111] direction using the measured values of V and U, and then $6/26(4\pi)$ of the [100], $12/26(4\pi)$ of the [110], and $8/26(4\pi)$ of the [111] were taken and added to get the final distribution. Essentially this assumes that all the elastic waves in cones of total solid angle $6/26(4\pi)$, where the 4π is the total solid angle over a sphere, about the [100] directions, have the same dispersion curves as do the [100] modes. Houston's method would merely have changed the relative values of the fractions taken. Figure 10 is the resultant frequency distribution obtained in this manner.

The very sharp peaks in the spectrum occur at frequencies for which U is zero for some mode. U is zero at those frequencies for which the ν *versus* $1/\lambda$ curves have zero slope. These curves always have zero slope

[8] W. V. Houston, Revs. Modern Phys. **20**, 161 (1948).

at $g_{max}(1/\lambda_{min})$ and may be zero at other frequencies, as, for example, in the longitudinal [111] mode. This is consistent with the existence of a measurable second nearest neighbor interaction for these modes.[7] Between those values of g for which $U=0$, the group velocity is a negative quantity, but only its absolute value was used in the calculations.

DISCUSSION

The existence of the very intense prongs of diffuse scattering in [110] directions shown in Figs. 2 and 3 is due to the very small value of the velocity of the $t_{110(2)}$ mode. Referring to Fig. 1, if $\mathbf{g}$ is a vector from the 200 reflection in the [110] direction, then the unit vector $\mathbf{e}_{t110(2)}$ which points along the direction of oscillation of the $t_{110(2)}$ mode, lies in the *hko* plane and is perpendicular to $\mathbf{g}$. The unit vector of the other transverse mode, $\mathbf{e}_{t110(1)}$, is perpendicular to the *hko* plane. As can be

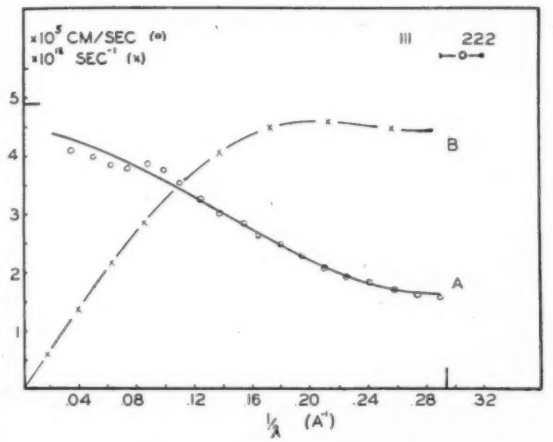

FIG. 8. Dispersion of the longitudinal mode in the [111] direction in β-brass at 295°K. Curve A is a plot of velocity ($\times 10^{-5}$ cm/sec) *vs* wave vector length (A^{-1}). Curve B is frequency ($\times 10^{-12}$ sec^{-1}) *vs* wave vector length (A^{-1}). The velocity intercept shown is that predicted by elastic theory.

seen from Table I, the small velocity of the $t_{110(2)}$ mode is predictable from the small difference in c_{11} and c_{12} for β-brass. Figure 3 shows only eight such prongs, however, and not the expected 12, which is due to the fact that the $\cos^2$ term is zero for this component in the four "missing" directions.

While the differences between the x-ray values of the elastic constants and those values obtained by Lazarus can be satisfactorily explained, nonetheless this particular x-ray technique is not well adapted for their determination. Wooster's[9] group at the Cavendish laboratory working close to crystalline reflections and thereby being able to use much smaller volume elements, have developed techniques for getting the elastic constants to a considerably greater degree of accuracy.

The dispersion curves, Figs. 4 through 9, have a form

[9] G. N. Ramachandran and W. A. Wooster, Acta Cryst. 4, 335 (1951).

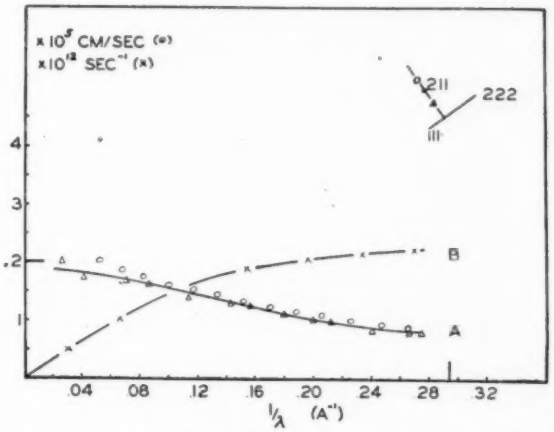

FIG. 9. Dispersion of the transverse mode in the [111] direction in β-brass at 295°K. Curve A is a plot of velocity ($\times 10^{-5}$ cm/sec) *vs* wave vector length (A^{-1}). Curve B is frequency ($\times 10^{-12}$ sec^{-1}) *vs* wave vector length (A^{-1}). The velocity intercept shown is that predicted by elastic theory.

similar to that of a weighted string, and actually can be approximated very well by an analytical expression of the form:

$$V^2=K^2\left[\left(\frac{\sin\pi g/2g_{max}}{\pi g/2g_{max}}\right)^2+B\left(\frac{\sin\pi g/g_{max}}{\pi g/g_{max}}\right)^2\right] \quad (2)$$

which is simply an expression for the velocity of a wave traveling along an infinite one-dimensional lattice of identical masses with second nearest neighbor coupling as well as nearest neighbor. B is a measure of the second nearest neighbor interaction. Of course this can at best be only a qualitative measure in the case of a three-dimensional system. A list of the values of K and B for the different modes is given in Table II. One noticeable feature is that B is higher for the longitudinal modes than for the transverse modes.

Except for the two peaks at small ν, the frequency distribution, Fig. 10, rises steadily and cuts off at some

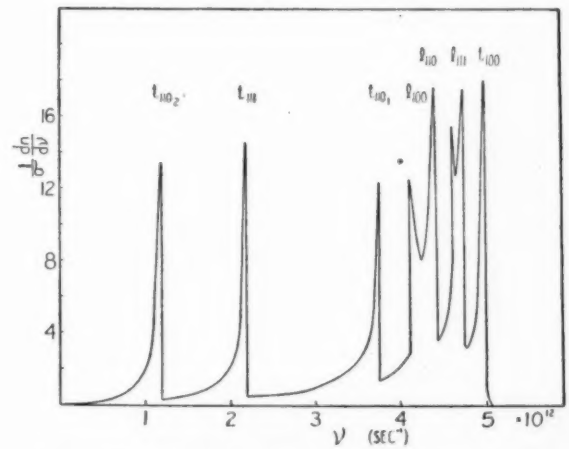

FIG. 10. An approximate frequency spectrum of elastic waves in β-brass at 295°K. $\sigma=4\pi v\times 10^9$ where v=volume of crystal in cm^3.

TABLE II. Values of the constants K and B of Eq. (2) for different elastic waves in β-brass at 295°K.

Mode	$K/10^8$	B
l_{100}	1.87	3.39
t_{100}	2.20	1.05
l_{110}	3.06	1.59
$t_{110(1)}$	2.44	0.67
$t_{110(2)}$	0.74	1.05
l_{111}	2.52	3.29
t_{111}	1.32	1.30

maximum frequency. It is within experimental error that the limiting frequency is the same for the three longitudinal modes. Therefore, the contribution of any longitudinal mode to the distribution function has probably been fairly accurately represented. However, the contributions of the transverse modes, for example, the two peaks at small ν, are highly questionable. If in Fig. 3 one moves along the surface of the Brillouin zone from a [110] direction to a [100] direction, the limiting frequency for the transverse modes propagating in these directions changes considerably. Therefore, it seems more likely that there should be a whole sequence of small peaks between those of the transverse modes shown in Fig. 10, rather than these few peaks in which the contributions of all the transverse modes have been lumped. In that case the final distribution might closely resemble that predicted by Debye.

The experimentally measured specific heat at very low temperatures could perhaps be used as a check on the existence of any low frequency peaks in the distribution function, since the calculated specific heat is sensitive to the shape of the distribution under the condition of nonequipartition of energy. But the assumption of equipartition holds for β-brass at room temperature, since the specific heat calculated on this basis:

$$c_V=\frac{1}{V\rho}\frac{d}{dT}(3NkT)=3N\left(\frac{k}{V\rho}\right)=\frac{3k}{v_a\rho},$$

where v_a is the volume of a primative cell and ρ the density, differs by less than 5 percent from Moser's[10] experimental value, and under this condition the specific heat at room temperature is merely a constant times the total area under the distribution curve, and does not depend upon the shape at all. The area under the curve in Fig. 10, $3N/\sigma$ or $3/4\pi V10^9$, is approximately nine-tenths of the predicted value.

We are indebted to Professor B. Averbach of the Department of Metallurgy for help and advice in the preparation of the single crystal of β-brass, and to Professors J. C. Slater and N. H. Frank for discussions of the frequency spectrum.

[10] H. Moser, Physik Z. **37**, 737 (1936).

Analysis of Certain Errors in the X-Ray Reflection Method for the Quantitative Determination of Preferred Orientations

WARREN P. CHERNOCK, *Argonne National Laboratory, Chicago, Illinois*

AND

PAUL A. BECK, *University of Illinois, Urbana, Illinois*

(Received November 14, 1951)

The reflection method for quantitative determination of pole figures, proposed by Schulz, proved to be limited with respect to the range of tilting angles in which satisfactory results can be obtained. It is shown that the previously unexplained decrease in the diffracted intensity with increasing tilting angle for specimens with random orientation distribution can be accounted for on the basis of an elementary analysis of defocusing effects. Experimental evidence is presented to show that variation of the receiving slit length and of the main slit width has the effect predicted by the analysis. The importance of accurate specimen alignment is discussed, and a satisfactory alignment check procedure is described.

INTRODUCTION

AN improved quantitative reflection method for determining pole figures was proposed by Schulz.[1] This very useful method was stated to give accurate results within an angle range up to about 75° from the center of the pole figure. Other investigators,[2] using the method with a different spectrometer unit, found considerable decrease of the indicated intensity at about 50°–60° away from the center. These differences have not been satisfactorily explained; one of the aims of the present work is their clarification. It was expected that by investigating the causes of the intensity decrease, it will become possible to minimize them, thereby extending the useful angle range.

Effect of Flatness of the Specimen

It is well known that true focusing is achieved under ideal spectrometer geometry conditions only, where the focal point of the x-ray beam, the specimen surface, and the Geiger counter receiving slit all lie on the same circle. The radius of this circle is equal to the radius of curvature of the cylindrical specimen surface. Figure 1 demonstrates the geometric conditions when a flat specimen is used. It is obvious that only point B, the point of tangency of the specimen surface with the spectrometer circle, corresponds to ideal spectrometer geometry in this case. If the x-ray beam is of such dimensions that only an area immediately adjacent to point B is irradiated, a sharp intensity maximum will be observed at the proper Bragg angle. When a larger area of the specimen surface is irradiated, such as is necessary in practical application for texture determination, the entire diffracted beam is not sharply focused at F_2, and as a result a portion of the beam is not passed by a very short detector slit at F_2. This portion of the diffracted beam is, of course, not contributing to the measured intensity. However, as a result of the finite length L_2 of the detector slit (the nomenclature used here is the same as that in reference 1), a certain length $x\,y$ along the specimen surface can be irradiated without noticeable loss of measured x-ray intensity. Many years of experience with setups of this type indicates that under practical operating conditions the length of the irradiated flat specimen surface and the length of the detector slit can be controlled so that no serious difficulties arise from the flatness of the specimen. The focusing difficulties are, however, greatly increased when cylindrical or spherical specimens are used, for which the center of curvature and the center of the spectrometer circle are on opposite sides of the reflecting specimen surface.[3]

Effect of Misalignment

An important condition for satisfactory operation of a reflection specimen holder for texture work is that the focusing conditions should remain unchanged when the specimen orientation is varied. To fulfill this condition in the arrangement described by Schulz, the reflecting specimen surface must be accurately aligned

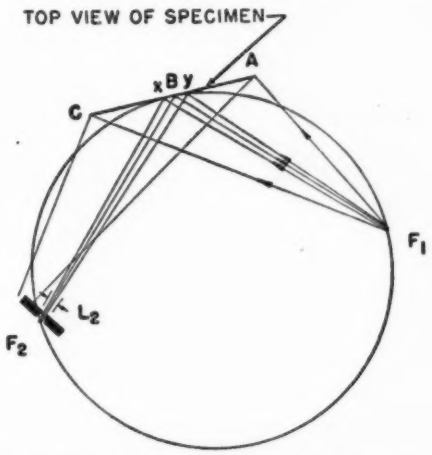

FIG. 1. Spectrometer geometry with flat specimen.

[1] L. G. Schulz, J. Appl. Phys. **20**, 1030 (1949).
[2] H. Hu and P. A. Beck, Am. Inst. Mining. Engrs. J. Metals, 1214 (October, 1950).
[3] J. T. Norton, J. Appl. Phys. **19**, 1176 (1948).

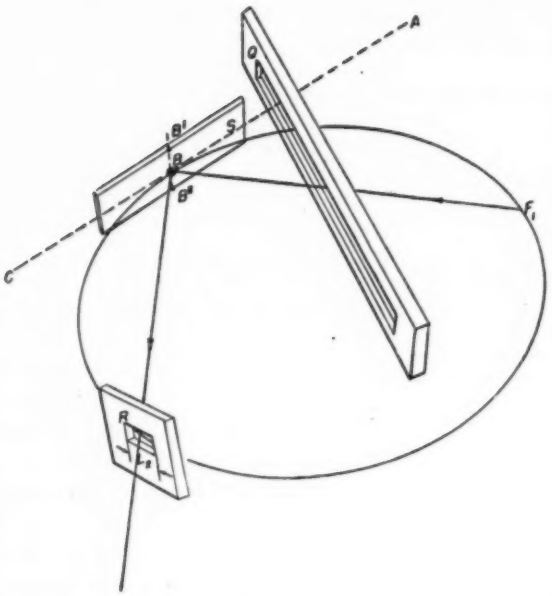

FIG. 2. Perspective view of principal components of spectrometer arrangement according to L. G. Schulz. F_1, focal point of primary x-ray beam; Q, main slit; R, receiving slit; S, flat reflecting specimen surface.

so as to contain one of the axes of rotation and be perpendicular to the other. When the specimen is positioned accurately, rotation of the specimen about an axis corresponding to CA (Figs. 1 and 2) may be accomplished without lateral movement of point B. This is shown in Fig. 3 for three tilting angles ϕ_1, ϕ_2, and ϕ_3, as viewed through the main slit (Q in Fig. 2) from the direction of A. When the specimen is not aligned accurately (Fig. 4), a change in ϕ is accompanied by a lateral displacement of point B and of the irradiated area of the specimen. This displacement results in a movement of the focal point F_2 (defocusing) of the diffracted rays, as shown in Fig. 5, where S_1 and S_2 correspond to specimen positions ϕ_1 and ϕ_2 of Fig. 4. (B'' in Fig. 5 corresponds to B_2 in Fig. 4.) The movement of point F_2 brings about an apparent change in the Bragg angle, as shown in Fig. 6. The x-ray intensity received by the Geiger counter in a position corresponding to $2\theta_1$ is I_1 when the specimen is in position S_1, and I_2 when the specimen is displaced to position S_2 (Fig. 5). The decrease in measured intensity resulting from the apparent change in Bragg angle is then superimposed on the intensity variation corresponding to changing angle ϕ as a result of preferred orientation and prevents the accurate measurement of the latter. It was found that the change in the apparent 2θ-value with a change of 45° in ϕ may be as large as 0.5° or as small as 0.03°, depending upon the care taken in aligning the specimen. Measurements of the apparent Bragg angle with varying ϕ may be used to check the accuracy of alignment of a specimen. A variation of 0.05° in 2θ between three specimen positions ($\phi=0°$, $\phi=45°$ clockwise, and $\phi=45°$ counterclockwise)

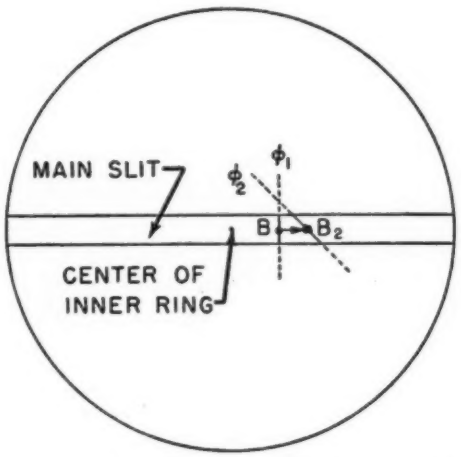

FIG. 4. Inaccurately aligned specimen in two positions.

was found to be the maximum allowable deviation for specimen alignment for reliable texture determination.

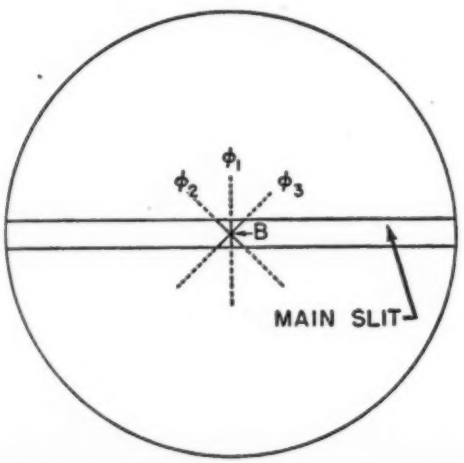

FIG. 3. Accurately aligned specimen in various positions.

Effect of Slit Dimensions

Figure 2 shows the specimen in a position where the surface S is perpendicular to the plane of the spectrometer circle. Line ABC is the intersection of the specimen surface with that plane, and it is tangent to the spectrometer circle at B. Line B′ B B″ is in the specimen surface and perpendicular to line ABC. In Fig. 1, which gives the top view of the specimen when the specimen surface is perpendicular to the plane of the spectrometer circle, points B, B′, and B″ are all superimposed. The same situation is shown in Fig. 7, as seen from the direction of A. Rotation of the inner ring of the specimen holder corresponds to rotation of the specimen about axis CA (Fig. 2). Points B′ and B″ at the upper and lower edges of the irradiated area of the tilted specimen (Fig. 7) no longer satisfy the ideal conditions of focusing, since B′ moves toward the center of the spectrometer circle, and B″ moves away

from it. The effect of these movements is defocusing as is shown for B″ in Fig. 5. With the specimen displaced from S_1 to S_2, the focal point shifts from F_2 to F_2'. Correspondingly, the spectrometer shows an apparent decrease in the Bragg angle from $2\theta_1$ to $2\theta_2$, (Fig. 6), and the x-ray intensity received by the Geiger counter through slit F_2 in its position corresponding to $2\theta_1$ may be very much smaller with the specimen at S_2 than with the same specimen in its position S_1. If the specimen is accurately aligned, the effective specimen displacement and the apparent change in Bragg angle for B′ is of the same magnitude but in the opposite direction. Here, too, the intensity received through the slit F_2 decreases. The net effect of tilting a well-aligned specimen is an apparent widening of the diffraction line, resulting from the apparent changes in Bragg angle toward lower values for the lower half of the specimen and toward higher values for the upper half of the specimen

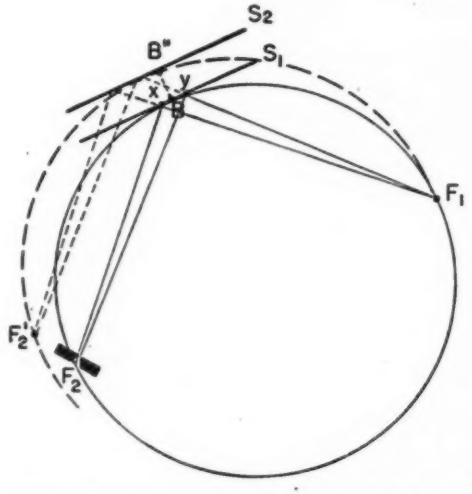

FIG. 5. Defocusing as a result of displacement of flat specimen.

for a counterclockwise rotation of the specimen. This line widening may be so large (see Fig. 9) that an important portion of the diffracted intensity is not received by the Geiger counter through the slit length L_2. The indicated intensity is then expected to decrease as ϕ is increased. This is actually observed, as shown in curve 1 of Fig. 10. This intensity decrease constitutes a severe limitation of the ϕ angle range in which the reflection method can be used.

Actually, there is a certain range of tilting angle, ϕ, within which the defocusing does not lead to significant loss of intensity. This range is controlled by the detector slit length, L_2 (Fig. 2). If L_2 is larger, a larger extent of defocusing may be tolerated without much loss of intensity, and consequently, a larger range of ϕ may be used. This effect was experimentally investigated. A random specimen was obtained by placing PbS powder mixed with glue into a rectangular cavity in a Bakelite slide. The specimen surface was gently smoothed with the blade edge of a knife, while the glue

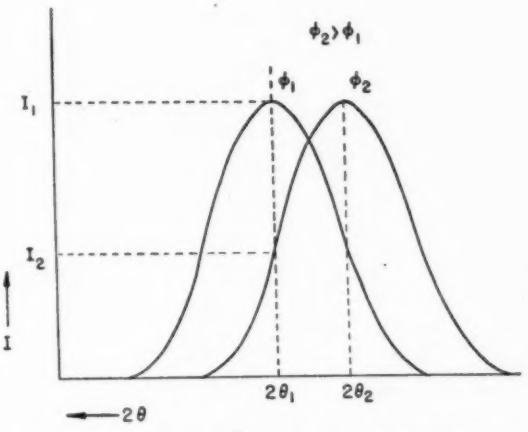

FIG. 6. Shift of the apparent Bragg angle (2θ) resulting from change in the specimen tilt angle (ϕ).

was still wet, until the surface of the powder specimen was aligned with the surface of the Bakelite slide. The slide was then mounted on the specimen holder and accurately aligned. The (200) reflection for PbS was found at a 2θ-value of 30.02°. The Geiger counter was set at this 2θ-value and intensity measurements were made as a function of ϕ, with various detector slit and main slit dimensions. Figure 10 gives the percentage decrease of measured intensity as a function of increasing ϕ for various detector slit lengths (L_2). The percentage decrease of measured intensity is defined as $(I_0-I_x)/I_0 \times 100$, where I_0 is the measured intensity at a ϕ-value of 0°, and I_x is the measured intensity at varying ϕ-values. An increase of L_2 was achieved by removing the detector slit (curve 2) and by removing the detector slit mount, as well as the plate (curve 3), in front of the Geiger counter of a General Electric XRD-3 x-ray spectrometer. The experimental conditions are summarized in Table I. In this series of experiments ϕ_{10} (defined as the angle at which 10 percent intensity decrease is observed with a random specimen) was increased from 22° to 40° by increasing the detector slit length.

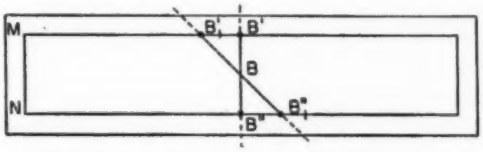

FIG. 7. Specimen surface at two different tilt angles, as seen through the main slit from direction A (see Fig. 2).

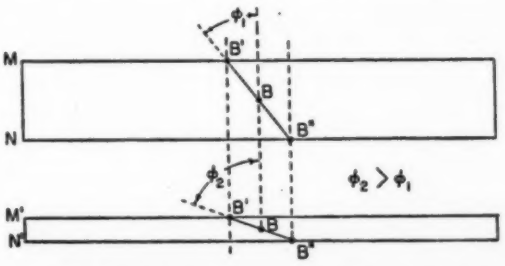

FIG. 8. Effect of main slit width on limit of tilt angle.

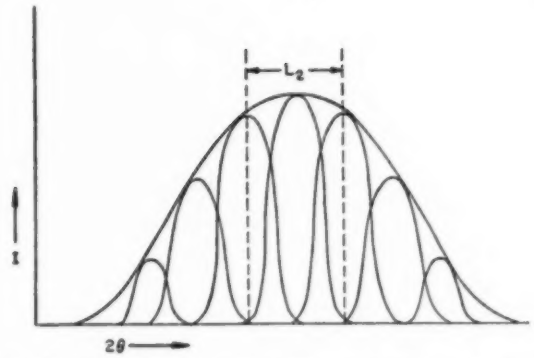

FIG. 9. Increase in apparent line width as a result of defocusing.

The removal of the entire slit mount as well as the plate in front of the Geiger tube is accompanied by a large decrease in the angular resolution obtainable with the spectrometer. For materials with cubic crystal structure, the decrease in resolution is usually not important since there is in most cases a large angular separation between reflections from different crystal planes, and overlapping of adjacent reflections is not very probable. However, the line position and line width relationships must be carefully examined before the method is applied to noncubic substances, where the angular separation of adjacent reflections may be rather small and the increased width of the intensity maxima may cause overlapping of adjacent reflections. In such cases, the required angular resolution may necessitate the use of a small detector slit length, which in turn restricts the useful range of ϕ.

Another factor affecting the constancy of the measured diffracted intensity of a random specimen with varying ϕ is the width MN (Fig. 7) of the main slit. The effect of a decrease in the main slit width from MN to M′N′ is shown in Fig. 8. It is seen that the ϕ-value for equal displacement of B″ from the spectrometer circle increases from ϕ_1 to ϕ_2 when the slit width is decreased from MN to M′N′. The effect of decreasing the main slit width from 0.040 in. to 0.020 in. and to 0.005 in. was studied experimentally by means of the random sample described previously. The experimental conditions are summarized in Table I, and the results are shown in Fig. 11. It is clearly seen that ϕ_{10} has been increased by a decrease in the main slit width. The gain resulting from a decrease of the main slit width from 0.020 in. to 0.005 in. is relatively small, probably because under the experimental conditions the slit width effect became small enough to be comparable with the misalignment effect discussed previously. On the other hand, the use of a 0.005-in. main slit in place of the 0.040-in. slit decreased the x-ray intensity and thus increased the counting time by a factor of eight. Further decrease of the main slit width and still longer counting time would be justified only if the accuracy of the alignment procedure could be appreciably increased. As expected, it was found that the increase in ϕ_{10} is largest when the detector slit length is short. Practically no improvement in the uniformity of response was obtained by decreasing the main slit width when the detector slit had its maximum length.

TABLE I. Experimental conditions for determining the decrease of intensity as a function of θ for a random sample.

Variation of detector slit length	Main slit width	Total no. of counts	Percent probable error	Results shown Figure No.	Curve No.
0.2° Detector slit	0.020″	4096	1.0	10	1
Detector slit mount removed	0.020″	16,384	0.5	10	2
Slit mount and plate in front of Geiger counter removed	0.020″	16,384	0.5	10	3
0.2° Detector slit	0.040″	2,048	1.5	11	1
0.2° Detector slit	0.020″	1,024	2.0	11	2
0.2° Detector slit	0.005″	1,024	2.0	11	3

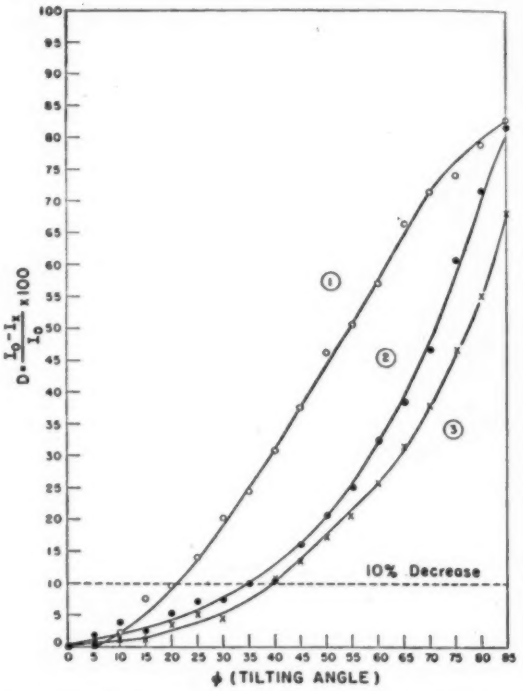

FIG. 10. Diffracted x-ray intensity as a function of tilt angle, with increasing receiving slit length (see Table I).

With a 0.2° detector slit two adjacent reflections were completely resolved, even when their 2θ-values did not differ by more than 1°. With the equipment used, counting times were not excessively long when a 0.020-in. main slit width was used. The variation of intensity with changing ϕ under these conditions is shown by curve 1 of Fig. 10. The ϕ_{10} value for this curve corresponds to about 22°. It is thus possible to determine a fiber texture from three reflection specimens only if the angles of the three reflecting surfaces with respect to the fiber axis are properly chosen. For instance, a longitudinal section, cut parallel to the rolling direction of a rolled rod, may be used to determine the central portion of the pole figure, up to 25° away from the center. A cross section, perpendicular to the rolling direction, may be used to determine the area of the

pole figure lying between the rolling direction and 25° away from the rolling direction. A section cut at 45° to the rolling direction may then be used to determine the rest of the pole figure. The region of overlap of the areas plotted from two sections may be used as a further check of specimen alignment. If three specimen sections are to be used, each section must be carefully aligned on the specimen holder. A "slit stop" mechanism may be used to limit the effective length of the main slit. It is desirable to use the greatest length which will assure that the x-ray beam is entirely intersected by the reflecting specimen surface in all specimen positions. When three sections are used, as described previously, the 45° section usually requires the most severe limitation of slit length. The other two sections may then be studied without changing the setting of the "slit stop," in order to obtain directly comparable counting rates.

CONCLUSIONS

It may be concluded that the decrease in diffracted beam intensity with increasing specimen tilting angle, which often becomes very important at angles of approximately 40°–50°, is a result of defocusing. The useful tilt angle range can be increased by decreasing the defocusing effects. This can be accomplished by very accurate specimen alignment, by decreasing the width of the main slit, and by increasing the receiving slit length. The last method is particularly effective, but it results in a decrease in angular resolution and, in some cases, in insufficient separation of reflections from different crystal planes.

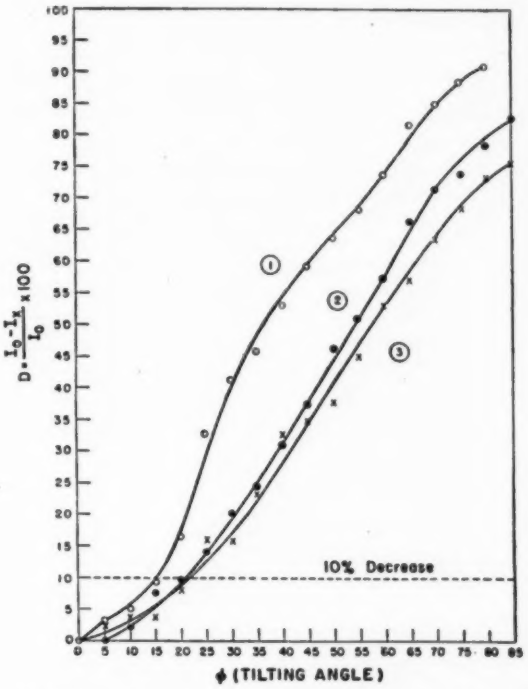

FIG. 11. Diffracted x-ray intensity as a function of tilt angle, with decreasing main slit width (see Table I).

ACKNOWLEDGMENTS

The investigation was carried out at the Metallurgy Division of Argonne National Laboratory. The authors wish to express their appreciation to Dr. F. G. Foote and Dr. M. H. Mueller of that organization for helpful discussions.

Correlation of DC and Microsecond Pulsed Emission from Oxide Coated Cathodes*

FRANK A. HORAK
Department of Physics, University of Missouri, Columbia, Missouri
(Received November 19, 1951)

This report describes a study of dc and microsecond pulsed emission from oxide coated cathodes prepared on four different base metals. One of the base metals used was pure electrolytic nickel and the other three had impurities of 0.2 percent silicon, 4 percent silicon, and 4.7 percent tungsten added to the nickel. The flat base metal cathode was coated with equal molar barium-strontium carbonate. The tubes were placed on life test at a cathode temperature of 1125°K with no emission current drawn. Dc and pulsed emission measurements were taken periodically. Three methods were used to measure the zero field emission current, (1) dc retarding potential, (2) dc Schottky, and (3) pulsed Schottky. These gave essentially the same Richardson plot indicating a positive correlation of dc and pulsed emission. From these Richardson plots obtained using methods (1) and (3), the work function, the emission constant, and J_0, the characteristic emission current density at 650°K, were determined. The results show that the different cathode base metals control the variation in emission with life. The emission from the tungsten-nickel base metal is stable with life and is of much higher value than the other base metals.

INTRODUCTION

THE dc thermionic emission properties of oxide coated cathodes were well known before World War II as reported by Becker[1] and Blewett.[2] The extensive use of pulsed electron tubes during the war aroused much interest in the properties of oxide coated cathodes under pulsed condition. Sproull[3] observed a decay in the thermionic emission of pulsed oxide cathodes and Coomes[4] reported that unusually large electron emission currents are available in microsecond pulses. From early diode experiments[4] it appeared that definite correlations of a simple nature did not exist. Higher pulsed than dc emission values are usually quoted but always for relatively high cathode temperatures. The pulsed emission level at these temperatures is so high that the dc emission limitation is probably imposed by a poisoning of emission caused by excessive anode dissipation rather than a fundamental restriction on the dc emission process itself. A space charge limited dc current density of 18 A/cm² observed by Dillinger[5] in 1947 also strongly suggests that the same mechanism may apply to both types of emission.

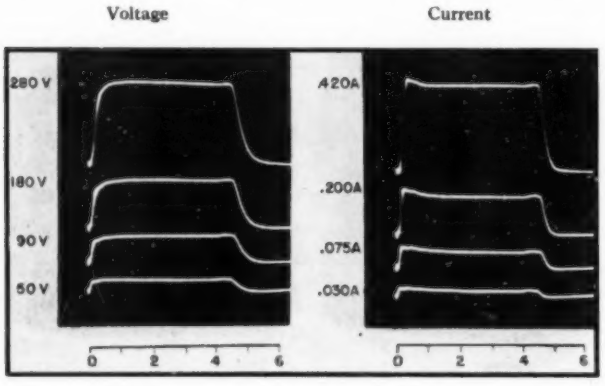

FIG. 1. Current and voltage pulses used for emission measurements.

In 1949 Bien[6] reported that over restricted temperature ranges, the temperature variation of pulsed and dc thermionic emission is essentially the same. Bien studied the microsecond pulsed currents from cathodes at temperatures between 850° and 700°K and dc currents below 600°K. These temperature ranges were used to avoid a dc emission decay which occurred above 600°K, and a pulsed emission decay which was noticeable above 850°K. Pulsed currents could not be measured below 700°K.

This paper describes a study of the dc and microsecond pulsed emission currents obtainable from oxide coated cathodes prepared on four different base metals. These cathodes were life tested under quiescent conditions, i.e., no emission current was drawn, and emission values were determined as a function of life.

EXPERIMENTAL TECHNIQUES

Cathodes used in this study were prepared on four base metals.[7] One of the four base metals used was the pure electrolytic nickel 1001 and the other three had major impurities of 0.2 percent silicon, 4 percent silicon, and 4.7 percent tungsten. A nickel button from the different base metals was hydrogen fired and mounted on a standard 2C39 flat cathode.[8] It was then mounted in a blank and outgassed at 1050°C in vacuum. A 0.002-in. Mo-Ni thermocouple was attached to the base metal for measuring the temperature. The cathodes were sprayed with equal molar barium-strontium carbonate coating (Raytheon C51-2) of 10 mg/cm² on the 0.5 cm² area. The tantalum anode was outgassed at 1300–1400°C by radio frequency heating and electron bombardment from a tungsten filament. The outgassed

* Supported in part by the ONR.
[1] J. A. Becker, Phys. Rev. **34**, 1332 (1929).
[2] J. P. Blewett, Phys. Rev. **55**, 713 (1939); J. Appl. Phys. **10**, 831 (1939).
[3] R. L. Sproull, Phys. Rev. **67**, 166 (1945).
[4] E. A. Coomes, J. Appl. Phys. **17**, 647 (1946).
[5] J. R. Dillinger, Ph.D. thesis, University of Wisconsin (1947).
[6] R. B. Bien, Technical Report No. 73, M.I.T. (1949).
[7] Obtained from the International Nickel Company.
[8] Obtained from the Machlett Company, Inc.

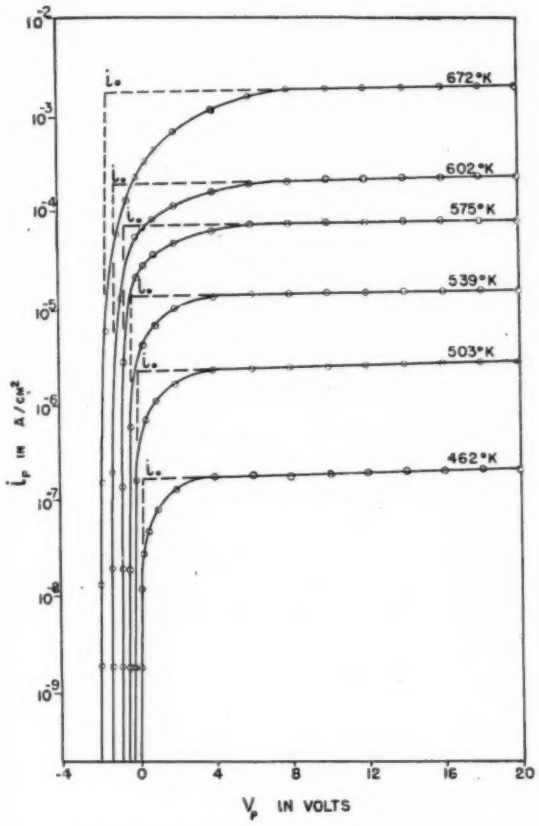

FIG. 2. Dc retarding potential plots for 4.7 percent W-Ni base cathode at 476 hours life.

parts of the tubes and a batalum getter were assembled to form a plane parallel geometry diode having an anode-cathode spacing of about 2 mm. The tube was baked out at 450°C, the cathode was converted and activated, the tube was sealed off at a pressure less than 10^{-8} mm of Hg, and the getter flashed. After seal off, the tubes were placed on life test by heating the cathodes to 1125°K with no emission current drawn. Cathodes were held at a constant temperature which was measured by a calibrated Mo-Ni thermocouple.[9] Three methods were used to measure the zero field emission currents, (1) the dc retarding potential, (2) the dc Schottky, and (3) the pulsed Schottky. Standard experimental techniques were employed in the dc methods. For the pulsed emission measurements a square voltage pulse of about four microsecond at a repetition frequency of 60 pps was applied to the anode, and the emission current was measured using a Sylvania Model *P*-4 synchroscope. In order to extend the current range beyond that which could be measured directly on the synchroscope, a pulse amplifier whose gain was about 1000 was inserted in the circuit. The type of voltage and current pulses which were used in these measurements are shown in Fig. 1.

[9] I. L. Sparks, Ph.D. thesis, University of Missouri (1951).

RESULTS

Typical plots of data used to determine the zero field emission current are shown in Figs. 2, 3, and 4. The cathode for which this data was taken was one of those which was prepared on a 4.7 percent W-Ni base and was operated quiescent for 476 hours. Figure 2 shows a set of dc retarding potential plots for this cathode at various temperatures. The anode current expressed in terms of current density at the cathode is plotted as a function of the applied anode voltage. Zero field current values i_0 were obtained at each temperature from the intersections of the dotted lines drawn as shown in the figure. Figure 3 shows a set of dc Schottky plots for the same diode at various temperatures. Extrapolating the curves to the zero voltage axis give the zero field currents. Figure 4 shows a similar set of pulsed Schottky plots for the same diode. Again extrapolating to zero voltage axis give the zero field currents. At low temperatures an emission decay with time was observed at high anode voltages and accounts for this deviation from the Schottky line. Richardson plots were constructed from the above sets of zero field emission currents and used to evaluate the

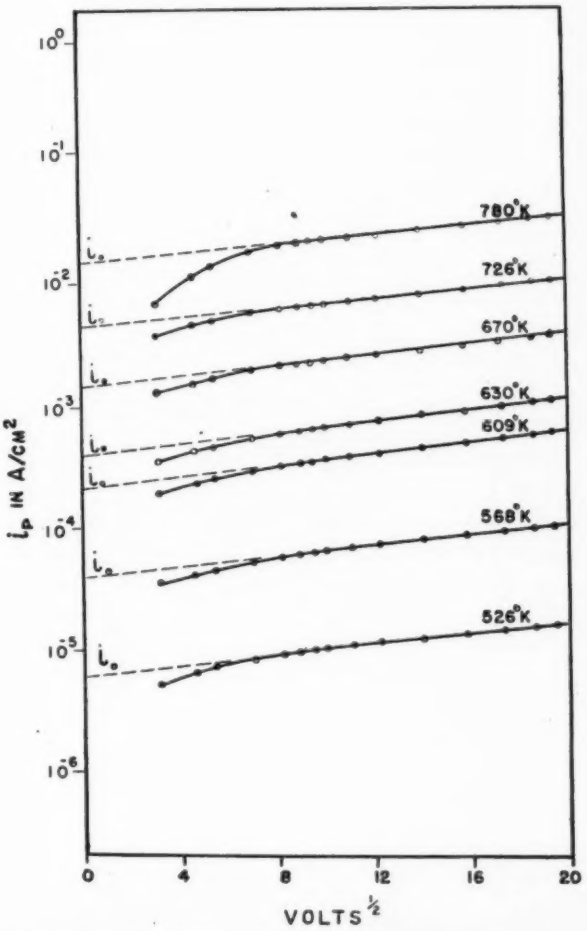

FIG. 3. Dc Schottky plots for 4.7 percent W-Ni base cathode at 476 hours life.

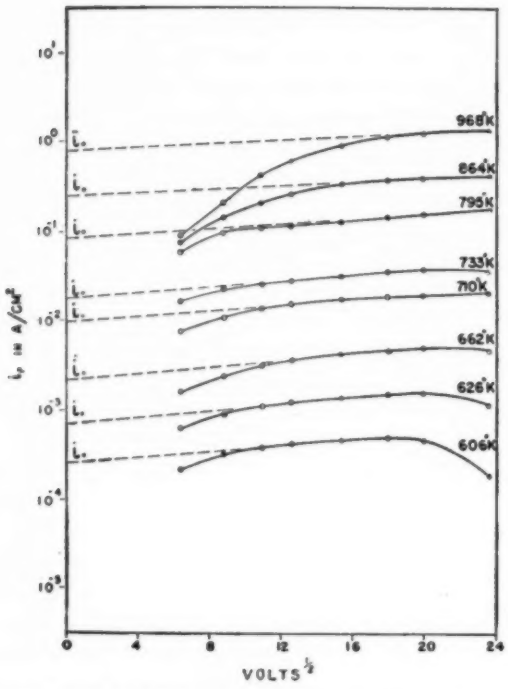

FIG. 4. Pulsed Schottky plots for 4.7 percent W-Ni base cathode at 476 hours life.

thermionic work functions and emission constants. The resulting curves are shown in Fig. 5. It is seen that all points fall essentially on the same straight line, independent of whether these current values were determined by using the retarding potential or Schottky plots for the dc currents or the Schottky plots for the pulsed currents. Points *A* and *B* from the dc Schottky plot and point *C* from the pulsed Schottky plot, show an apparent deviation from this straight line. In the case of point *C* this apparent deviation is a result of the space charge limitation of the emission and thus sets an upper limit to the pulsed current measurement with our present equipment. Points *A* and *B* deviate because of an emission decay which was readily observable at high accelerating fields. Thus the cathode was not in the same state of activity at these two points.[10] Because of these limitations, dc emission currents could be measured at temperatures from 450 to 700°K and

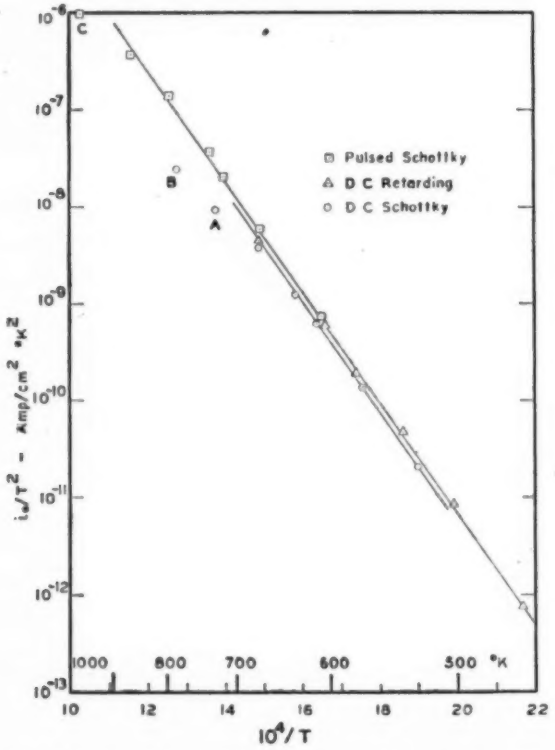

FIG. 5. Richardson plots for 4.7 percent W-Ni base cathode at 476 hours life using zero field currents from Figs. 2, 3, and 4.

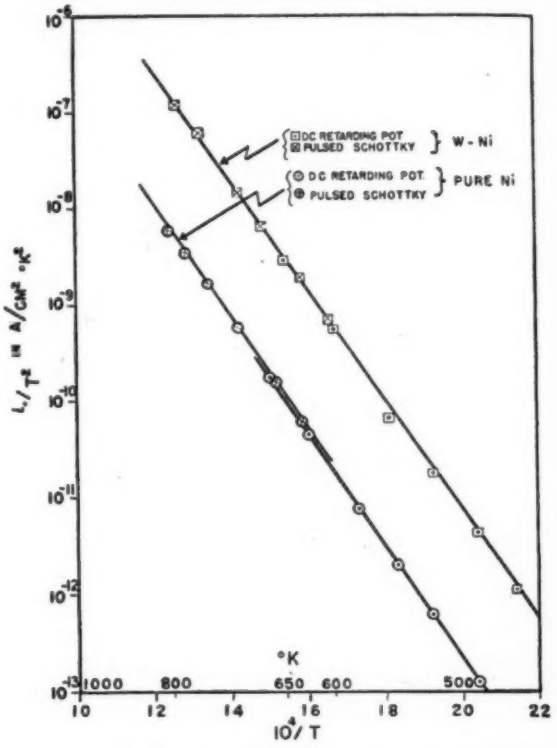

FIG. 6. Richardson plots for pure Ni and 4.7 percent W-Ni base cathodes at zero hours life.

pulsed emission currents measured from 600 to 900°K for cathodes of moderate activity. This gave an overlapping temperature range of about 100 degrees and an overlapping current range of more than one order of magnitude.

Richardson plots for pure nickel and tungsten nickel base cathodes at zero hours life are shown in Fig. 6 for comparison. The emission current obtainable from the W-Ni is about 1.5 orders of magnitude higher than that from the pure nickel. Here again the similarity of the dc and pulsed emission values can be seen.

Diodes were prepared on each of the four base metals and at progressively increasing points in life, dc retarding potential and pulsed Schottky data were taken

[10] D. A. Wright, Proc. Phys. Soc. (London) **62**, 398 (1949).

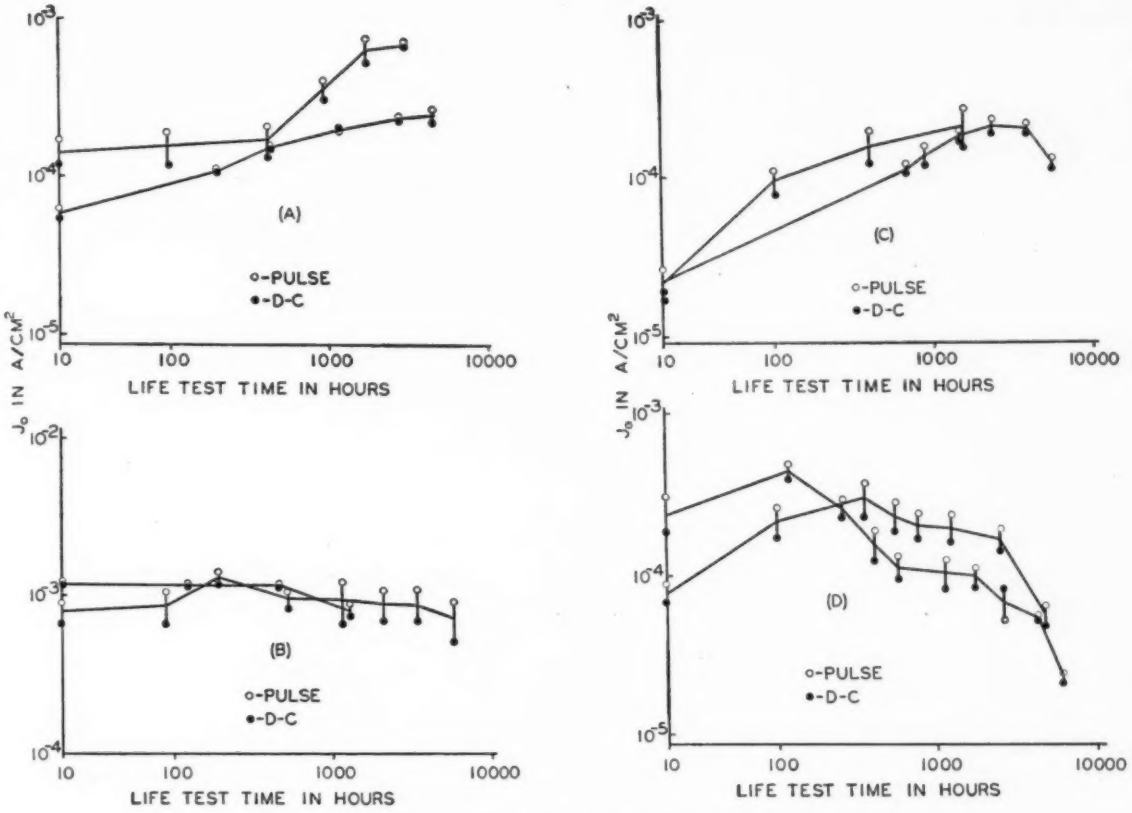

FIG. 7. Emission at 650°K for cathodes under quiescent life test. (A) Pure nickel; (B) 4.7 percent W-Ni; (C) 0.2 percent Si-Ni; (D) 4.0 percent Si-Ni.

and used to make Richardson plots. From these plots, values of the work function and emission constant were obtained as well as J_0, the characteristic zero field emission at 650°K. Work function values between 1.0 and 1.3 ev were observed for these cathodes but significant variations were not found with different base material or increasing life. A comparison of J_0 values for two tubes of each cathode type is shown in Fig. 7 as a function of cathode life. The emission from the 4.7 percentage W-Ni is higher and shows less variation with life than that from the other base materials. In the chemical development of its interface,[11] Ba_3WO_6, an oxygen deficiency is probably produced in the coating which gives rise to the high state of thermionic activity. Hensley and Affleck[12] have shown that this interface thickness does not increase appreciably with life, and thus the chemical reaction does not continue rapidly after the initial activation. In the case of the 4 percent Si-Ni, it is seen that at the outset there is a slight rise but later a rapid drop in emission. The drop might be associated with the continued formation of the Ba_2SiO_4 interface. Eisenstein[13] has shown that for the 4 percent Si-Ni base metal the interface thickness increases with life. The decrease in emission with time may be due to the eventual depletion of Ba in the coating through the interface formation. The pure nickel and 0.2 percent Si-Ni both show only a gradual rise in emission due to the less rapid production of impurity centers. Both dc and pulsed values are shown on these curves which are drawn through the average of two values. In most cases the pulsed currents are slightly above the dc emission currents but by a factor of less than two. It is doubtful if any significance should be attached to this difference.

[11] H. P. Rooksby and E. G. Stewart, Nature **157**, 548 (1946).
[12] E. B. Hensley and J. H. Affleck, J. Appl. Phys. **21**, 938 (1950).
[13] A. S. Eisenstein, J. Appl. Phys. **20**, 776 (1949).

CONCLUSION

The three methods used for measuring the zero field thermionic emission, the retarding potential, the dc Schottky, and the pulsed Schottky plots, give essentially the same Richardson line, and thus the same work function and effective "A" constant. The different cathode base materials used seem to control the variation of emission with life which may be explained in terms of the interface formation. The emission from the W-Ni cathode is stable with life and of much higher value than that from the other base metals.

The author wishes to acknowledge the generous support of this work by the ONR and by the University Research Council. It is a privilege to express his appreciation to Professor Albert S. Eisenstein, not only for his assistance in the selection of the problem but also for his valuable suggestions in the preparation of this manuscript.

The Allotropic Transformation of Hafnium and a Tentative Equilibrium Diagram of the System Zirconium-Hafnium

J. D. FAST
Philips Research Laboratories, N. V. Philips' Gloeilampenfabrieken, Eindhoven, Netherlands
(Received November 20, 1951)

The temperature of the transformation in hafnium is at least 550°C higher than the value recently reported by Duwez (1310°±10°C). A tentative equilibrium diagram of the system zirconium-hafnium is given.

INTRODUCTION

IN 1939 the electrical resistance of a 97 weight percent Hf−3 weight percent Zr rod was measured as a function of the temperature. These measurements confirmed the existence of an allotropic transformation in hafnium, predicted in 1926 by Zwikker,[1] who examined the thermal behavior of hafnium with a much greater zirconium content. Because of the outbreak of the war the investigation was interrupted. It was intended to continue the measurements on much purer hafnium after the war but up until now there was no opportunity to do so. A recent paper by Duwez,[2] however, causes us to publish our results obtained in 1939. Although it is not yet possible to give the exact transformation temperature of pure hafnium, it certainly lies several hundred degrees above that reported by Duwez. In this paper it is given as 1950°±100°C.

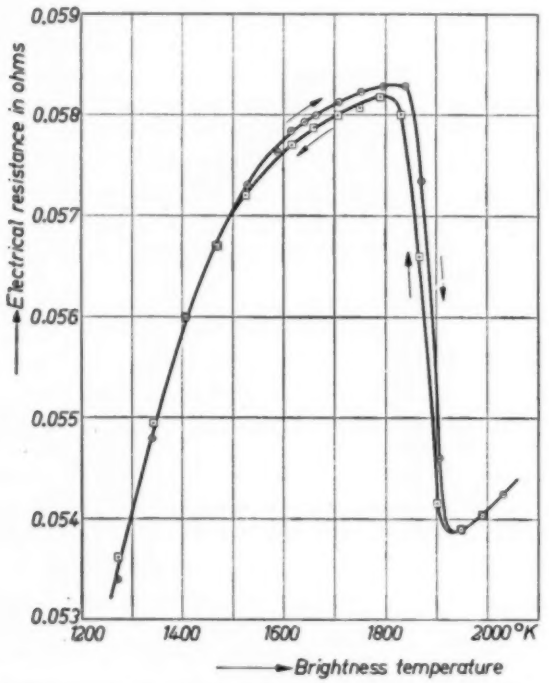

FIG. 1. Electrical resistance of a 97 weight percent Hf−3 weight percent Zr rod 0.98 mm in diameter and 25.5 mm long as a function of the brightness temperature.

[1] C. Zwikker, Physica **6**, 361 (1926).
[2] P. Duwez, J. Appl. Phys. **22**, 1174 (1951).

ELECTRICAL RESISTANCE MEASUREMENTS

The 97 weight percent Hf−3 weight percent Zr rod used for the investigation was obtained by first preparing a rod of 1.5-mm diameter by the Eindhoven iodide process[3] and then cold-swaging it to a final diameter of about 0.98 mm. The specific gravity of this hafnium was 12.90.

A length of 65 mm of the 0.98-mm rod was mounted between two poles of a four-pole bridge. The other two poles were connected through thin tungsten wires with two points of the rod about 25.5 mm apart; they were used for voltage measurements. The mounted bridge was sealed in a glass vessel and this in turn was sealed to a high vacuum pump. After the evacuation and the degassing of the apparatus the hafnium rod was heated by passing direct current through it. At several currents the voltage and the temperature were measured, the latter with the aid of an optical pyrometer with a red filter. At the higher temperatures the wall of the glass vessel was slightly blackened by evaporating metal. Each brightness temperature measured was corrected for the absorption by the wall.

Figure 1 giving the results of the measurements shows that the transformation range for this material extends from about 1830°K to about 1930°K brightness temperature. According to C. Zwikker (unpublished results) the emission coefficient of both zirconium and hafnium is 0.45 for $\lambda=0.652\mu$. With this value of the emission coefficient we find for the transformation range 1960°K–2075°K or 1690°C–1800°C. The fact that the transformation does not take place at a well-defined temperature but extends over a range is of course due to the presence of impurities, mainly, to the 3 percent Zr. It may be that traces of oxygen enlarged the range. From measurements on zirconium[4] it is known that even small quantities of oxygen give a marked transformation range, the beginning of the transformation being shifted to only slightly higher temperatures and the end to much higher temperatures. The same applies to titanium.[5] Only "virgin" metal, i.e., zirconium or titanium that had never been in contact with the air, showed a sharp transformation point. Even the invisible

[3] J. H. de Boer and J. D. Fast, Z. anorg. u. allgem. Chem. **187**, 193 (1930).
[4] J. H. de Boer and J. D. Fast, Recueil Trav. Chim. Pays-Bas **55**, 459 (1936).
[5] de Boer, Burgers, and Fast, Proc. Kon. Ak. Wetensch. Amsterdam **39**, 515 (1936).

oxide layer formed at room temperature gives a small range after dissolving in the metal during vacuum heating.

LATTICE CONSTANTS

The values of the lattice constants of 100 percent Zr and 100 percent Hf[6] are given in Table I together with the values reported by Duwez for his hafnium. The main impurity of hafnium is always zirconium. From our pre-war measurements we know that the atomic volumes of Zr and Hf in their alloys are virtually additive. This enables us to draw the conclusion that the composition of Duwez' alloy is approximately 81 atomic percent Hf—19 atomic percent Zr.

TABLE I. Lattice constants of 100 percent Zr and 100 percent Hf.

Material	a	c	c/a
100 percent Zr	3.225A	5.134A	1.592
100 percent Hf	3.187	5.041	1.582
Hf-Duwez	3.195	5.057	1.583

TENTATIVE EQUILIBRIUM DIAGRAM Zr-Hf

It was always assumed, and the experiments of Duwez[2] give some evidence, that the crystal structure of the high temperature modification of hafnium is the same as that of zirconium and titanium, i.e., body-centered cubic. Considering the small difference in atomic volume between Zr and Hf, this would almost certainly imply that these metals form an uninterrupted series of solid solutions not only in their hexagonal but also in their cubic forms. Taking into account the low transformation temperatures found by Zwikker and Duwez and considering that 3 weight percent Zr corresponds to 5.7 atomic percent Zr, we get the tentative equilibrium diagram shown in Fig. 2. According to this diagram the transformation range of hafnium changes so strongly with the zirconium content, that the extrapolation to pure hafnium becomes very uncertain. The most reliable value of the transformation point of Hf seems to be 1950°±100°C.

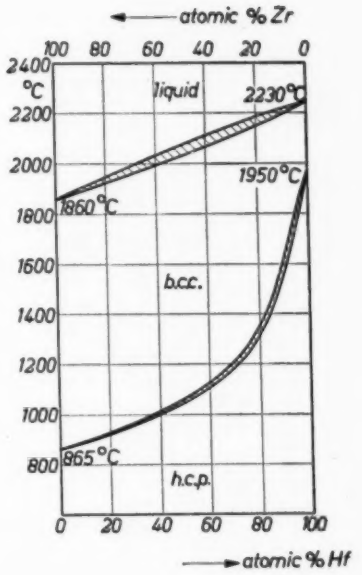

FIG. 2. Tentative equilibrium diagram of the system zirconium-hafnium.

The diagram indicates that the value of the enthalpy of mixing of hexagonal Zr and Hf is greater (more positive or less negative) than that of the metals in their cubic forms. The same was found to apply to Zr and Ti.[7] In the latter case the transformation points of both metals are about the same, so that the difference in the enthalpies of mixing causes a minimum in their transformation point diagram.

[6] J. D. Fast, Chem. Weekblad **44**, 621 (1948).

[7] J. D. Fast, Recueil Trav. Chim. Pays-Bas **58**, 973 (1939).

Physical Structure and Magnetic Anisotropy of Alnico 5. Part I*

R. D. HEIDENREICH AND E. A. NESBITT
Bell Telephone Laboratories, Murray Hill, New Jersey

(Received December 17, 1951)

It is concluded from electron metallographic results that the high coercive force and anisotropy of Alnico 5 are caused by a very finely divided precipitate produced by the permanent magnet heat treatment. This precipitate is a transition structure rich in cobalt and is face-centered cubic with $a_0 = 10$A and appears as rods growing along the [100] directions of the matrix crystal when no magnetic field is applied during heat treatment. The size of the precipitate rods at optimum properties is approximately 75–100A by 400A long. The spacing between rows of rods is about 200A. The rods are not distinctly resolved in the electron images unless they are grown by aging at 800°C. Their orientation and structure is clearly evident in the electron diffraction patterns at all stages of growth. The precipitate responds to a magnetic field applied during heat-treatment both by suppression of nuclei making an angle greater than about 70° with the field and by the forcing of the rods off the [100] direction into that of the field. The precipitate rods tend to scatter in direction about the field vector when the field is off the [100] but are aligned accurately when the field is along [100].

INTRODUCTION

THE term "electron metallography" as used here refers to the combined electron microscope and electron diffraction results of a structural investigation of metals and alloys. These two instruments offer a high resolution technique of studying structures of a size below that at which x-ray diffraction and light microscopy are effective. They are particularly suitable in cases where an alloy exhibits only a very small amount of a precipitated second phase or where that phase is highly dispersed with a small crystal and a small particle size.

Although a considerable amount of x-ray and light microscopic work concerning Alnico 5 has appeared in the literature[1–3] the question of structural changes during heat treatment which greatly affect the magnetic properties has not been answered. Theoretical consideration[4] of the magnetic properties has led to a model of Alnico 5, the most significant feature of which is a fine, oriented precipitate having a high Curie temperature (above 800°C). This precipitate must possess magnetic

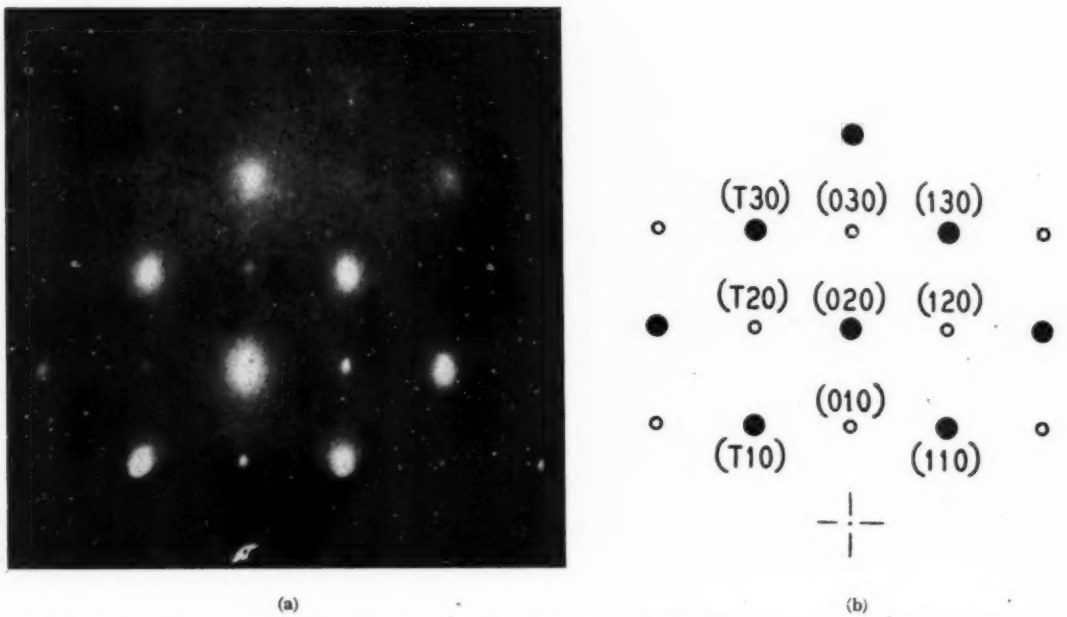

FIG. 1. Reflection electron diffraction pattern from a slowly cooled Alnico 5 single crystal. (100) face and beam along [100] direction. The sketch (b) illustrates the indexing of the B.C.C. spots (heavy) and the superlattice reflections (open circles). The Alnico 5 matrix is generally ordered.

* An abstract of this paper was presented at the American Physical Society Meeting, Schenectady, New York, June 14, 1951.

[1] W. Jellinghaus, Arch. Eisenhüttenw. **16**, 247–51 (1943).
[2] A. H. Geisler, Elec. Eng. **69**, 37–44 (1950).
[3] A. H. Geisler, Trans. Am. Soc. Metals **43**, 70–104 (1951).
[4] Kittel, Nesbitt, and Shockley, Phys. Rev. **77**, 839 (1950). See also the earlier references in reference 4 of Part II.

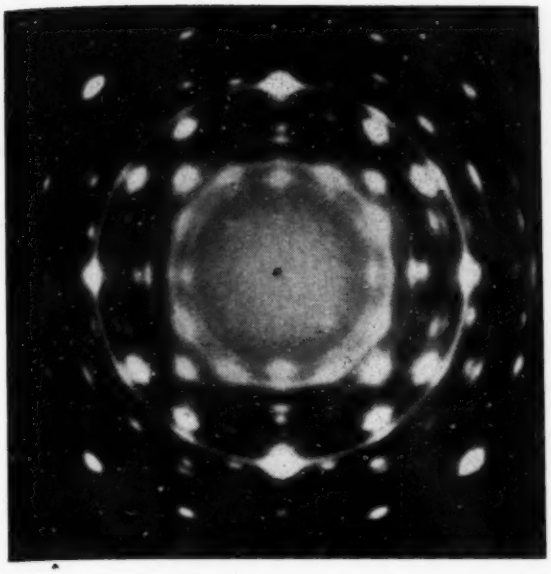

FIG. 2. Transmission electron diffraction pattern from a thermal oxide replica of an Alnico 5 (100) face. The structure of the oxide is cubic spinel with $a_0 \simeq 8.3$Å and a crystal size of about 100 A. The composition is probably based on $CoO \cdot Fe_2O_3$.

properties such that its nucleation in the matrix crystal can be influenced by a magnetic field applied during heat treatment. It is the purpose of this paper to present direct evidence for the existence of such a precipitate, and to demonstrate the correlation between the general texture of the precipitate and magnetic properties such as coercive force and easy direction of magnetization.

At this stage of the investigation, the composition of the precipitate is not known. It is hoped that further work will clarify its composition and elucidate more detail concerning its formation and relation to the matrix crystal.

I. EXPERIMENTAL TECHNIQUE

The alloys used in this investigation were prepared by D. H. Wenny of the Metallurgical Department of Bell Telephone Laboratories and gave the following approximate composition:

Ni.....14 percent	Cu..... 3 percent
Al..... 8 percent	Fe.....51 percent
Co.....24 percent	

Single crystals were desired for this work; the growing of these crystals is described in Part II. The orientations of selected grains were determined from Laue photographs and disks about 1.5 cm in diameter and 1–2 mm thick cut from the grains to produce single crystal disks, the face being generally a (100) or (110) plane, depending upon which was desired. Alnico 5 is quite brittle and usually exhibits [100] cleavage cracks after heat treatment, and this greatly simplifies the problem of orienting the sample during experiments. These cracks served as internal markers in light and electron

FIG. 3. Light micrographs (a) 150× and (b) 2000× and (c) electron micrograph 5400× of (100) face of slowly cooled Alnico 5 crystal showing "spikes" or "puddles."

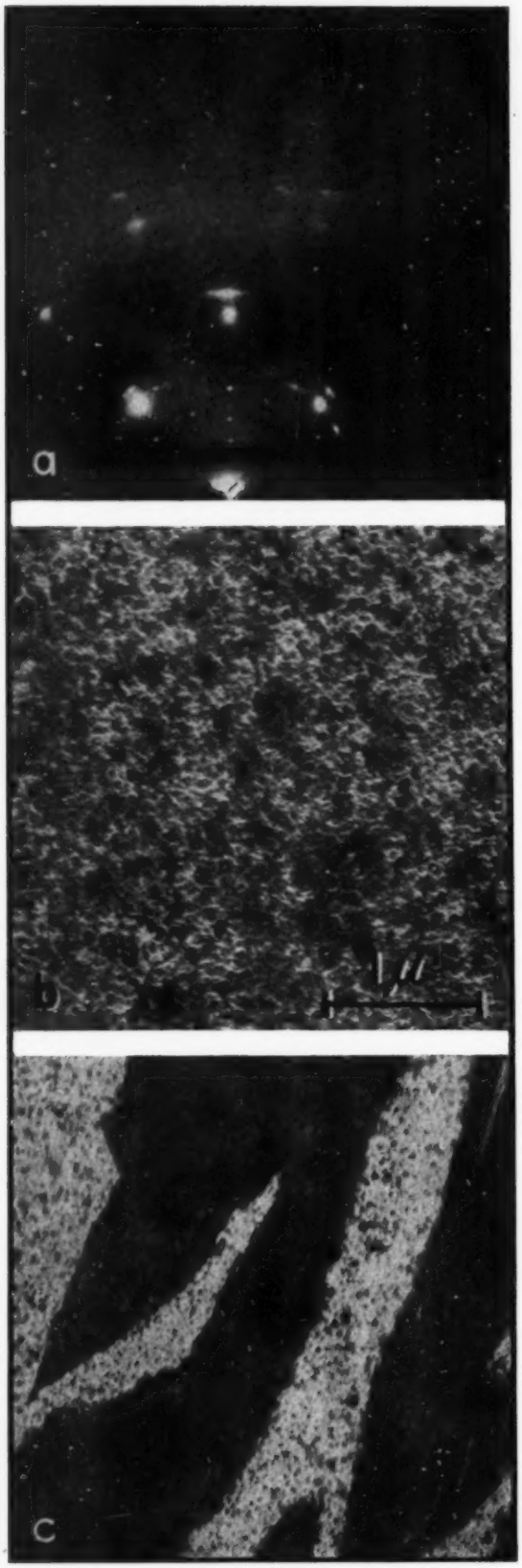

FIG. 4. Single crystal (100) face cooled from 1300°C at about 3°C/sec (permanent magnet heat treatment). (a) Electron diffraction pattern. Beam along [100]. Compare with Fig. 1. (b) Electron micrograph showing characteristic granularity. (c) Electron micrograph showing granularity in puddles.

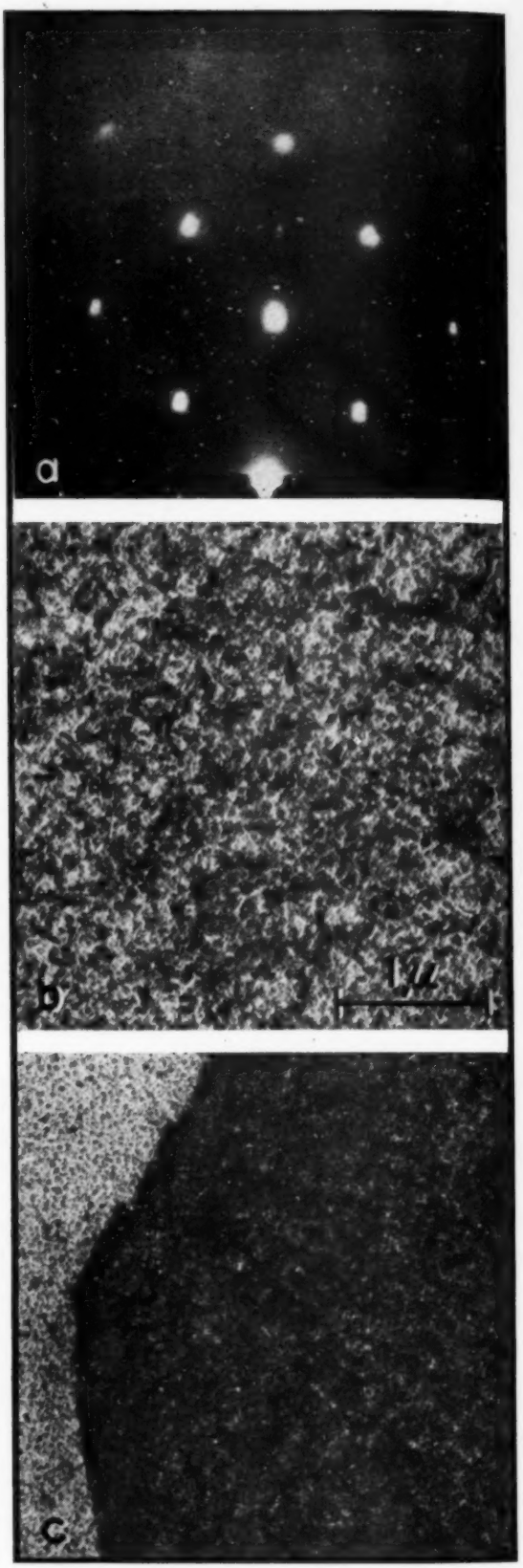

FIG. 5. Same crystal as Fig. 4 aged 8 hr at 590°C. Compare with Fig. 4. The diffraction pattern is now sharp and the spots for the permanent magnet precipitate clearly visible. The granularity in both the matrix and the puddles is more pronounced.

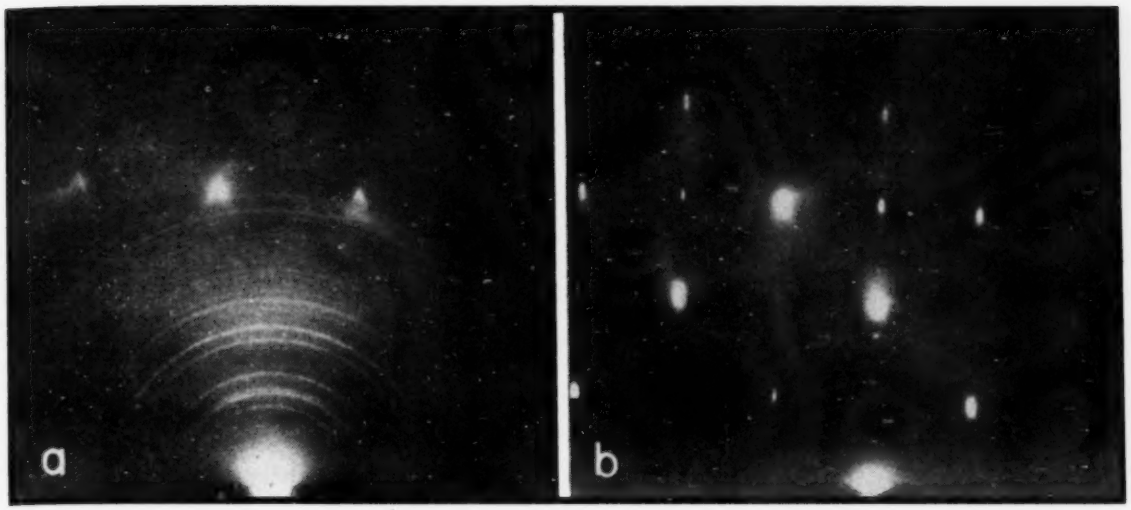

FIG. 6. Electron diffraction patterns from an Alnico 5 crystal oil quenched from 1300°C. (100) face, beam along [100]. The rings are for the randomly oriented permanent magnet precipitate and are strong in (a). A small change in the setting of the crystal produces the matrix B.C.C. spots and superstructure lines of (b).

micrographs and made the orientation of the crystal immediately evident.

The electron microscopic and electron diffraction results were obtained entirely from the prepared surface of the crystal. Consequently, it was essential to discover a preparation which would yield a surface free from tarnish and corrosion films as well as deformation resulting from mechanical polishing, with the precipitated phases standing in relief.[5] The procedure finally adopted as a standard preparation for the electron metallography of Alnico 5 is as follows:

1. Abrade on #0 carborundum polishing paper.
2. Electropolish for about 1 minute at 30 volts in an electrolyte consisting of 75-cc glacial acetic acid, 24-cc perchloric acid, and 2–3-cc of distilled water. The cathode is aluminum with about ten times the area of the disk being polished. The specimen is plunged into a stream of running water upon removal from the polishing bath.
3. The specimen is rinsed in methanol to remove the water and then etched 10 sec in a mixture containing 44-cc methanol, 5-cc concentrated HCl, and 1-cc liquid bromine.
4. From the etchant, the specimen is rinsed first in methanol and then acetone and blotted on a clean filter paper. This surface is then ready for electron diffraction and the preparation of a replica for electron microscopy.

The bromine etch was employed because it stops contact plating onto the surface of any of the elements present in the alloy (particularly copper) and produces a clean surface with the precipitate left standing in relief.

[5] Heidenreich, Sturkey, and Woods, J. Appl. Phys. **17**, 127 (1946).

The electron diffraction patterns were taken with a simple camera employing no lenses but using a biased electron gun and a slit system to produce a well-collimated beam. The specimen to plate distance is 400 mm and exposure times are of the order of 1–3 seconds. The camera constant is $L\lambda = 24$ mmA using 40-KV electrons with $\lambda = 0.06$A. The crystal disks were oriented in the holder with a simple zone axis such as [100] or [110] in the direction of the electron beam. As mentioned, the problem of orientation was greatly simplified by the [100] cleavage cracks nearly always present. Alnico 5 is body-centered cubic with $\alpha_0 = 2.86$A. The general accuracy of electron diffraction measurements is at best only about 1.5 percent with the result that lattice parameters cannot be determined with anything like the accuracy possible using x-rays. Hence, changes in lattice constant caused by variations in composition such as might occur during precipitation cannot be detected in most cases. Since an electron diffraction pattern closely approximates a plane section through the reciprocal lattice, it follows that the B.C.C. Alnico 5 crystal will give rise to a F.C.C. array of spots in the diffraction pattern. Such a pattern is illustrated in Fig. 1(a), which was taken with the electron beam along [001] of a crystal cut with a (100) surface. This crystal was slow cooled from the melt, and the diffraction pattern shows only the B.C.C. phase and from a diffraction standpoint is a single crystal. The intense Laue spots are those to be expected while the less intense spots are superlattice reflections indicating that the alloy is ordered, and the structure factors for other cubic reflections are not zero. Figure 1(b) is a sketch of Fig. 1(a) with the array of spots indexed. The sum of the indices for a superlattice reflection is odd while for a B.C.C. spot the sum is even.

After obtaining the electron diffraction pattern of a

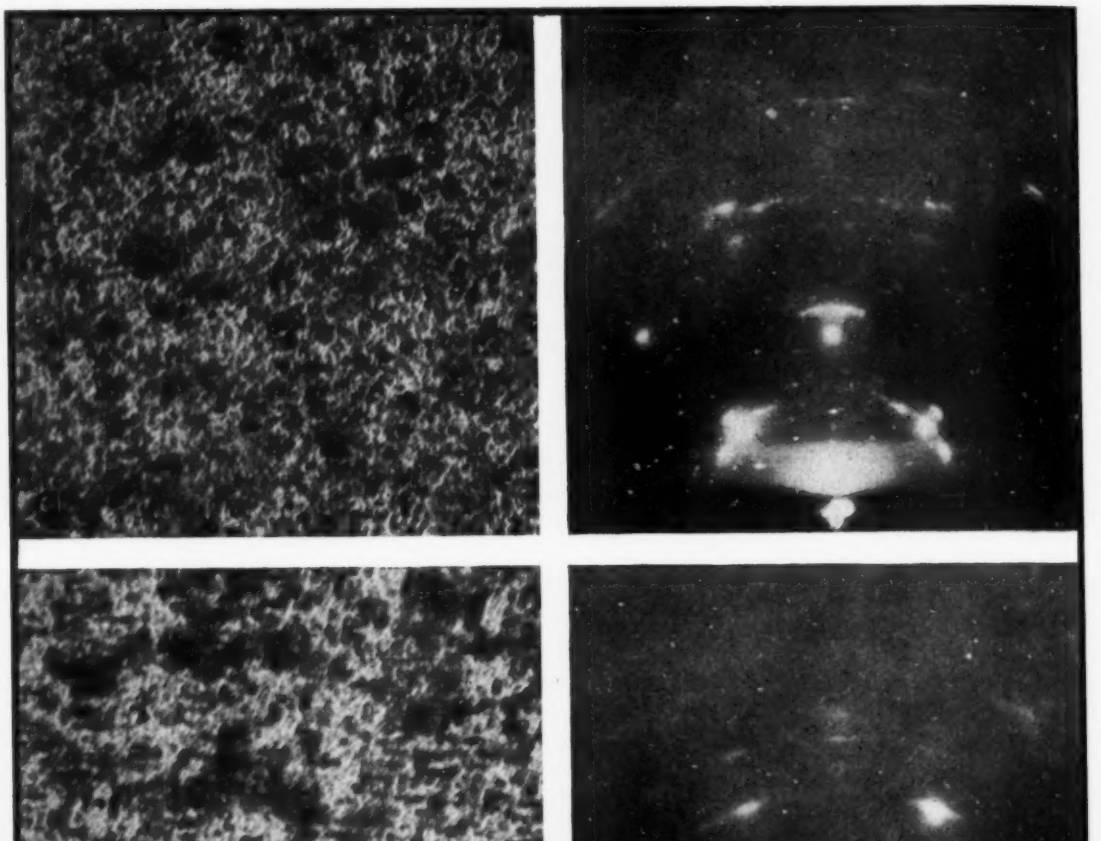

FIGS. 7(a)–7(c). (Caption on next page.)

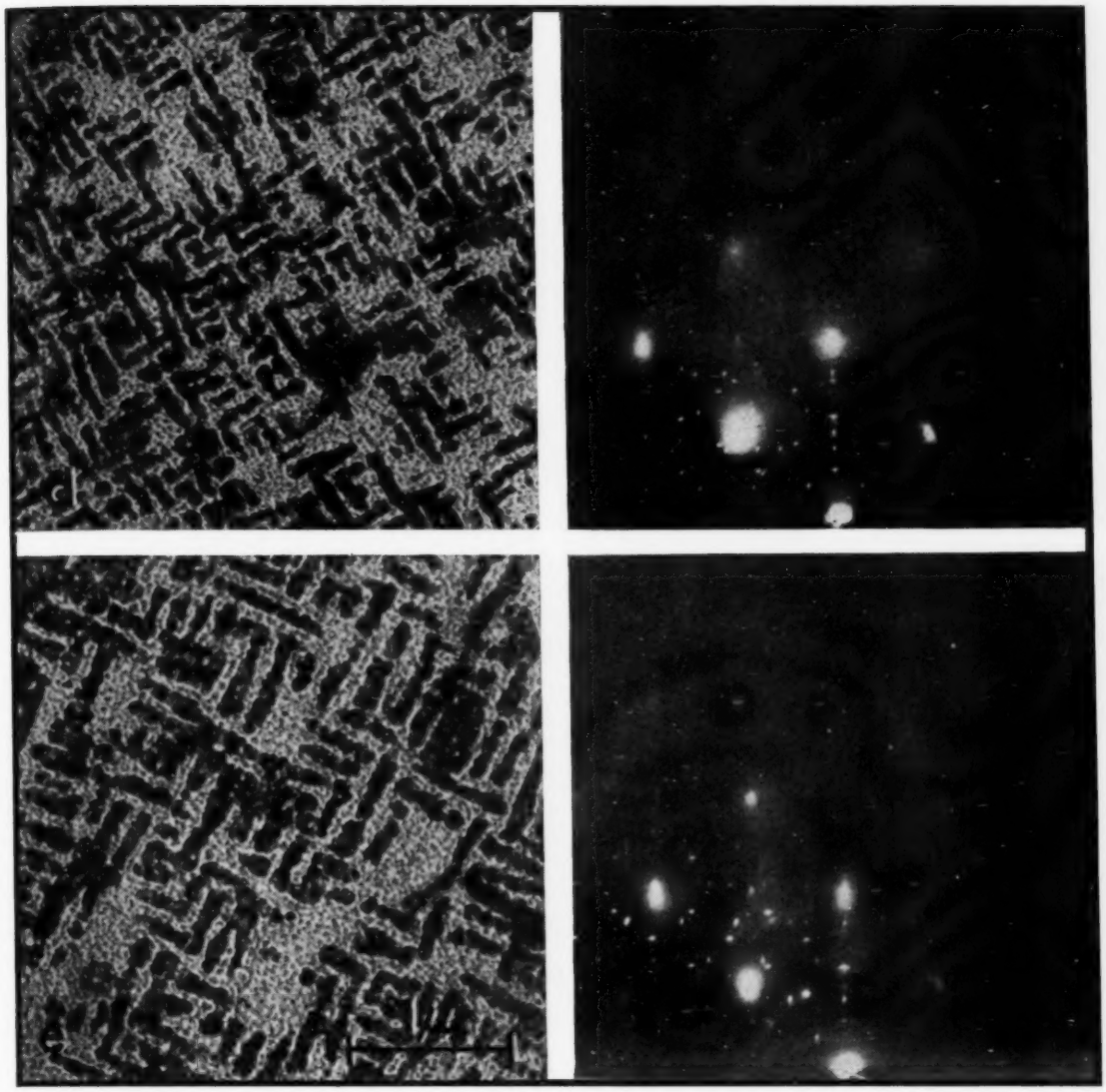

FIGS. 7(d)–(e).

FIG. 7. Sequence of electron diffraction pattern and micrographs showing growth of Widmanstätten permanent magnet precipitate at 800°C. (100) crystal face and beam along [100]. The sharpening of the B.C.C. spots and development of the precipitate is to be noted. (a) Cooled 2°C/sec from 1300°C. (b) Plus 10 min 800°C. (c) 20 min 800°C. (d) 60 min 800°C. (e) 120 min 800°C.

crystal, a replica was prepared for electron microscopy. At the beginning of this investigation a survey of the various replication techniques was undertaken in order to determine which one was the best for this particular purpose. Among those tried were stripped plastic lacquer films, shadow-cast replicas and polystyrene-silica replicas. It was soon evident, however, that the replica best suited for the study of Alnico 5 was the thermal oxide replica prepared by the method of Mahla and Nielsen.[6] The oxide replicas from Alnico 5 are more than simply topographical reproductions of the etched surface. This is because of differential oxidation rates resulting from local variations in concentration of one or more alloying elements. The structural detail seen in these replicas is the same from an electropolished surface as from an etched surface. The electron diffraction patterns are quite different, the electropolished surface being very smooth with no second phase standing in relief. The method of preparation of the thermal oxide replicas is as follows and is nearly identical with that described by Mahla and Nielsen.

1. The electropolished and etched specimen is immersed for 10–20 sec in a molten bath of 1:1 KNO_3–$NaNO_3$ at 500°C to produce a golden oxide film. The actual time of oxidation is judged from the color and appearance of the surface. A film about 150A thick is desirable.

2. After the specimen has cooled, it is rinsed in water to remove the adhering salts, which are water soluble, and then rinsed in methanol.

[6] E. M. Mahla and H. A. Nielsen, J. Appl. Phys. **19**, 378 (1948).

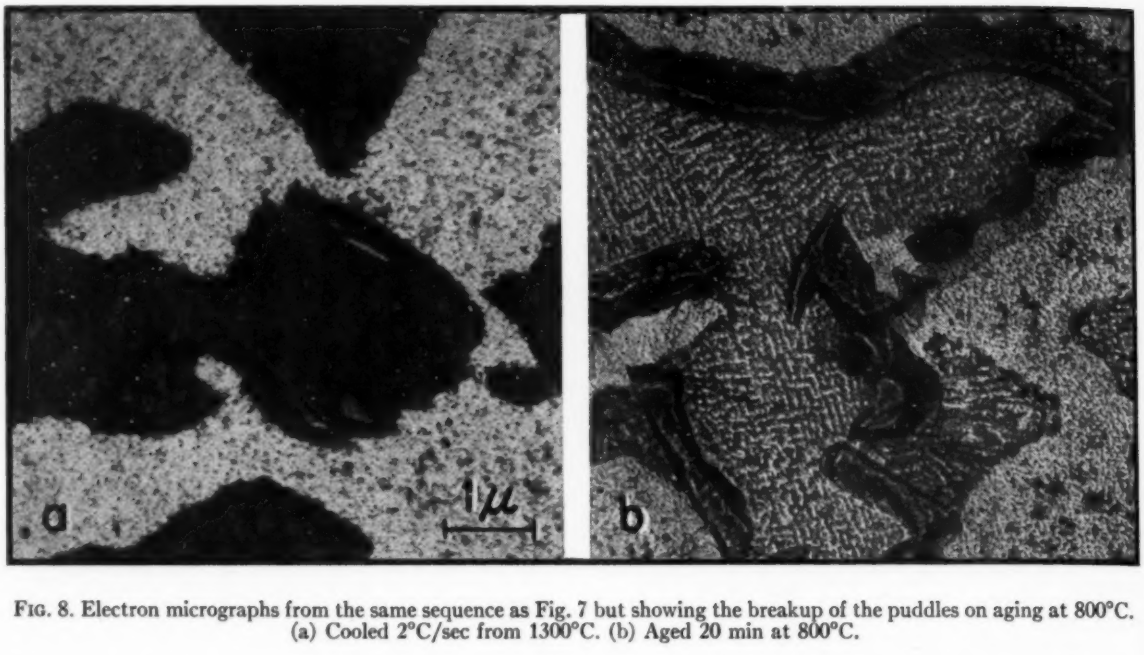

FIG. 8. Electron micrographs from the same sequence as Fig. 7 but showing the breakup of the puddles on aging at 800°C. (a) Cooled 2°C/sec from 1300°C. (b) Aged 20 min at 800°C.

3. The sides of the specimen are cleaned with fine emery paper to remove the oxide, and the surface to be studied is scribed into $\frac{1}{8}$-in. squares using a sharp needle.

4. The crystal with scribed oxide film is next placed in a solution consisting of about 47-cc methanol and 3-cc liquid bromine. In a few minutes the oxide film squares are released from the surface and are transferred to fresh methanol for washing. The squares are then caught on the standard 200 mesh, $\frac{1}{8}$-in. diameter electron microscope specimen screen and are ready for examination.

The electron micrographs were all taken with the RCA EMU using 50-KV electrons and a 0.004-in. platinum objective aperture.

The interpretation of the electron micrographs of the thermal oxide replicas is of prime importance and rests upon the following facts:

(a) Transmission electron diffraction patterns of the oxide replicas show that the film is crystalline with a crystal size below 100A. The structure is spinel cubic with a_0 about 8.3A. The best fit is $CoO \cdot Fe_2O_3$, but considerable variation in composition and substitution of other metallic elements can occur in the spinels to produce changes in the lattice constant. The film exhibits a highly preferred orientation with the spinel (100) tending to lie parallel to the Alnico 5 (100), and the spinel [100] tending to lie along the Alnico 5 [100]. Figure 2 illustrates the appearance of the electron transmission pattern from a replica of a (100) Alnico 5 face.

(b) It has been observed in iron-cobalt alloys that cobalt tends to oxidize more rapidly than the iron.

(c) The time required to produce a golden oxide replica on Fe_2NiAl is about 30 times that required for Alnico 5.

The conclusion is that the cobalt greatly accelerates the rate of oxidation so that cobalt rich regions in the alloy will produce correspondingly thicker local regions of oxide. Hence, the replica is to a first approximation a tracer map for cobalt concentration.

Since the replica film is crystalline, Bragg reflections occur and some granularity in the electron image due to the crystallinity is to be expected. As will be seen, however, this is a second-order effect and does not seriously complicate the interpretation of structures exceeding the film thickness. The oxide replicas are thus useful in studying structures down to about 200A, and cobalt segregations or concentration variations over a distance of 200–500A should be observable in the replicas.

The slowly cooled Alnico 5 crystal from which the diffraction pattern of Fig. 1 was obtained exhibits a great deal of structure in the light microscope when prepared by the standard procedure already discussed. Figure 3(a) is a low magnification light micrograph of the surface that yielded Fig. 1. This structure consists of "spikes" and smaller regions of random shape which are referred to as "puddles." They are not a second

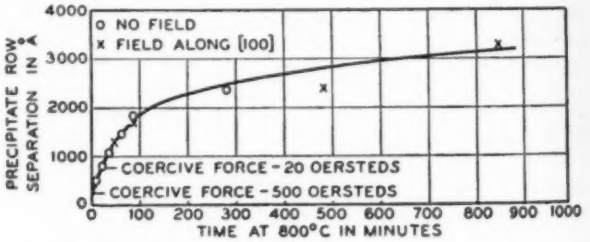

FIG. 9. Plot of average distance between precipitate rows vs time at 800°C. The spacing in condition of maximum coercive force is obtained by extrapolating to zero time to yield a value of about 200A.

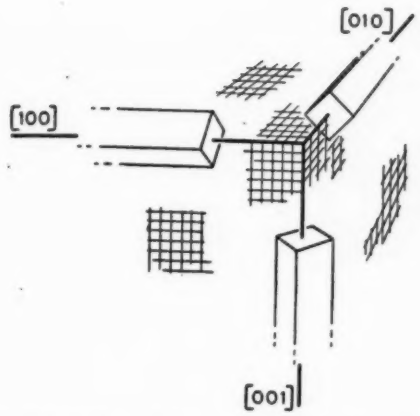

FIG. 10. Orientation of permanent magnet precipitate rods along three [100] directions in Alnico 5 crystal. The precipitate is a transition structure which is F.C.C. with $a_0 = 10A$. The match is [100] ppt. along [100] matrix and (110) ppt. parallel to (100) matrix with 2 cells of precipitate to 7 cells of matrix.

phase in the ordinary sense since their structure is B.C.C., and they are coherent with the matrix. The x-ray patterns from this crystal indicate a single crystal with superlattice in agreement with Fig. 1. The conclusion is thus that the puddles are due either to a change in composition relative to the matrix or that they exhibit a different degree of atomic ordering. (This is to account for the differential etching.) The structure of the spikes seen in Fig. 3(a) is shown in more detail in Fig. 3(b) which is a high magnification light image. It is seen that the spikes consist of a main central region and a fringe or edge which has etched differently. An electron micrograph of the thermal oxide replica is seen in Fig. 3(c). The spikes or puddles are dark because the film is thicker, and the fringe at the edge is very much in evidence. The light and electron images are thus in agreement. It follows from the discussion of the interpretation of the oxide replica that the puddles of Fig.

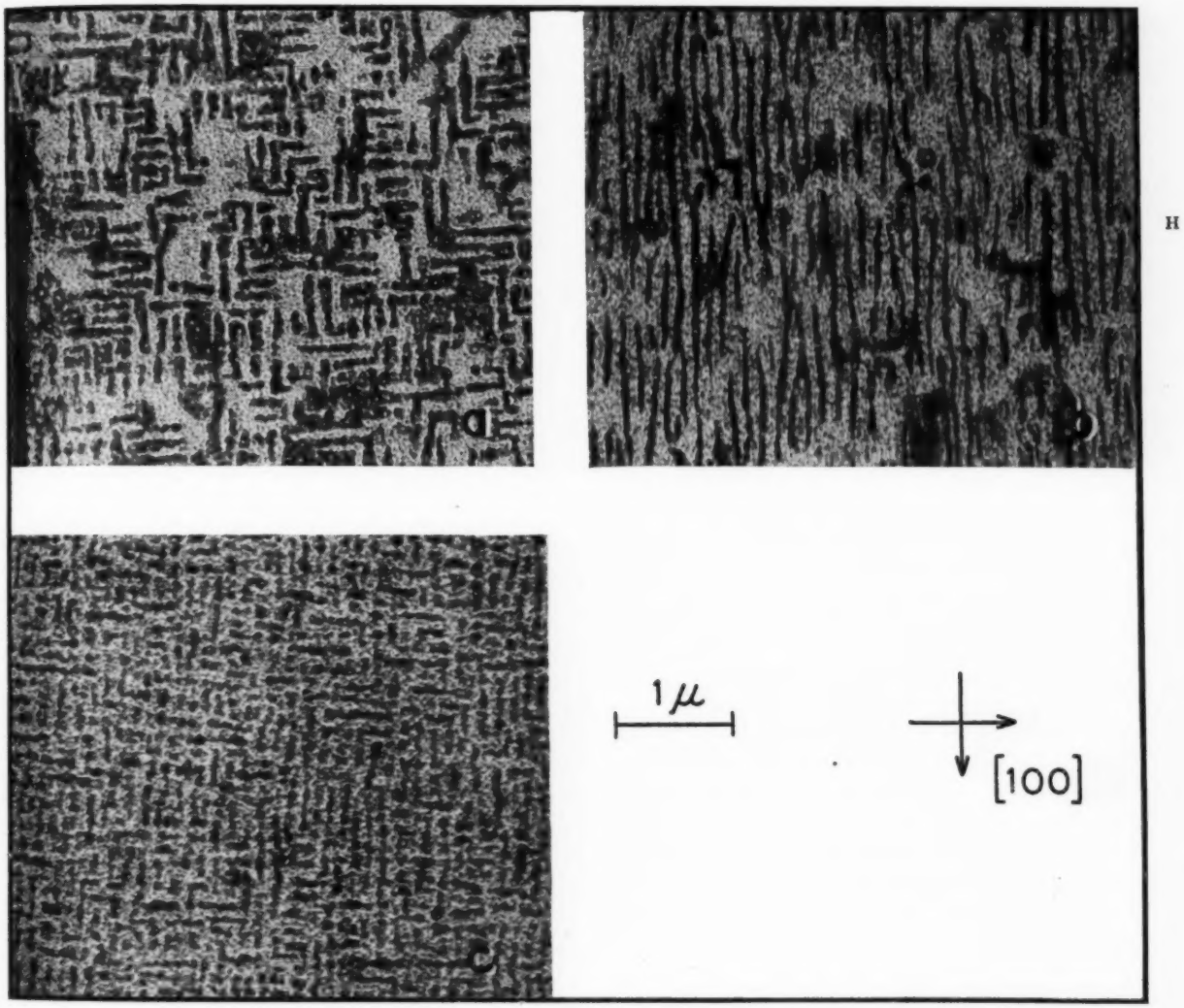

FIG. 11. Effect of a magnetic field applied during the 2°C/sec cool from 1300°C on the permanent magnet precipitate in Alnico 5. Single crystal, (100) face. Aged 2 hr at 800°C to grow the precipitate. (a) Cooled 2°C/sec from 1300°C with no field. (b) Cooled 2°C/sec from 1300°C with field along [100]. (c) Section normal to applied field showing rod shape of precipitate with rods lying along H.

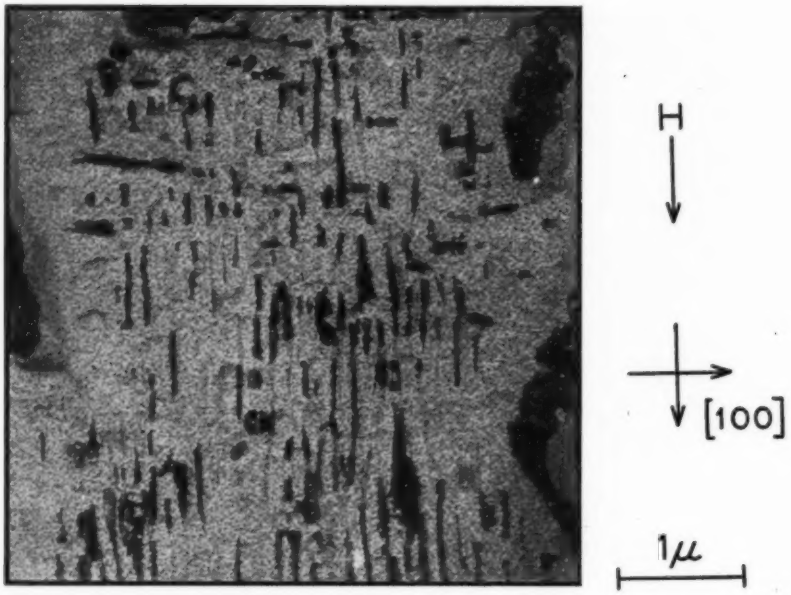

FIG. 12. Same as Fig. 11(b), but showing a region surrounded by puddles which have impoverished the adjacent matrix. The change in composition in this area has reduced the sensitivity to field heat treatment.

3(c) are richer in cobalt than the matrix, because the film is thicker in this region. It cannot be said that the puddles also exhibit order and the matrix disorder or vice versa. However, it can be speculated that the puddles are due to a segregation of cobalt atoms in these regions to produce a cobalt-rich lattice which may be energetically favored by the formation of a superlattice. It would not be surprising if this were the case, but it is yet to be proved. The granular appearance of the matrix in Fig. 3(c) is not caused by the film structure itself but reflects a state of segregation in the alloy as will be seen by comparison with images to be presented later.

II. STRUCTURE AND HEAT TREATMENT

The general effect of heat treatment on the electron metallography of Alnico 5 is of interest here only insofar as it has a direct bearing on the interpretation of heat treatment leading to desirable magnetic properties. The commercial heat treatment of Alnico 5 is not isothermal but requires a cooling rate of from 2–4°C/sec from about 1300°C down to below 600°C. Hence, the effect of cooling rate on the microstructure is of primary importance in the first stage of this investigation. The easy directions of magnetization, coercive force, etc., will be discussed in the second part of this paper dealing with magnetic properties.

The single crystal disks cooled from 1300°C at rates in the region of 2–4°C/sec and with no magnetic field exhibit microstructure with the following characteristics:

1. The "spikes" and puddles illustrated in the micrographs of Fig. 3 may or may not be present depending upon the cooling rate in the higher temperature range. The rate above 900°C seems to be the controlling factor. Accelerated cooling above 900°C reduces the amount of puddles.

2. The electron diffraction patterns exhibit arrays of spots for a new phase, which is always found in the material that has been given the permanent magnet heat treatment, whether or not puddles are present. The Bragg spots for the B.C.C. structure are often not as sharp as seen in Fig. 1 but may exhibit arcing indicating that various portions of the crystal are not oriented exactly the same. Short arced rings for a structure not yet understood are also seen. This structure appears to be B.C.C. with $a_0 \sim 3.0$A.

3. The electron micrographs of the thermal oxide replica show a characteristic granularity suggesting a precipitated phase too highly dispersed to be distinctly resolved.

4. Light-microscopic and x-ray results cannot differentiate between samples cooled at a rate of 2–4°C/sec and those cooled much more slowly. The precipitate mentioned in (2) has not been detected by either light microscopy or monochromatic x-ray diffraction patterns.

Figure 4(a) illustrates the electron diffraction patterns obtained with the permanent magnet heat treatment on an Alnico 5 single crystal with a (100) face and the beam along [001]. The new array of spots and the arced spots mentioned in (2) as well as the usual B.C.C. spots are evident on comparison with Fig. 1. Figures 4(b) and 4(c) show the electron micrographs of this same sample and illustrate both the granularity and the large puddles.

The coercive force of 200–300 oersteds obtained from the treatment of Fig. 4 can be raised to 500 oersteds by aging the crystal 8 hours at 600°C. The structural effect of this aging is to sharpen the B.C.C. spots and develop the new precipitate[7] array of spots as shown in Fig. 5(a).

[7] This precipitate will be referred to as the "permanent magnet precipitate." That it is responsible for the properties of Alnico 5 will be demonstrated in the discussion of the effect of a magnetic field during heat treatment.

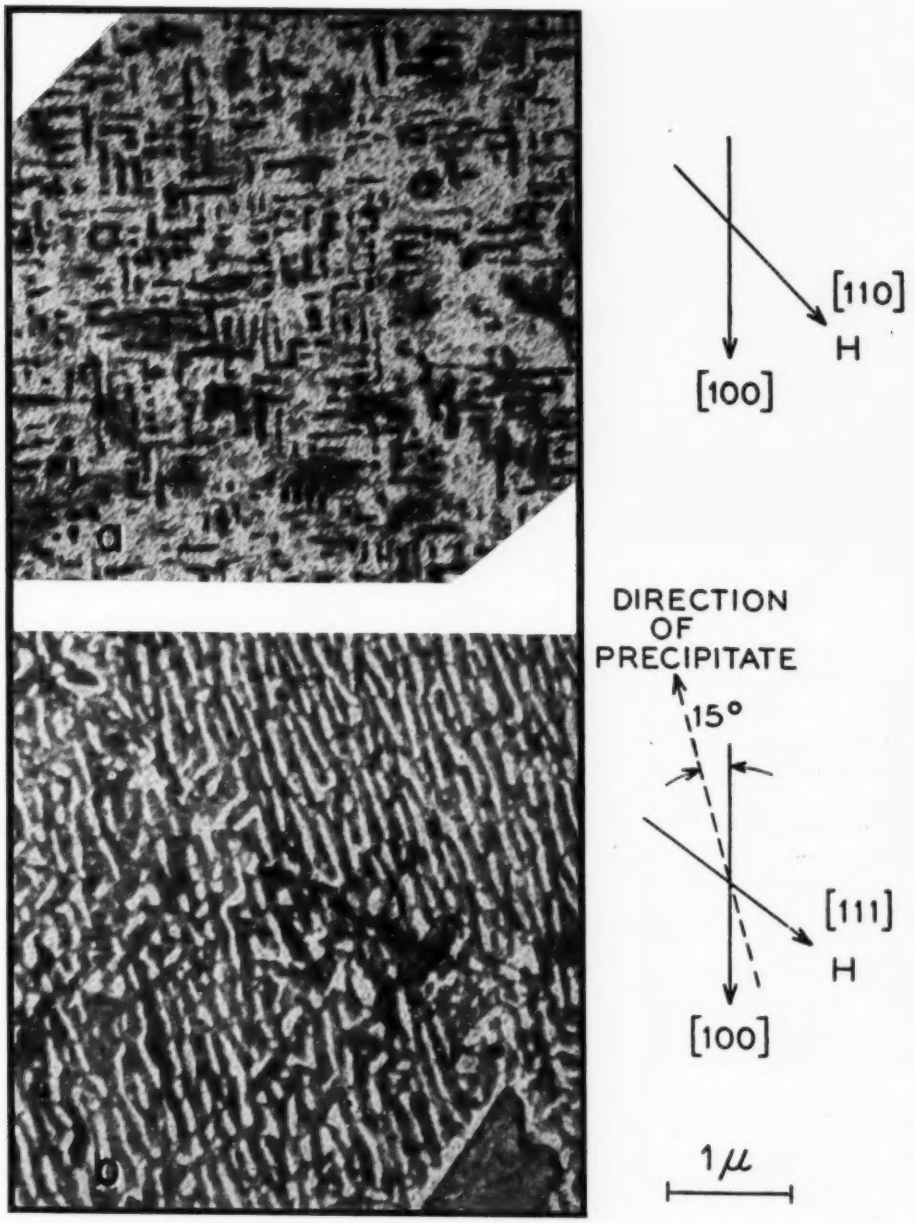

FIG. 13. Alnico 5 single crystals heat treated with magnetic field along directions different than [100]. Aged at 800°C to grow precipitate already nucleated. (a) (100) face. Field along [110]. (b) (110) face. Field along [111].

The granularity seen in the replica is likewise enhanced as shown in Fig. 5(b). The granularity in the puddles is even stronger than in the matrix as seen in Fig. 5(c). In general, the puddles (when present) seem to age more rapidly than the matrix as judged from the electron micrographs. It appears from Fig. 5 that the 600°C aging aids the development of the permanent magnet precipitate and also "heals" or brings about realignment within the crystal.

The electron diffraction pattern of Fig. 5(a) requires that the permanent magnet precipitate giving rise to the array of new spots be accurately aligned with the matrix crystal. The degree of alignment can be greatly reduced if the cooling rate is increased. Thus, a crystal given an oil quench from 1300°C yields the electron diffraction pattern seen in Fig. 6. Figure 6(a) shows a ring pattern for the permanent magnet precipitate indicating a random orientation of crystallites. Figure 6(b) is the same crystal but with the angle of grazing set to yield a strong pattern for the matrix crystal. The B.C.C. spots are not arced in this crystal (compare with Fig. 4) and the superlattice reflections are very strong. No puddles are found in the quenched specimens.

Electron diffraction patterns for the permanent magnet precipitate are obtained over a range of cooling rates from an oil quench to a slow air cool. A crystal water-quenched from 1300°C does not show any precipitate in contrast to the oil quench. The very slow cool from the melt does not yield a precipitate pattern as was seen in Fig. 1. The present evidence points to the permanent magnet precipitate obtained with the

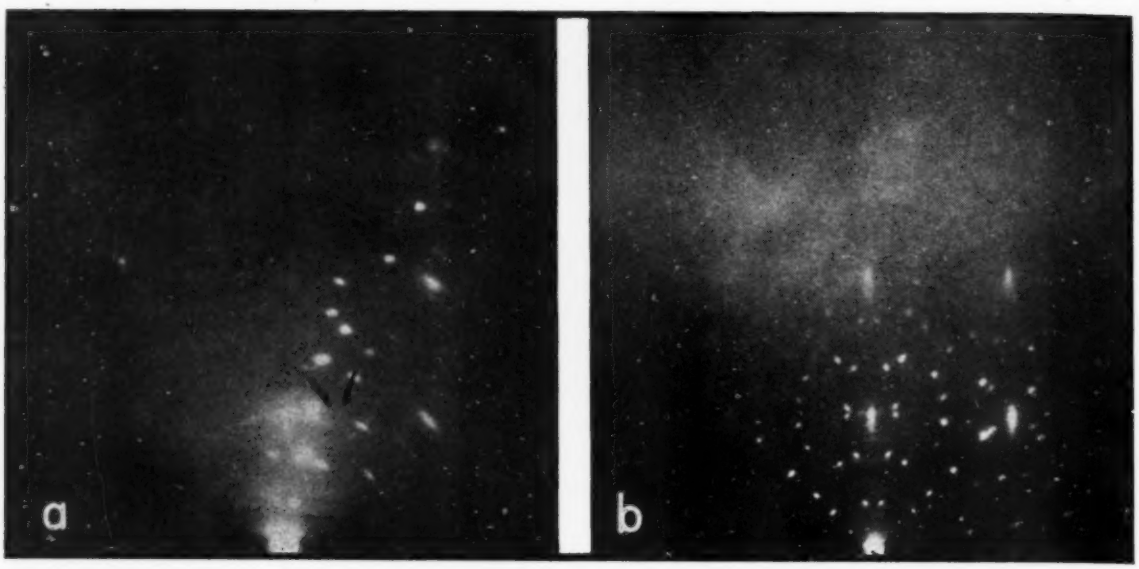

FIG. 14. Effect of 800°C aging on single crystal with (110) face, heat treated with magnetic field approximately normal to surface. Electron beam along [100]. (a) Cooled 2°C/sec from 1300°C. (b) Aged ½ hr at 800°C.

commercial cooling rate as being a transition lattice rather than a thermodynamically stable phase.

Experiments show that the permanent magnet precipitate is nucleated at about 820°C. The usual treatment does not allow time for much growth to occur and hence experiments to study the growth of the precipitate were undertaken. It was found that a Widmanstätten structure could be grown by heat treatment at 800°C but not below. Geisler[8] has recently demonstrated a Widmanstätten precipitate in Alnico 5 of sufficient size to be visible in a light microscope by aging 300 hours at 800°C. The same structure can be seen in the replicas at a much earlier stage requiring only 15–30 minutes at 800°C following the permanent magnet heat treatment.

The growth of the precipitate at 800°C to make it distinctly visible in the electron microscope is very important in the investigation of the effect of a magnetic field during heat treatment. Therefore, it is worth while to show in detail the electron metallography of the growth at 800°C. The starting point is an Alnico 5 single crystal with a (100) face, for which the heat treatment consisted of cooling from 1300°C at 2–3°C/sec with no magnetic field. The 800°C heat treatments were done in a small furnace with an air atmosphere. At the end of the prescribed time at 800°C, the crystal was quenched in water and then prepared for electron diffraction, and a replica made. The results obtained as a function of time of heat treatment at 800°C are illustrated in Fig. 7. The following conclusions are drawn from this sequence:

(1) The permanent magnet precipitate can be grown at 800°C without significant change in crystal structure for times of the order of an hour or two. Two hundred hours at 800°C convert the precipitate to B.C.C.

(2) The Widmanstätten pattern is first seen in the electron micrographs after 10–15 minutes aging at 800°C.

(3) The precipitate is apparently in the form of rods oriented with the long axis in the [100] directions of the matrix. The rods tend to group into plate-like rows.

(4) The lattice of the precipitate accurately maintains its orientation relative to the matrix.

(5) The originally arced B.C.C. spots become sharper as the aging proceeds and this indicates a healing of the spread in orientations in the matrix or between the matrix and the puddles.

(6) The internal break-up of the puddles by the 800°C aging, as shown in Fig. 8, indicates that they are unstable as formed by the initial cooling rate.

(7) The greatly reduced amount of Widmanstätten in the regions about the puddles indicates that in these regions the puddles have impoverished the matrix of an element or elements necessary to the formation of the precipitate.

(8) The fact that the precipitate oxidizes more rapidly than the matrix is presently taken as evidence that the permanent magnet precipitate is rich in cobalt. The puddles are probably also cobalt rich.

The effect of 800°C aging on the slowly cooled crystal of Figs. 1 and 3 is quite different. No Widmanstätten precipitate appears and the diffraction patterns remain as shown in Fig. 1.

A quantity of interest in the theory of the magnetic properties of Alnico 5 is the average separation of the precipitate rods, which tend to form in plates. Although the general size of the granular detail produced by the permanent magnet heat treatment is no more than a few hundred angstroms, no definite distances can be measured in the images. An extrapolated value of the

[8] A. H. Geisler, Phys. Rev. 81, 478 (1951).

spacing can be obtained from the 800°C heat treatments. Measurements of separation between rows from a series (from which Fig. 7 was taken) ranging from 10 minutes to 14 hours at 800°C are plotted in Fig. 9. The average separation of precipitate rows lying along a single [100] direction, determined by extrapolating Fig. 9 to zero time, is about 200A. The electron diffraction patterns indicate that the crystal size of the precipitate is 75–100A, so that the actual distance in the matrix between precipitate rows is of the order of 125A. The size of a precipitate rod in the permanent magnet state is estimated to be not less than 75×75 ×400A. This value is only an approximation but is consistent with the fact that the precipitate particles are not actually resolved in the electron micrograph of crystals having maximum coercive force.

The 800°C heat treatment is very useful in enlarging the precipitate. However, since ten minutes at 800°C is sufficient to reduce the coercive force from 500 oersteds to 25 or less, the magnetic properties after aging at 800°C are not of much interest. The effect on the easy direction of magnetization will be mentioned later.

III. CRYSTAL STRUCTURE OF THE PERMANENT MAGNET PRECIPITATE

The crystal structure of the permanent magnet precipitate is not known in detail. Some general features of the structure and the orientation relative to the matrix can be readily determined from the electron diffraction patterns. Since this precipitate gives evidence of being a transition structure rather than a stable phase, it must be borne in mind that there is very likely a continuous change occurring during heat treatment and that patterns taken at various stages may show changes in relative intensities. The accuracy of the electron diffraction results does not allow any positive statements concerning changes in lattice parameters.

Electron diffraction patterns taken from single crystals of Alnico 5 with the permanent magnet heat treatment show that the precipitate is cubic with a large cell. The structure can be indexed as face-centered cubic with $a_0 = 10.0$A. This suggests an arrangement of atoms similar to those of the metal atoms in a spinel such as exhibited by Cu_2Mg. The precipitate tends to form as rods with the [100] direction of the precipitate along the [100] direction of the matrix but rotated 45° about the [100] so that the (100) plane of the matrix matches the (110) plane of the precipitate. This arrangement is sketched in Fig. 10[9]. The electron diffraction patterns show directly that the fit between precipitate and matrix is such that 7 cells of the matrix just match 2 cells of the precipitate. The crystal forces bringing about this match are quite strong and in the absence of a magnetic field it is accurately maintained. Up to this time, the precipitate has not been found in x-ray diffraction patterns, probably on account of the small crystal size.

Further work concerning the crystal structure of the precipitate is being done but the details are not in a state to be reported at this time. Of greater interest in this paper is the effect of a magnetic field applied during heat treatment.

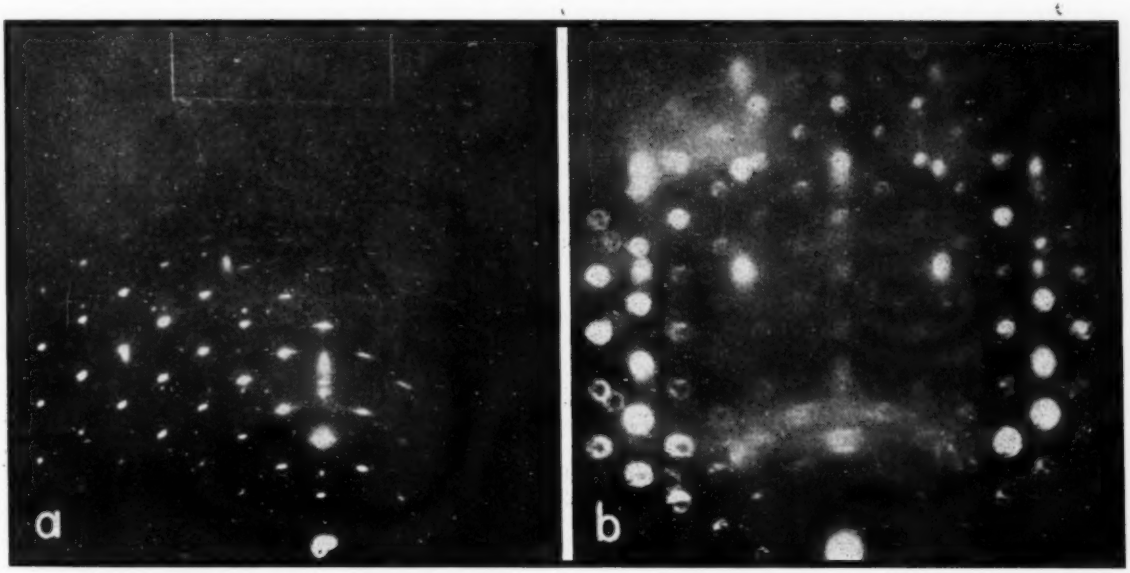

FIG. 15. Strong electron diffraction patterns for the permanent magnet precipitate from crystals aged at 590°C. (100) face and beam along [100] perpendicular to precipitate rods. (a) Aged 24 hr 590°C. (b) Aged 32 hr 590°C but with residual local magnetic fields about precipitate particles.

[9] In Fig. 7(b), *d* and *e* exhibit a double array of precipitate spots consisting of one array as seen in Fig. 7(c) and another identical array at right angles. This would be expected for the electron beam along one of the [100] directions. Interesting patterns are obtained where more than one array of precipitate spots occurs.

IV. EFFECT OF A MAGNETIC FIELD DURING HEAT TREATMENT

One of the outstanding features of Alnico 5 that must be explained by a plausible structure is the great effect produced by a magnetic field applied during treatment. If a single crystal is heat treated by cooling 2°C/sec from 1300°C with a field of several thousand oersteds directed along a [100] direction, the magnetic measurements indicate that a large effect has been produced. It is obvious that if the precipitate discussed in the preceding section is the agent responsible for the behavior of Alnico 5, then a positive effect must be found when the heat treatment is carried out in a magnetic field. That a striking structural effect is produced by the field is illustrated in Fig. 11(b). Figure 11(a) shows a pattern obtained on a (100) face of a single crystal cooled 2°C/sec from 1300°C with no magnetic field and then aged two hours at 800°C to grow the precipitate. The cubic symmetry is obvious. If the same experiment is now repeated but with a magnetic field applied along a [100] parallel to the surface, the result is shown in Fig. 11(b). *The magnetic field has completely suppressed the nucleation of precipitate at right angles to the field.* A section normal to the magnetic field shows the ends of the precipitate rods as seen in Fig. 11(c). This result requires that the magnetic forces on the precipitate nuclei be comparable with the crystal forces. The effect of composition on this ability to heat treat in a magnetic field is demonstrated in Fig. 12 which shows a region surrounded by puddles in this same crystal that yielded Fig. 11(b). The density of precipitate rods is lower than in Fig. 11(b), and it is seen that they also tend to grow across the field. This indicates that the puddles have impoverished the adjacent regions giving a composition not so sensitive to field heat treatment. The importance of the composition of Alnico 5 thus becomes apparent in its effect on the precipitate.

When the direction of the magnetic field during heat treatment no longer coincides with a [100] of the crystal, the situation is much more complicated. The result depends upon the angle between the magnetic field, H, and the [100] direction in the crystal. If this angle is called α, it is known that for $\alpha \approx 90°$, the precipitate nuclei are completely suppressed while for $\alpha = 0$, the nuclei are favored. Experiments in which the value of α was 10°, 45°, and 54° yielded the following conclusions:

(1) For $0 < \alpha < 90°$, the magnetic force acting on the precipitate nuclei tends to force them off the [100] in direct competition with the crystal forces. The result is that the crystal is fragmented and appears to have recrystallized.

(2) The electron diffraction patterns show that the precipitate is no longer in accurate register with the lattice but exhibits a range of orientations. A portion of the precipitate apparently follows the magnetic field but there is a great deal of scatter.

(3) The aging at 800°C removes the fragmentation to produce again a single crystal and allows the crystal forces to take over and at least partially restore the precipitate to [100] directions. The degree to which the realignment of the precipitate occurs, depends upon the angle α. There is some value of α, say α_c, such that for $\alpha > \alpha_c$, no nucleation occurs at all. At present, it can be said only that $70° < \alpha_c \lesssim 90°$.

The electron micrographs of crystals heat-treated with the magnetic field off the [100] directions and aged at 800°C do not show the original direction of the field applied during heat treatment. A crystal heated with $\alpha = 10°$ appears identical with Fig. 11(b) after the 800°C age. For $\alpha = 45°$, the result is shown in Fig. 13(a). The precipitate was nucleated in the two [100] directions and grew there at 800°C. Precipitate formed off the [100] direction vanished during aging where the crystal forces took over. For $\alpha = 54°$, the result is shown in Fig. 13(b). In this case the crystal was prepared with a (110) surface and heat treated with the field along [1$\bar{1}$1]. The precipitate is obviously not confined to the [100] after the 800°C age.

The rearrangements occurring at 800°C because of the crystal forces are demonstrated nicely in the electron diffraction patterns. Figure 14 shows the effect in a crystal with a (110) face heat treated with the field normal to that face, or approximately so. Figure 14 is the pattern obtained after cooling 2°C/sec and shows that the crystal is fragmented and the precipitate not confined to the [100] directions. The preferred orientation evident in Fig. 14(a) may be along the field direction. After ½ hour at 800°C the pattern obtained is seen in Fig. 14(b). The change upon aging is quite striking in Fig. 14(b). The fragmentation has been removed by the 800°C age to produce a single crystal again, and the precipitate now is confined to the [100] directions. The two [100] directions are at 45° to the surface of the specimen and result in an interesting array of precipitate spots. This pattern for the precipitate can be completely accounted for by a 45° superposition of two of the arrays seen in Fig. 4(a) or Fig. 7(c).

The diffraction patterns obtained from crystals heat treated in a magnetic field generally are considerably stronger because of the orientation of the precipitate. Since the precipitate is in the form of rods, only a weak pattern can be expected when the beam is along the rod axis. The strongest patterns occur with the beam normal to the rod axis. Figure 15(a) shows a very strong pattern for the precipitate produced by heat treating with the field along [100] and aging 24 hours at 590°C. The beam is along [100] but perpendicular to the rods.

The crystals must be demagnetized before an electron diffraction pattern can be taken. Even though the specimen is demagnetized to nearly zero average field, electron diffraction patterns indicating the presence of

local magnetic fields are sometimes obtained. These local fields act as poor lenses for the electrons and introduce peculiar deviations. Figure 15(b) illustrates such a case with a strong pattern for the precipitate but with the spots badly distorted or "wormy." It will be noted that the B.C.C. matrix spots are quite normal in Fig. 15(b), hence it is concluded that the local fields are confined to the precipitate particles and only the beams diffracted by those particles show the effect of a magnetic field. This phenomenon again draws attention to the magnet properties of the precipitate.

In brief, the electron metallography can be summarized as follows:

(1) The permanent magnet heat treatment of Alnico 5 produces a fine precipitate in the form of rods about 75×75×400A in size with a tendency to group into plates about 200A apart. This precipitate is crystallographically distinct from the matrix and is tentatively indexed as face-centered cubic with $a_0 = 10$A. The cell size is 7/2 that of the matrix. The precipitate rods tend to form with [100] directions of the precipitate along the [100] directions of the matrix and the (110) planes of the precipitate parallel to (100) planes of the matrix. The precipitate is apparently a transition structure for which both the starting point and final product are B.C.C. The process is not understood in detail and the composition of the precipitate is unknown but is probably cobalt rich.

(2) The precipitate is magnetically active and can be influenced by a field applied during nucleation. Precipitation can be confined to a single [100] direction, by a field along that direction. When the field is not along a [100] direction, fragmentation of the matrix occurs and some of the precipitate is forced off the [100] and tends to follow the field. Whether it follows the field or is suppressed depends upon the angle between the precipitate rod and the field.

As will be seen in the following Part II, this precipitate can account for the general magnetic properties of Alnico 5, and it indicates that the theory which predicted its presence is correct at least in its broader aspects.

The authors are grateful to Mr. K. H. Storks for pertinent suggestions and aid in interpreting the diffraction data and for a number of x-ray diffraction experiments. They also wish to express their appreciation to Mr. F. G. Foster for light optical examination and photomicrographs of a large number of specimens.

Physical Structure and Magnetic Anisotropy of Alnico 5. Part II*

E. A. NESBITT AND R. D. HEIDENREICH
Bell Telephone Laboratories, Murray Hill, New Jersey
(Received December 17, 1951)

As a result of measurements of magnetic anisotropy and coercive force on single crystals of Alnico 5 and the electron metallography of Part I, the following conclusions were obtained. When the crystals are heat treated in a field in the principal crystallographic directions, the easy direction of magnetization is the field direction, and magnetically the crystals have twofold symmetry. However, there is a strong tendency because of crystal forces for the precipitate to grow in ⟨100⟩ directions; and, therefore, the crystal has the highest anisotropy when the heat-treating field and a ⟨100⟩ direction are parallel. The large increase in residual induction of Alnico 5 which results from the magnetic field heat treatment is caused by the easy directions of the crystal changing from the ⟨111⟩ directions to a single easy direction approximately parallel to the field. Domain rotations rather than boundary movements account for the coercive force of the alloy, since the dimensions of the individual particles are approximately 200 angstroms. The present physical picture of the alloy is one of single domains of precipitate material in parallel with single domains of matrix material, the observed coercive force being the resultant of this parallel combination.

INTRODUCTION

THE main purpose of this work has been to test experimentally a current theory of Alnico 5[1] which accounts for some of the alloy's unusual permanent magnet properties. This alloy, containing by weight 8 percent Al, 14 percent Ni, 24 percent Co, 3 percent Cu, and 51 percent Fe, has the unique property that its energy product $(BH)_{max}$ is increased by heat treatment in a magnetic field (H_t) from 1.8×10^6 with $H_t=0$ to 5×10^6 with $H_t=1000$ oersteds. Briefly the theory accounts for the behavior of Alnico 5 in the following manner: Consider a polycrystalline bar of Alnico 5 (Fig. 1) which has been heat treated in a field (H_t) in the direction indicated. According to the theory, plates of precipitate are formed parallel to the field (as shown by the broken lines) but not transverse to it. The result is that the alloy is divided into plates of precipitate and rod-like units of matrix as shown in Fig. 1. The nuclei which are favored for growth are parallel to the field, since in this position their demagnetizing energy is a minimum and the growth of these favored nuclei results in directional precipitation. This theory, in general, has been substantiated by the experimental work of Part I. The presence of the plates of precipitate has been verified, and, in addition, it was found that the plates are approximately 200 angstroms apart and are composed of rows of rods. These dimensions are small enough so that the constituents should behave as single magnetic domains. The problems of accounting for the coercive force and of explaining the magnetic behavior of the alloy were attacked by using the experimental data obtained in Part I, and by making magnetic anisotropy and coercive force measurements on single crystals of Alnico 5.

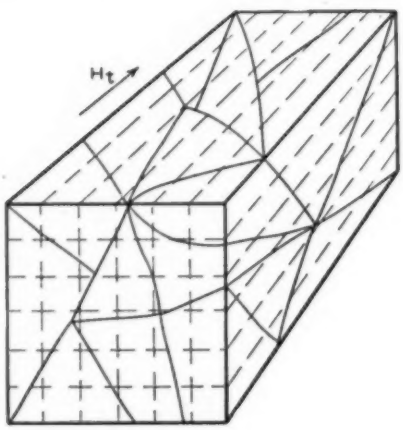

FIG. 1. Polycrystalline bar of Alnico 5. Heat treated in field in direction indicated. Dotted lines show direction of precipitation according to theory.

PREPARATION OF SPECIMENS

The alloy was first melted in a high frequency induction furnace and a 50-lb ingot $3\frac{1}{2}$ inches in diameter was cast. A four-inch length of this ingot was placed in a high temperature molybdenum-wound furnace and heated in a hydrogen atmosphere to a temperature close to the melting point (approximately 1400°C) and held there for three days, and then cooled at 2°C per minute to room temperature. The ingot was kept in the solid state, and the furnace had a temperature gradient of approximately 60°C for the length of the piece. Crystals were grown in this manner to avoid segregation occurring on melting and freezing. An analysis of the crystals gave the following composition: 7.96 percent Al, 14.48 percent Ni, 25.91 percent Co, 3.16 percent Cu, and 48.77 percent Fe, which is close to the attempted composition. Single crystal disks of approximately one-half-inch diameter and $\frac{1}{16}$-inch thickness were cut and oriented[2] from these crystals.

* An abstract of this paper was presented at the American Physical Society Meeting, Schenectady, June 14, 1951.

[1] Kittel, Nesbitt, and Shockley, Phys. Rev. 77, 839 (1950). See also reference 4.

[2] Walker, Williams, and Bozorth, Rev. Sci. Instr. 20, 947–950 (1949).

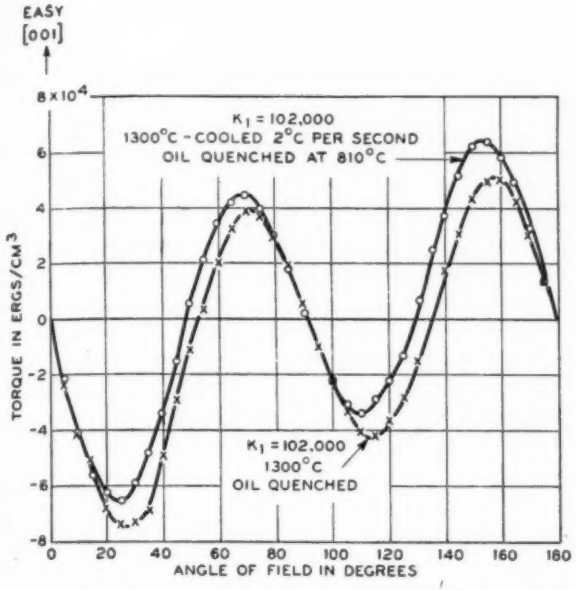

FIG. 2. Magnetic anisotropy of quenched Alnico 5 single crystals (100) plane.

RESULTS

The magnetic anisotropy and coercive force of the single crystal specimens were measured for a variety of heat treatments with and without the magnetic field. The main purpose of these experiments was to observe the changes in magnetic properties with different treatments and finally to account for the coercive force on the basis of magnetic anisotropy. The torsion method for measuring the magnetic anisotropy of the crystals was used. Briefly, it consists of rotating disk specimens in a strong uniform magnetic field of 8000 oersteds and measuring the torque necessary to turn the crystal away from a direction of easy magnetization. From the measured values of torque, the magnetic anisotropy constant K was computed by the use of the usual formulas[3] relating the torque to rotations in the cubic lattice.

If the alloy is quenched from 1300°C which is its solution temperature, the structure is largely body-centered cubic and the magnetic domains lie along the cube edges (⟨100⟩ directions) as observed by magnetic powder patterns. The torque curves for a specimen treated in this manner and for one cooled from 1300°C at approximately 2°C per second to 800°C and then oil quenched are shown in Fig. 2. The latter treatment causes the nuclei of the permanent magnet phase to form, and the alloy is said to be in the nucleated state. These torque curves are for disks cut in the (100) plane and show fourfold cubic symmetry with some distortion, but the anisotropy constants obtained by averaging the peak values are $K_1 = 102{,}000$ after each treatment. This rather low value is the anisotropy of the crystal, before substantial precipitation occurs.

[3] H. J. Williams, Rev. Sci. Instr. 8, 56–60 (1937).

When a crystal cut in the (100) plane is cooled from 1300°C at approximately 2°C per second without the presence of an applied magnetic field, and then aged at 590°C for 8 hours, the alloy may be thought of as divided into plates of precipitate and rectangular units of matrix. This is the standard treatment of Alnico 5 except that the magnetic field is not applied during heat treatment. In this case the precipitate grows in ⟨100⟩ directions as shown by the electron microscope picture in Fig. 11(a) of Part I. The torque curve for this crystal is shown in Fig. 3. Fourfold symmetry was obtained, but as a result of the precipitation that has occurred during cooling, the easy directions of magnetization have changed from ⟨100⟩ to ⟨110⟩ in the (100) plane. The anisotropy constant, K_1, is now $-141{,}000$ and so has changed in sign and increased in absolute value. Figure 3 also shows the torque curve obtained for the (110) plane having the same heat treatment. The easy directions in this plane are the ⟨111⟩ directions and the anisotropy constant K_1 is $-165{,}000$. The ⟨111⟩ directions are the easy directions in Alnico 5 after substantial precipitation of the permanent magnet phase, when it is not heat treated in a field. The two values of anisotropy constant K_1 agree reasonably well and we may assume an average value of about $-150{,}000$ for the anisotropy constant of the crystal after substantial precipitation of the permanent magnet phase. The coercive forces of the (100) and (110) disks in the directions of easy magnetization were, respectively, 419 and 426 oersteds.

More information on the crystal anisotropies of the matrix and precipitate can be obtained by the following

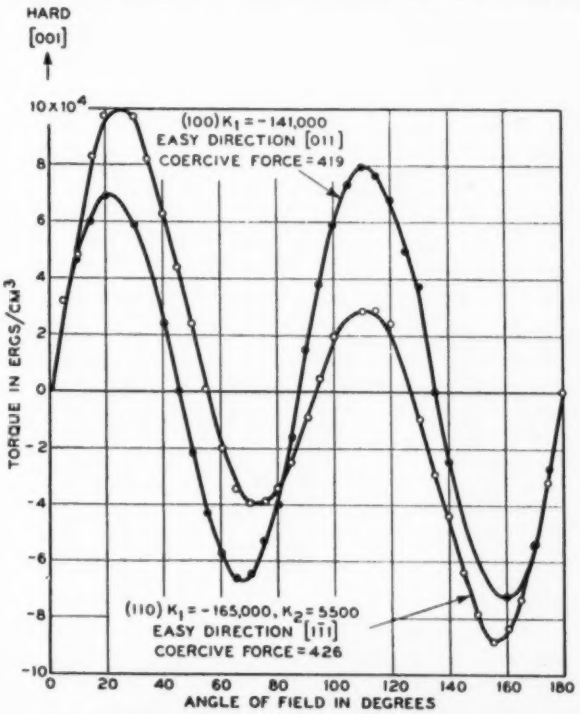

FIG. 3. Magnetic anisotropy of Alnico 5. Single crystals not heat treated in a field, aged at 590°C.

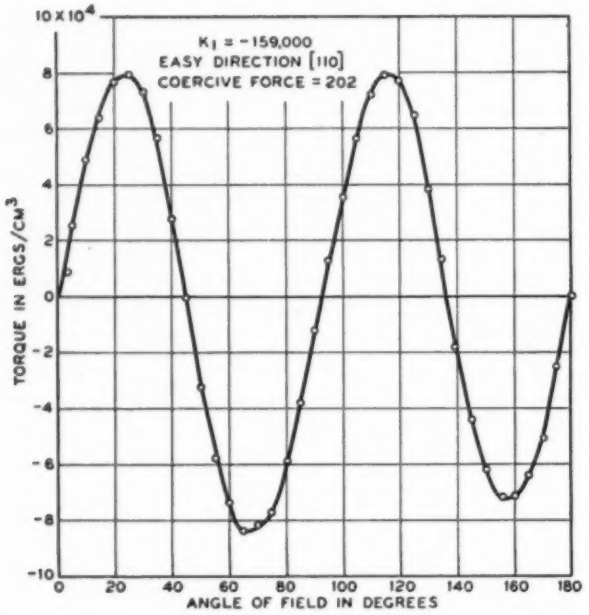

FIG. 4. Magnetic anisotropy of Alnico 5 single crystal (100) disk heat treated in a field perpendicular to its face, aged at 590°C.

experiment. If a disk cut in the (100) plane is heat treated in a field perpendicular to its face, according to theory and experiment, plates of precipitate material normal to the face of the disk will be obtained. All the precipitate rods in the plates will be oriented perpendicular to the surface of the disk. When the torque of the disk is measured by applying a field in the plane of the disk, the shape effect of the plates will cancel since the plates have a simple pattern of twofold symmetry and are 90° apart, and the torque measured will be mainly that resulting from the crystal anisotropy of the matrix and precipitate. The curve obtained is shown in Fig. 4. The crystal has fourfold symmetry, the easy directions in the plane of the disk are ⟨110⟩, and the anisotropy constant K_1 has a value of $-159{,}000$. This value is approximately the same as that obtained for the (100) and (110) planes when the crystal was aged but not heat treated in a field. According to the fine particle theory,[4] the coercive force is $2K_1/I$ and therefore for this case is $2\times159{,}000/1100$ or 290 oersteds. If we measure the coercive force of this crystal in the plane of the disk directly by the ballistic method, we obtain a value of 202 oersteds. The difference between this value and that calculated from the torque curve may be the result of the shape effect of the matrix introduced by the field heat treatment. The value of the coercive force due only to crystal anisotropy is about 300 oersteds, and this is a rather low value when one considers the final coercive force obtained (600 oersteds) when the alloy is heat treated in a field. Evidently for the latter heat treatment, shape anisotropy must be responsible for the additional coercive force obtained. This aspect of the subject will now be discussed.

When a crystal of Alnico 5 is heat treated in a field in a principal crystallographic direction, the easy direction of magnetization is the field direction and the crystal exhibits twofold magnetic symmetry. This is in contrast to the case without a field where the crystal symmetry prevails and the easy directions are the ⟨111⟩. Figure 5 shows a series of torque curves for Alnico 5 crystals heat treated in a field in the principal crystallographic directions and then aged. When a specimen cut in the (100) plane is heat treated in a [001] direction in the plane of the disk, precipitate forms in the [001] direction parallel to the field on all faces of the matrix rod except those normal to the field, as shown by the electron microscope pictures of Figs. 11b and 11c in Part I. The matrix domains will lie parallel to the precipitate domains in the plane of the disk, and in this position they can exert maximum torque with the applied field. This is indicated by the fact that the torque curve for this plane and orientation yield the highest anisotropy. The case for the [001] direction in the (110) plane is somewhat comparable. Here again the domains in the precipitate and the matrix will lie in the [001] direction and in a plane parallel to the plane of the disk being measured.

When a crystal is heat treated in a (110) plane in the $[1\bar{1}0]$ direction in the plane of the disk, the condition is different. The precipitate will tend to favor the ⟨100⟩ directions, and since most of these are not parallel to the (110) plane, the anisotropy will be lower than in the previous cases as shown in Fig. 5. However, the precipitate will be forced off the ⟨100⟩ directions by the field heat treatment and this is substantiated experi-

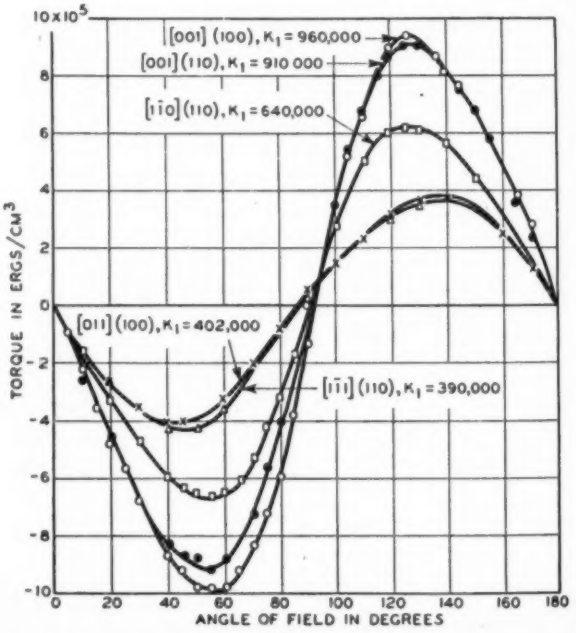

FIG. 5. Magnetic anisotropy of Alnico 5 single crystals heat treated in a field in the direction and parallel to the plane indicated.

[4] C. Kittel, Phys. Rev. **70**, 965–971 (1946); L. Néel, Compt. rend. **225**, 109 (1947); E. C. Stoner and E. P. Wohlfarth, Nature **160**, 650 (1947).

mentally by the electron diffraction photographs in Fig. 14 of Part I (field in [110]). In (a) of this figure, the precipitate diffraction spots do not have the cubic symmetry which they would have if the precipitate grew in ⟨100⟩ directions. In (b) of this figure, the crystal has been heated to 800°C, the alignment caused by the magnetic field heat treatment is reduced by this anneal, and the orientation of the precipitate is more nearly along cube planes. The precipitate in the [001] direction at right angles to the field will be completely suppressed, so that the field direction will be the easy direction of magnetization.

The strong tendency for the precipitate to grow in ⟨100⟩ directions can be observed in Fig. 11a of Part I. It appears that this tendency is controlled by crystal forces and not by the spontaneous magnetization of the matrix. Apparently the matrix becomes magnetic last on cooling; if it became magnetic first, its spontaneous magnetization would orient the precipitate, and the microstructure would appear similar to that shown in Fig. 11b. When a crystal cut in the (100) plane is heat treated in the [011] direction lying in the plane of the disk, the anisotropy is lower than in any of the previous cases. Because of the crystal forces, the precipitate will tend to favor the two ⟨100⟩ directions that are in the plane of the disk; but it will be forced toward the field direction, which is the direction of easy magnetization. Another unfavorable case occurs when a crystal in the (110) plane is heat treated in the $[1\bar{1}1]$ direction lying in the plane of the disk. Then the field does not favor any one of the three ⟨100⟩ directions and the anisotropy for field heat treatment is again low because of the conflict between the field and the crystal forces. As a result of the field heat treatment, however, the crystal has lost its normal twofold symmetry which is caused by crystal anisotropy, and it now has a simple twofold symmetry which is characteristic of the magnetic field heat treatment. This symmetry is caused by the tendency of the precipitate to lie parallel to the direction of the magnetic heat-treating field. The anisotropy of the crystal heat treated in a field in the $[1\bar{1}1]$ direction is approximately twice the value obtained without field heat treatment.

Summarizing, the effect of the applied field on the magnetic precipitate is that the precipitate has a natural tendency to grow in the three ⟨100⟩ directions, but if the applied field is normal to one of these directions, it will prevent the precipitate from growing in that direction. In addition, for other important directions the precipitate will be affected by the strong crystal forces in the ⟨100⟩ directions, but in general it will be forced toward the field vector and this will be the easy direction of magnetization.

If a crystal is heated to 800°C after being treated to obtain permanent magnet properties, the precipitate will grow so that it can be studied by the electron microscope. In general, only the precipitate which is in ⟨100⟩ directions will remain stable on heating to 800°C.

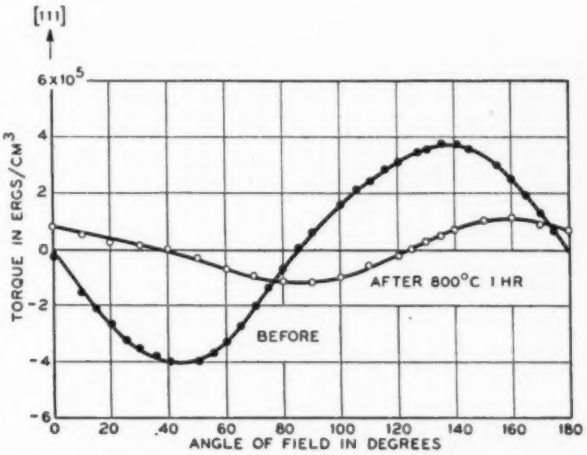

FIG. 6. Magnetic anisotropy of Alnico 5 crystal (110) plane before and after heat treatment at 800°C for 1 hr. Previous heat treated with field in $[1\bar{1}1]$ in plane of disk and aged at 590°C.

Figure 6 shows torque curves taken before and after this 800°C treatment on a crystal cut in the (110) plane and heat treated in a $[1\bar{1}1]$ direction in the plane of the disk. After the 800°C treatment, the anisotropy is lower and the easy direction has shifted 40° from the $[1\bar{1}1]$ to within 15° of the [001] direction in the plane of the disk. The reason for this large shift in the direction of easy magnetization is clearly shown by the electron microscope photograph in Fig. 13b of Part I. Here we observe that the precipitate itself is lying within 15° of the [001] direction in the plane of the disk. Thus the easy direction of the crystal has shifted 40° upon heating to 800°C because the precipitate itself has shifted 40°.

The coercive forces of the crystals in the various crystallographic directions were also measured in addition to the anisotropy measured by the torque method (torque anisotropy). Table I shows the values obtained on both coercive force and anisotropy. The results on the anisotropy of coercive force are parallel in a general way to the results on the torque anisotropy. For example, the coercive force in the [001] direction in the (100) plane was 598 oersteds; and perpendicular to this direction, but still in the plane of the disk, it was 220 oersteds. This difference of 378 oersteds is the largest difference in coercive force obtained, and it is accompanied by the highest anisotropy constant of 960,000. Also the coercive force in the $[1\bar{1}1]$ direction in the (110) plane was 495 oersteds and perpendicular to this direction but still in the plane of the disk, it was 392 oersteds. This difference of 103 oersteds and its accompanying anisotropy K_1 of 390,000 was the lowest obtained for crystals heat treated in a field.

The anisotropy constants obtained by measurement can not always be used directly to calculate the coercive force on the basis of the fine particle theory. For example, for the crystal cut in the (100) plane and heat treated in the [001] direction in the plane of the disk, the anisotorpy K_1 is 960,000. According to fine particle

TABLE I.

Plane of disk	Heat treatment	Anisotropy K_1	Anisotropy K_2	Coercive force in easy direct.	Coercive force in hard direct.	Easy direction of magnetization
(100)	1300°C—Oil quench	102,000		10	···	[001]
(100)	1300°C—Cooled 2°C/sec to 800°C —then oil quenched	102,000		20	···	[001]
(100)	1300°C—Cooled 2°C/sec—no field +590°C—7 hr	−141,000		419	···	[011]
(110)	1300°C—Cooled 2°C/sec—no field +590°C—7 hr	−165,000	+5500	426	···	[1$\bar{1}$1]
(100)	1370°C—Cooled approx. 2°C per min	− 35,500		186	···	[011]
(100)	1300°C—Cooled 2°C/sec—field in [001] in plane of disk +590°C—7 hr	960,000		598	220	[001]
(110)	1300°C—Cooled 2°C/sec—field in [001] in plane of disk +590°C—7 hr	910,000		605	348	[001]
(110)	1300°C—Cooled 2°C/sec—field in [1$\bar{1}$0] in plane of disk +590°C—7 hr	−640,000		434	189	[1$\bar{1}$0]
(100)	1300°C—Cooled 2°C/sec—field in [011] in plane of disk +590°C—7 hr	−402,000		495	388	[011]
(110)	1300°C—Cooled 2°C/sec—field in [1$\bar{1}$1] in plane of disk +590°C—7 hr	−390,000		495	392	[1$\bar{1}$1]
(110)	Above treatment +800°C—1hr	−111,000		···	···	15° off [001]
(100)	1300°C—Cooled 2°C/sec—field ⊥ to (100) face of disk	− 98,500		···	···	[011]
(100)	Above treatment +590°C—7 hr	−159,000		202	···	[011]

theory, the coercive force is $2K_1/I_s$ or $2\times960{,}000/1100$ which equals 1750 oersteds. This value may be compared with the measured value of 598 oersteds obtained by the ballistic method. The agreement is poor, but the assumption that we have mainly single domain action is reasonable because the size of both the matrix and precipitate have been determined experimentally and are of the right size for single domain action. Other factors, also, indicate that the magnetic mechanism is primarily one of rotation rather than boundary movement. The coercive force appears to be too dependent upon small particle size to be explained by a domain wall cutting across areas of strain or magnetic cavities. For example, if the size of the matrix is increased from 200 to 850 angstroms by heat treatment at 800°C, the coercive force will decrease from 600 to 10 oersteds.

The reason for the discrepancy between the calculated and measured values of coercive force may be due to the difference in the anisotropy of the rods of matrix and the rods in the plates of precipitate; the former, having the greater volume and less shape effect, largely determines the coercive force. When the torque anisotropy of this parallel combination is measured, that caused by each constituent is additive, but when the coercive force is measured by the ballistic method, the lower anisotropy prevails. A reverse field applied to the combination probably changes the flux through the matrix first since it has the lower shape effect, and this is the main factor in determining the coercive force.

Figure 7 shows a simplified permanent magnet structure deduced from the electron micrographs of Fig. 11 of Part I. It gives the approximate dimensions and domain orientations for the structure with and without the field heat treatment. The most important result of the field heat treatment is to cause a large increase in the residual induction of the alloy. The reason for this is the growth of precipitate parallel to the field direction, and this establishes a single easy direction of magnetization. In practice, the residual induction is increased from 9000 to 13000 gauss with field heat treatment, and this increase corresponds approximately to a rotation of 45° of the magnetization vector (13000 cos 45°=9100).

We have seen that the part of the coercive force of the matrix, which is the result of crystal anisotropy, is approximately 300 oersteds. Since this is too low a value to account for the value of 600 oersteds measured when the alloy is heat treated in a field, an additional mechanism must be assumed. The torque curves for the crystals heat treated in a field indicate shape anisotropy (twofold symmetry), and therefore the additional 300 oersteds may be accounted for in this manner. According to the unpublished work of Shockley and Kittel,

$$H_c=(1-1.1P)2\pi\Delta I_s,$$

where P is the packing factor of the matrix which in this case is approximately $\frac{2}{3}$ and ΔI_s is the unknown difference in the saturation magnetization of the matrix and precipitate. If H_c equals 300 oersteds, caused by shape anisotropy, the calculated value of ΔI_s is 177. Therefore, a difference of $177\times4\pi$ or 2230 gauss in the saturation of the matrix and precipitate would account for 300 oersteds of the coercive force on the basis of shape anisotropy. The total coercive force of the alloy heat treated in a field is then accounted for on the basis

of the crystal anisotropy of the matrix and precipitate and the shape effect of the matrix.

CONCLUSIONS

The experimental work of Parts I and II of this paper substantially confirmed the physical picture established by the Kittel, Nesbitt, and Shockley theory of Alnico 5. A new face-centered cubic precipitate, transitory in nature, was found which is essential in accounting for the alloy's permanent magnet properties. The experimentally determined size of the matrix rod (200A) was within the range (100 to 1000A) predicted by the theory. Also, the over-all shape of the precipitate was plate-like, but the plates themselves were found to be made up of rods. This latter fact is consistent with Néel's theory[4] which predicted ellipsoids of revolution. Geisler[5] in his work on Alnico 5 also observed the plate-like shape of the precipitate. The magnetic precipitate grows in the direction of the field predicted by our theory; however, there is a strong tendency because of crystal forces for the alloy to precipitate in ⟨100⟩ directions. Some investigators[6,7] have found indications that the domain magnetization follows the [100] direction nearest the field. More recently Hoselitz and McCaig[8] found that when a field applied during cooling makes an angle with the [100] direction, the direction of easy magnetization is much nearer the [100] than the field direction. In our work we found that when the field was applied in the principal crystallographic directions ([100], [110], [111]), the direction of easy magnetization was the field direction. If the field is applied at a moderate angle to the [100] direction, the direction easy magnetization lies between the field vector and the [100] direction. Specifically, when the field was applied 40° off the [001] direction in the (110) plane, the easy direction of the single crystal was found to lie 29° off the [001]. Also, when the field was applied 22° off the [001] direction in the (110) plane, the easy direction was found to lie 11° off the [001]. These results are in agreement with a recently published magnetic powder pattern photograph[9] of Alnico 5 in which the maximum deviation between the applied field direction and the domain magnetization is 10°.

The coercive force of the alloy has been accounted for by fine-particle theory on the basis of domain rotations rather than boundary movements. Stoner and Wohlfarth[4] have also viewed the alloy in this manner. The small size and shape of the matrix rod, and the dependence of the coercive force upon these factors substantiate this view of domain rotations.

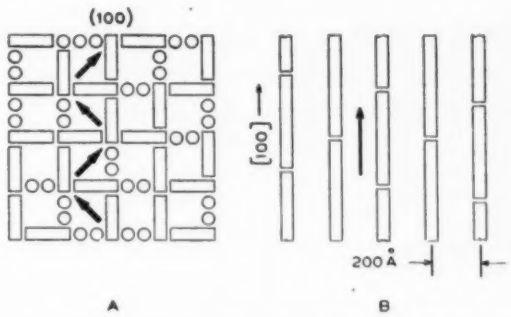

FIG. 7. Simplified permanent magnet structure showing domain orientation: (A) Without heat treatment in magnetic field. (B) With heat treatment in magnetic field.

Goldman and Smoluchowski[10] have expressed the view that the properties of Alnico 5 are caused by the anisotropy of magnetostriction of the precipitate which they assume to be an iron-cobalt alloy of approximately 30 percent cobalt. Our work shows that the precipitate is not the simple iron-cobalt alloy but a complicated face-centered cubic cell with a lattice constant of 10A whose composition and magnetostriction are not known at the present time.

The fundamental permanent magnet units consist of two kinds of chemically different single magnetic domains in parallel, one of precipitate and the other of matrix material. The precipitate appears to have a higher Curie point, but the matrix has the larger volume, and it largely determines the coercive force of the alloy. When the alloy is heat treated in a field, the matrix possesses shape anisotropy because of elimination of transverse precipitation. This accounts for the increase in coercive force when the alloy is so treated. After cooling the alloy from its solution temperature of 1300°C the nuclei for the permanent magnet phase become magnetic in the vicinity of 900°C and grow preferentially parallel to the field direction. In the vicinity of 800°C the matrix becomes magnetic, and substantial precipitation of the permanent magnet phase begins. At this point the anisotropic properties of Alnico 5 are established and subsequent heat treatment below this temperature merely continues the growth of the precipitate on the predetermined planes.

ACKNOWLEDGMENTS

The authors are greatly indebted to R. M. Bozorth, W. Shockley, C. Kittel, H. J. Williams, and J. K. Galt for valuable discussions and suggestions during the work, and to Mrs. M. H. Read and J. G. Walker for assistance in mechanical preparation and x-ray orientation of the specimens.

[5] A. H. Geisler, Trans. Am. Soc. Metals **43**, 70–104 (1951).
[6] K. Hoselitz and M. McCaig, Proc. Phys. Soc. (London) **B62**, 163–190 (1949).
[7] J. J. Went, J. phys. et radium **12**, 457 (1951).
[8] K. Hoselitz and M. McCaig, Proc. Phys. Soc. (London) **B64** 549–559 (1951).
[9] E. A. Nesbitt, J. Appl. Phys. **21**, 879–889 (1950).
[10] J. E. Goldman and R. Smoluchowski, Phys. Rev. **80**, 320 (1950).

Letters to the Editor

Reduction of Three-Dimensional Electromagnetic Problems

JOHN W. MILES*
Auckland University College, Auckland, New Zealand
(Received December 5, 1951)

LET $\phi^1(x, y, \tau)$ be a solution to the two-dimensional wave equation

$$\phi_{xx}+\phi_{yy}=\phi_{\tau\tau} \tag{1}$$

where $\tau=ct$ (c and t being velocity of light and time). Then the electromagnetic field specified by

$$\mathbf{E}^1=\left(\mathbf{k}\frac{\partial}{\partial\tau}+\cos\theta\nabla\right)\phi^1(x\sin\theta, y\sin\theta, \tau-z\cos\theta) \tag{2a}$$

$$\mathbf{H}^1=\zeta\mathbf{k}\times\nabla\phi^1(x\sin\theta, y\sin\theta, \tau-z\cos\theta) \tag{2b}$$

represents a solution to Maxwell's equations

$$\nabla\times\mathbf{E}=-\eta\mathbf{H}_\tau \tag{3a}$$

$$\nabla\times\mathbf{H}=\zeta\mathbf{E}_\tau \tag{3b}$$

$$\nabla\cdot\mathbf{E}=0 \tag{3c}$$

$$\nabla\cdot\mathbf{H}=0 \tag{3d}$$

$$\eta=\zeta^{-1}=(\mu/\epsilon)^{\frac{1}{2}}, \tag{4}$$

where η is the characteristic impedance of the medium. This solution is constrained to have a null component of $\mathbf{H}$ parallel to the z axis (unit vector $\mathbf{k}$) and to travel at an inclination θ to this axis.

Similarly, in virtue of the symmetry of (3) with respect to the interchange of $\mathbf{E}$ and $-\mathbf{H}$ and η and ζ,

$$\mathbf{E}^2=-\eta\mathbf{k}\times\nabla\phi^2(x\sin\theta, y\sin\theta, \tau-z\cos\theta) \tag{5a}$$

$$\mathbf{H}^2=\left(\mathbf{k}\frac{\partial}{\partial\tau}+\cos\theta\nabla\right)\phi^2(x\sin\theta, y\sin\theta, \tau-z\cos\theta) \tag{5b}$$

represents a linearly independent solution that has a null component of $\mathbf{E}$ parallel to the z axis and moves at an inclination θ thereto.

These solutions have application to diffraction problems in which the generator of the diffracting surface (or surfaces) and its boundaries are everywhere parallel to the z axis, but in which the incident wave front is not parallel to this axis. The boundary conditions appropriate to a perfectly conducting obstacle are

$$\phi^1=0 \tag{6}$$

$$\phi_n^2=0. \tag{7}$$

Hence, the transformations of (2) and (5) reduce the solution of a three-dimensional ("quasi-two-dimensional" might be more descriptive) electromagnetic diffraction problem to a pair of two-dimensional scalar problems. (The reduction of two-dimensional electromagnetic problems to a pair of scalar problems is of course well known.)

We remark that there is nothing particularly novel about the form of the solutions (2) and (5), since they are merely particular cases of general solutions discussed by Stratton.[1] Thus, (2) may be derived from a Hertz vector parallel to the z axis. Moreover, the reduction for the special case of a half plane has been noted by Clemmow.[2] However, as far as we are aware, no one has previously set down the specific formulas (2) and (5), which have direct application to such problems as slits, ribbons, gratings, wedges, sets of planes, etc., for which two-dimensional solutions are known.

Note added in proof.—The referee has pointed out that, in the case of a monochromatic time dependence, the foregoing transformation has been used to reduce rectangular wave-guide problems to parallel plate problems.

* On leave from University of California, Los Angeles, California.

[1] J. A. Stratton, *Electromagnetic Theory* (McGraw-Hill Book Company, Inc., New York, 1941), p. 21.

[2] P. C. Clemmow, unpublished; see E. T. Copson, Proc. Roy. Soc. (London) **A202**, 277 (1950).

Heat Conduction Along an Exponential Bar

JOHN W. MILES*
Fulbright Lecturer, Auckland University College, Auckland, New Zeland
(Received December 28, 1951)

THE solution of the equation

$$(e^{\alpha z}f_z)_z=e^{\alpha z}f_t, \quad f=f(z, t), \tag{1}$$

representing one-dimensional diffusion (in particular, heat conduction) along a tube of exponentially varying cross section does not appear to be in the standard references.[1]

Having had occasion to require it (the problem came to the writer in connection with an investigation of condensation carried out by Dr. F. Farley of Auckland University College), we present here a solution to (1) subject to the conditions

$$f(z, 0)=0 \tag{2}$$

$$f(0, t)=1 \tag{3a}$$

$$f(\infty, t)=0. \tag{3b}$$

The Laplace transform of the solution is given by

$$F(z, s)=s^{-1}\exp\{-[\alpha+(\alpha^2+4s)^{\frac{1}{2}}]\cdot(z/2)\}, \tag{4}$$

the inverse of which is

$$f(z, t)=e^{-\alpha z}\{1-\tfrac{1}{2}\operatorname{erfc}[\tfrac{1}{2}(\alpha t^{\frac{1}{2}}-zt^{-\frac{1}{2}})]+\tfrac{1}{2}\operatorname{erfc}[\tfrac{1}{2}(\alpha t^{\frac{1}{2}}+zt^{-\frac{1}{2}})]\}. \tag{5}$$

where

$$\operatorname{erfc}(z)=1-\operatorname{erf}(z)=2\pi^{-\frac{1}{2}}\int_z^\infty \exp(-\zeta^2)d\zeta. \tag{6}$$

The steady state distribution corresponding to (5) is

$$f(z)=\lim_{t\to\infty}f(z, t)=e^{-\alpha z}. \tag{7}$$

* On leave from University of California, Los Angeles.

[1] H. S. Carslaw and J. C. Jaeger, *Conduction of Heat in Solids* (Oxford University Press, London, 1948).

Physical Entropy and Information

D. A. BELL
Department of Electrical Engineering, University of Birmingham, England
(Received October 15, 1951)

THE various models which have been proposed as a link between the negative entropy of information theory and the positive entropy of thermodynamics[1] have, I believe, thrown into relief a point which has been glossed over in the past; and since it has been so persistently glossed over, I hope I may be excused for using some very elementary analogies in order to introduce the point at issue.

If a civil engineering contractor measures a bulk of material (soil, concrete, etc.) in "yards," any physicist will mentally interpret the unit as "cubic yards," and would justify this on the grounds of "correct dimensions." Now in the theory of heat engines one always finds that kT is an energy (k=Boltzmann's constant, T=temperature) but k and T have not been satisfactorily allocated individual dimensions, any more than have the μ and κ of electromagnetic theory which jointly have the dimensions of (velocity)$^{-2}$. It is true that entropy is defined (from statistical mechanics) as $S=k\ln W+S_0$, but so far as thermodynamics is concerned, the association of this entropy with a physical system always involves temperature, so that the kT combination cannot be physically separated in this way.

If I may turn aside for another analogy, one might measure accelerations in units of g and then find that mass and weight are identical. This hypothesis would, of course, soon be destroyed by the discovery that g is not a universal constant, but a function of position relative to the earth's mass. But even if we had not the means to detect the variation of weight of a given mass, it would be found convenient to separate the two concepts as soon as one worked with nongravitational forces, e.g., in the measurement of e/m of the electron.

Now there is no doubt that the measure of information, as developed by Hartley,[2] Shannon,[3] Wiener,[4] and others, is a pure number. Moreover, it is now well established that if one measures information in units of k times a function of the type $-\log W$, thermodynamic entropy and information can be handled jointly in a way which makes the "Maxwell demon" type of model consistent with the second law of thermodynamics. Here, then, is the point at issue. Is the introduction of k into information units as deceptive as the measurement of acceleration in units of g, i.e., are "information" and "entropy" essentially quantities which differ in kind? Or are they identical in kind, in which case information-theory would tell us conclusively that Boltzmann's k must be regarded as a pure number, whence it would follow that entropy is a pure number and that temperature has the same dimensions as energy?

The latter seems a very satisfactory convention; statistical entropy is a function of "pattern" and might well be a pure number, while temperature is primarily associated with "energy per degree of freedom," and could well be of the dimensions of energy. But is there any objection to this convention from the point of view of thermodynamics?

[1] L. Brillouin, J. Appl. Phys. **22**, 338 (1951).
[2] R. V. Hartley, Bell Syst. Tech. J. **7**, 535 (1928).
[3] C. E. Shannon, Bell Syst. Tech. J. **27**, 379 and 623 (1948).
[4] N. Wiener, *Cybernetics* (John Wiley & Sons, Inc., New York, 1948).

Radiofrequency Field Quenching of Ultraviolet Excited Phosphors

T. Miller and K. N. Fromm*
Westinghouse Research Laboratories, East Pittsburgh, Pennsylvania
(Received December 19, 1951)

RECENTLY Destriau and Mattler have reported a quenching action produced by fifty-cycle electric fields upon x-ray excited phosphors.[1] Experiments in this laboratory with sixty-cycle fields applied to ultraviolet excited phosphors failed to produce any appreciable quenching effects. However, with increasing field frequency pronounced quenching was observed.

The phosphor is deposited at a thickness of 10 mg per square cm on a one-inch square aluminum plate. The rf field is applied between the aluminum electrode and a transparent electrically conducting glass plate having a surface resistance of thirty ohms per square area. A 0.0015-in. thick sheet of clear mica insulates the phosphor layer from the conducting surface of the glass.

Figure 1 illustrates the dependence of the quenching action upon the magnitude of the rf potential applied across the phosphor cell for copper and silver activated zinc cadmium sulfide phosphors. The zinc cadmium mixing ratios for these phosphors are such that both luminesce in an orange-red color. Other sulfide phosphors exhibit similar quenching characteristics. However, preliminary tests with zinc phosphate and zinc orthosilicate phosphors indicate that such phosphors are not affected by the rf field.

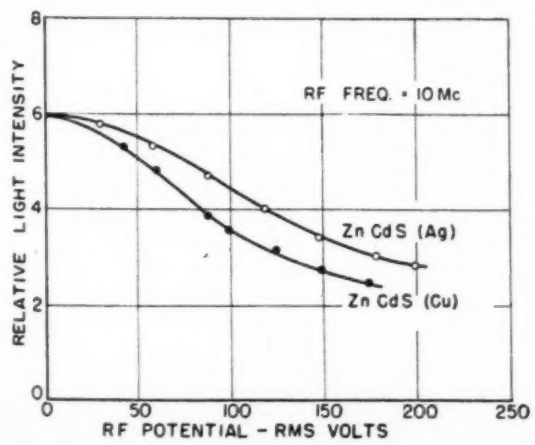

FIG. 1. Relative light intensity *vs* rf potential across phosphor cell.

Experiments are now in progress to determine the response time of the phosphors to amplitude modulated rf fields, the dependence of the quenching action on the intensity of the ultraviolet excitation, and the relationship between the percent quenching and field frequency.

* Now at Capehart-Farnsworth Corporation, Ft. Wayne, Indiana.
[1] Destriau and Mattler, J. phys. et radium **9**, 238 (1948).

Diffusion in Grain Boundaries

M. H. Dawson
Metallurgical Laboratories, Sylvania Electric Products, Incorporated, Bayside, New York
(Received December 3, 1951)

IT is the purpose of this note to point out that the work of Achter and Smoluchowski on diffusion in grain boundaries may really be a study of grain boundary precipitation as a function of solute super saturation and orientation difference at grain boundaries.

The photomicrographs presented by Achter and Smoluchowski[1] are in every respect similar to those observed in some age-hardening systems where there is no question of grain boundary diffusion. The grain boundaries act as preferred sites for nucleation so that no precipitate is observed within the grain, even though the concentration is initially uniform throughout.

I propose that the results of Achter and Smoluchowski may be explained in the following way. At the temperature of the diffusion anneal, Ag and Cu interdiffused by the customary mechanism of volume diffusion. On cooling, a precipitation reaction was nucleated at the grain boundaries. The amount of precipitate observed is a measure of the volume concentration of silver.

This explanation is quantitatively reasonable. The diffusion distance, $4Dt$, may be reasonably estimated at 0.2 mm from Fig. 5 of reference 1. This estimate corresponds to a value of D of 2×10^{-10} cm²/sec. Rhines and Mehl[2] studied the diffusion of Si, Al, Zn, Sn, and Be in copper and their values for D at 725°C lie between 0.8×10^{-10} and 3×10^{-10} cm²/sec. If grain boundary diffusion alone were responsible for the precipitate at the grain boundaries, one would expect a much greater penetration than observed by Achter and Smoluchowski.

[1] M. R. Achter and R. Smoluchowski, J. Appl. Phys. **22**, 1260–64 (1951).
[2] F. N. Rhines and R. F. Mehl, Trans. Am. Inst. Mining Met. Engrs., Inst. Metals Div. **128**, 185 (1938).

Diffusion in Grain Boundaries

M. R. Achter and R. Smoluchowski
Westinghouse Atomic Power Division and Carnegie Institute of Technology, Pittsburgh, Pennsylvania
(Received December 19, 1951)

IN the preceding note[1] Dr. Dawson brings up the question of whether the effects which we observed[2] along grain boundaries (see Fig. 1) were a result of preferential precipitation or to preferential diffusion. It was clear to us early in the course of our investigation that this problem needs an unequivocal answer.[3] Briefly our arguments are as follows:

(a) In the slow-cooled samples (Fig. 3, reference 2) in which there is ample time for precipitation to occur, there is a definite thin line of almost continuous precipitate visible along the boundary. This line is surrounded by a wide band of dispersed precipitates. While the former is clearly nucleated at the boundary,

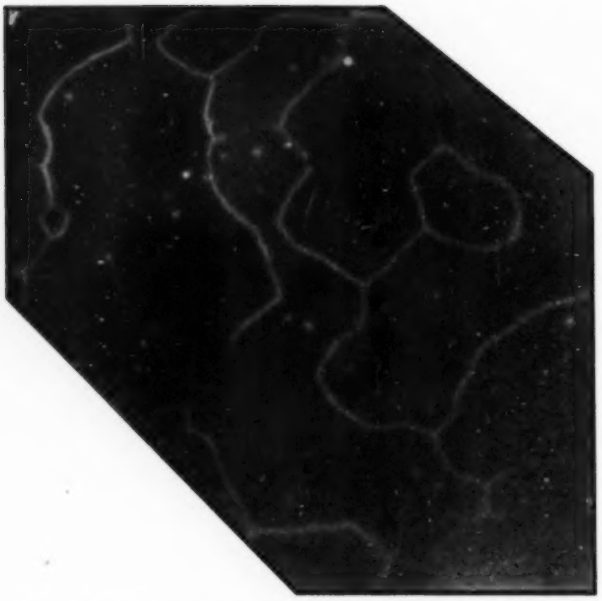

FIG. 1. Autoradiograph showing preferential concentration of radioactive silver along certain grain boundaries of columnar copper after diffusion (cut parallel to the interface).

the latter is nucleated in the volume of the grain (up to 0.1 mm distance from the grain boundary) and thus it does not depend on the accelerated rate of precipitation along boundaries.

(b) In the quenched samples (Fig. 4, reference 2), the wide dark band of dispersed precipitates either does not show up at all or is very narrow. On the other hand, the wide white band associated with an etch limit in the solid solution shows up clearly. In the slow-cooled samples the white band shows up distinctly even after the zone of precipitates has been passed. This means that even in the slow-cooled samples there still exists excess silver in solid solution outside of the region of disperse precipitates.

(c) If the observed effect were associated with volume diffusion as suggested by Dawson, then its activation energy would be almost twice that observed. It is the activation energy and not the absolute value of the diffusion coefficient which distinguishes volume diffusion from grain boundary diffusion.

(d) With radioactive silver in the diffusion couple one obtains a pattern strikingly similar to that shown in Fig. 4, reference 2, as the enclosed autoradiograph obtained in our laboratory by Mr. Donald G. Shafer indicates. The effect, in this case, is independent of the state of silver, whether it is in precipitate or in solid solution.

(e) If the effect were controlled by the rate of precipitation at the grain boundaries, it would not show the observed dependence upon the direction of diffusion in a given grain boundary.[4]

This research was supported by an AEC contract.

[1] M. H. Dawson, J. Appl. Phys. **23**, 373 (1952), this issue.
[2] M. R. Achter and R. Smoluchowski, J. Appl. Phys. **22**, 1260 (1951).
[3] M. R. Achter and R. Smoluchowski, *Symposium on Physics of Powder Metallurgy* (McGraw-Hill Book Company, Inc., New York, 1951).
[4] M. R. Achter and R. Smoluchowski, Phys. Rev. **83**, 163 (1951).

Shock Wave Formation in a Shock Tube

GEORGE A. LUNDQUIST
U. S. Naval Ordnance Laboratory, White Oak, Silver Spring, Maryland
(Received November 8, 1951)

MEASUREMENTS of shock-wave speed as a function of pressure ratio across the diaphragm separating high and low pressure chambers of a shock tube have been made by a large number of observers. In general, excellent agreement between measured and theoretically predicted shock velocities was found for low pressure ratios,[1,2] but an increasing deficiency of shock velocity was observed as diaphragm pressure ratios were increased above about three.[3,4]

Studies of shock waves near the diaphragm have shown that their formation is influenced considerably by the erratic diaphragm breakage. Reynolds[1] found that under some conditions a considerable time is taken for the initial pressure impulse to steepen into a shock wave. Smith[2] observed that in his tube strong shock waves were still somewhat curved after traveling 7½ feet from the diaphragm.

Lukasiewicz[5] has recently pointed out that the performance of light screens, or miniature Schlieren systems used to time the propagation of shock waves, may give some clues as to the development of the waves. He noted that several observers reported a failure of these units to operate at high diaphragm pressure ratio when placed close to the diaphragm, because of curvature or incomplete formation of the shock waves.

In view of this, Lukasiewicz suggested that deviations of measured shock speeds from theoretically predicted values may be a result of taking measurements too close to the diaphragm where shock waves have not had sufficient time to form completely. He proposed that measurements made at a sufficient distance from the diaphragm would show a close approach to theoretical predictions.

This was confirmed in tests made in a 20×20 cm shock tube. Air at 24°C was used in both chambers. Diaphragm pressure ratios up to 10,000 were obtained with pressures from 1 to 3 atmospheres in the high pressure chamber and pressures down to 0.2 mm Hg abs. in the low pressure chamber. Pressure ratios were measured with an accuracy of at least 5 percent and shock velocities with an accuracy of at least 1 percent. Glow discharge probes were used to time the shock waves at low pressures where light screens failed to operate.

As shown in Fig. 1, for a given pressure ratio shock velocities measured close to the diaphragm position were consistently smaller than those measured at greater distances. The shock waves accelerate for a considerable distance before reaching a constant velocity. Higher velocity shock waves require a greater time and length of tube to reach a maximum velocity than do the slower ones. At a distance of about 5 meters in this tube, shock waves for all diaphragm pressure ratios up to 10,000 reach a maximum velocity which is essentially equal to that predicted by shock tube theory. These measurements indicate that effects of noninstan-

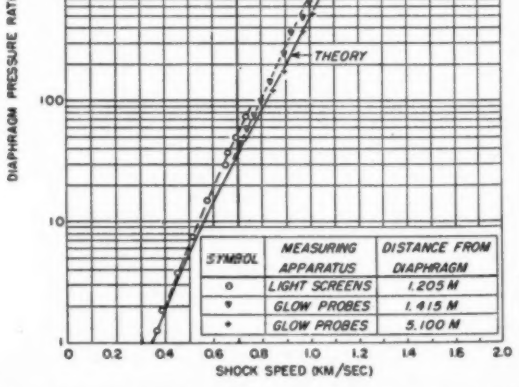

FIG. 1. Measurements of shock speed *vs* diaphragm pressure ratio taken at increasing distances from the diaphragm.

taneous diaphragm breakage on the propagation of strong shock waves may be negligible if a sufficiently long shock tube is used.

[1] G. T. Reynolds, "A preliminary study of plane shock waves formed by bursting diaphragms in a tube," OSRD Report No. 1519 (1943).
[2] Huber, Fitton, and Delpino, "Experimental investigation of moving pressure disturbances and shock waves and correlation with one-dimensional unsteady flow theory," NACA TN 1903 (1949).
[3] L. G. Smith, "Photographic investigation of the reflection of plane shocks in air," OSRD Report No. 6271 (1945).
[4] A. Hertzberg and A. Kantrowitz, J. Appl. Phys. **21**, 874 (1950).
[5] J. Lukasiewicz, "Shock tube theory and applications," National Research Council of Canada Report MT-10, Appendix A (1950). Also "Notes on shock tube experiments conducted at Universities of Michigan and Toronto" (private communication), File M2-17-13. F-2, National Research Council of Canada (1950).

A New Superlattice in Co-Pt Alloys

A. H. Geisler and D. L. Martin
General Electric Research Laboratory, The Knolls, Schenectady, New York
(Received December 17, 1951)

SUBSEQUENT to a recent study of the constitution of Co-Pt alloys around the 50 atomic percent composition[1] the structure of an alloy which contained 30 atomic percent cobalt was investigated. It was found by x-ray diffraction analysis that this alloy formed a superlattice of the type to be expected for Pt_3Co; it is face-centered cubic with Co atoms on the corner sites and Pt atoms on the face centers analogous to Cu_3Au. Previously, only the tetragonal face-centered superlattice CoPt has been reported.[2] However, in view of the observation of $FePt_3$, FePt, and Fe_3Pt in the iron-platinum system one might expect to find similar phases in the Co-Pt alloys.[3]

The Pt_3Co superlattice was present in samples of the 30 percent Co alloy after heat treating for 100 hours at 500°C, 600°C, or 700°C. This time interval was not sufficient to order the alloy at 400°C. On quenching from 800°C only the disordered phase was present in the sample. Thus, the transformation temperature range is located between 700°C and 800°C. The lattice parameter of the phase disordered at 800°C was 3.829A while that of the phase ordered at 700°C was 3.831A. The small difference in lattice parameter might make it difficult to detect the coexistence of the two phases by x-ray diffraction and may account for the absence of the supplementary microstructural features such as strain markings (striations) and recrystallization which have been attributed to the development of strains during ordering.[4]

The equilibrium between the disordered solid solutions and the ordered Co-Pt phase was the subject of the previous report.[1] Research has now been started to study the constitution around the Pt_3Co composition as well as elsewhere to establish the two phase equilibria throughout the Co-Pt alloy system.

[1] Newkirk, Smoluchowski, Geisler, and Martin, J. Appl. Phys. **22**, 290 (1951).
[2] E. Gebhardt and W. Köster, Z. Metallkunde **32**, 253 (1940).
[3] A. Kussmann and G. Gräfin V. Rittberg, Z. Metallkunde **42**, 470 (1950).
[4] Newkirk, Geisler, Martin, and Smoluchowski, Trans. Am. Inst. Mech. Engrs. **188**, 1249 (1950).

JOURNAL OF APPLIED PHYSICS VOLUME 23, NUMBER 3 MARCH, 1952

Announcements

Conferences

The spring meeting of the Association for Computing Machinery will be held at Mellon Institute, Pittsburgh, Pennsylvania, May 2 and 3, 1952.

Modern Network Synthesis (Audio to Microwaves) is the subject of a Symposium to be held on April 16, 17, and 18, 1952, at the Engineering Societies Building Auditorium (33 West 39 Street) in New York City. This Symposium, jointly sponsored by the Polytechnic Institute of Brooklyn and the Office of Naval Research, will summarize the progress to date in the various fields of network synthesis and highlight new developments of current interest to engineers and physicists. American and European authorities, who have made original contributions to the art, will participate.

No registration fee will be charged for admission to this Symposium. Proceedings of the Modern Network Synthesis Symposium will be published by September, 1952, at a cost of four dollars ($4.00) per copy. Orders for the Proceedings, accompanied by check or money order made out to "Treasurer, Network Symposium," will be accepted in advance. Copies of the detailed program, hotel accommodation information, and registration forms are available on request. All correspondence should be addressed to:

Polytechnic Institute of Brooklyn
Microwave Research Institute
55 Johnson Street
Brooklyn 1, New York

All persons interested in attending are urged to register early.

The Physical Society's 36th Annual Exhibition of Scientific Instruments and Apparatus will be held from Thursday, April 3rd, to Tuesday, April 8th, 1952, excluding Sunday.

As in 1951 the Exhibition will be located in both the Royal College of Science main building, Imperial Institute Road, and the Huxley Building, Exhibition Road, a representative selection being exhibited in each building. The entrance to the Huxley Building is opposite the Science Museum. Tickets will be valid for entry into both buildings: on Thursday morning and afternoon, April 3rd, the Exhibition will be open to Members of the Society and Press only.

Discourses will be delivered by eminent scientists on Friday, April 4th and Monday, April 7th, and the prize-winning entries of the Society's Craftsmanship and Draughtsmanship Competition will be on show. This competition is assuming increasing popularity and importance among instrument making firms and is another example of the service the Physical Society is undertaking in the national interest.

The Handbook of the Exhibition containing the description of exhibits will be available from the Physical Society early in March, price 7s. 3d. including postage.

Recent Appointments

Alfred Africano has been appointed an adjunct assistant professor in the Aeronautical Engineering Department of New York University's College of Engineering, to teach a new rocket course "Introduction to Rocket Propulsion."

The appointment of *Dr. Donald W. Collier* as Director of Research for Thomas A. Edison, Incorporated, West Orange, New Jersey, has been announced. Dr. Collier will have charge of

the Edison Central Research Laboratories and will take an active part in the expansion of the laboratories with the addition of new facilities now in the planning stage.

Dr. James De Juren, authority on neutron measurements, has joined the Atomic and Radiation Physics Division of the National Bureau of Standards. Other new members of NBS staff: *Dr. George T. Armstrong* will be investigating the vapor, liquid equilibria in mixtures of oxygen and nitrogen; *Dr. Abner Brenner*, Chief of the Electrodeposition Section of the National Bureau of Standards; *Frank R. Edgarton*, formerly a senior mechanical engineer with the Stromberg-Carlson Company, will assist at NBS in the development of fuzes for guided missiles; *Dr. Derrick H. Lehmer*, has been appointed Director of Research of NBS for Numerical Analysis in Los Angeles; *Edward C. Lloyd*, Assistant Chief of NBS Office of Basic Instrumentation; and *Pei Moo Ku* has joined the staff of the Engines and Lubrication Section of NBS.

Dr. Ralph Bown, Director of Research for Bell Telephone Laboratories since 1946 and a member of the Bell System for more than 30 years, was appointed Vice President in charge of research effective January 2, 1952, Dr. M. J. Kelly, President of the Laboratories, has announced.

Other organization changes at the Laboratories include the appointment of *Dr. J. B. Fisk* as Director of Research—Physical Sciences; *Dr. H. T. Friis*, appointed Director of Research in High Frequency and Electronics; *Dr. W. H. Doherty*, appointed Director of Research in Electrical Communications; and *Dr. R. M. Burns*, appointed Chemical Coordinator in addition to his duties as Director of Chemical and Metallurgical Research.